AD-A269 742

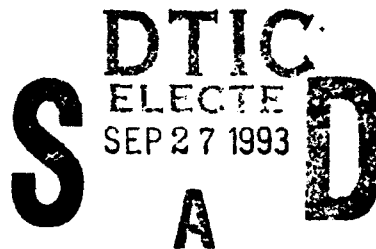# DEVELOPMENT OF THE MICROSTRUCTURE BASED STOCHASTIC LIFE PREDICTION MODELS

Progress Report
ONR Grant No: N00014-91-J-1299

Submitted to:

Dr. *A. K. Vasudévan*
Technology Directorate
Code 4421
Office of Naval Research
800 North Quincy Street
Arlington, VA 22217-5660

Prepared by :

Professor *Marek A. Przystupa* (Principal Investigator)
Jimin Zhang
Annetta J. Luévano
Department of Material Science and Engineering
University of California
Los Angeles, CA 90024
Tel.: (310) 825-6559
FAX: (310) 206-7353

August, 1993

93-22230

93 9 24 034

CONTENTS

ABSTRACT

The objective of the fatigue life prediction program at UCLA is to
(1) ascertain microstructural features relevant to fatigue in aluminum 7050
alloys and develop quantitative methods for their characterizations,
(2) characterize initial microstructures and accumulation of microstructural
damage during fatigue of 7050-T7451 plate alloys and (3) formulate and test
scaling relationships and models relating relevant microstructural features
to fatigue damage in aluminum 7050 alloys. Emphases during the reporting
period were on the completion of the metallographic and fractographic ex-
aminations of the high and low porosity 7050-T7451 commercial 6" plate al-
loys. Obtained results include quantification of the through thickness
gradients of grain structures and volume fractions and size distributions of
the constituent particles, pores and precipitates. To our knowledge this is
the most complete set of microstructural data on the 7050-T7451 commercial
plate alloys. Characterizations of the fracture surfaces and microstructures
of fatigued samples are in progress. Up to date results include data on the
change of surface roughness and fractal dimension with fatigue crack length
and preliminary information about microstructural features on the crack
path. Modeling has been focused on the predictions of the size distributions
of the fatigue crack initiating pores and on the incorporation of the
microstructural variables into existing fatigue life prediction models. The
most significant outcome from the modeling work has been development of
the methodology for predicting size distributions of the crack initiating pores
from metallographic data using extreme value approach. The obtained
distributions, when used with the proposed Paris/Erdogan type crack growth
model, give very good predictions of fatigue lives. Modeling effort also
included test of the capabilities of the Markov chain approach for potential
use in incorporating series of models describing different stages of fatigue
life. Future plans include: (1) finishing fractographic characterizations of the
old and new pedigree 7050 alloys, (2) microstructural and fractographic
characterizations of the low porosity and thin plate variants of the 7050 al-
loys, (3) refinement of extreme value methodology for predicting size distribu-
tions of the fatigue crack initiating microstructural features, (4)
incorporation of results of the microstructural characterizations into the next
versions of the life prediction models.

A. Introduction

The purpose of the program is to address current needs in the areas of the characterization of fatigued microstructures and in the incorporation of the microstructural parameters in fatigue life prediction models. The emphases during the reporting period, from January 1992 to June 1993, were on the completion of the microstructural characterization of the "high" and "low" porosity 7050-T7451 commercial plate alloys and on the formulation of preliminary life prediction models[1]. In the microstructural characterization part of the program we have concentrated on the development of the methodologies for (a) predicting size distributions of the crack initiating flaws and (b) characterization of the microstructural fluctuations on the crack path. To calculate size distributions of the crack initiating flaw we assume that they are extreme values of the distributions of the micropore and/or constituent particle sizes measured on the metallographic sections. The predictions are verified by comparing them with the size distributions of the actual crack initiating flaws obtained from fractographic examinations.

To characterize microstructural fluctuations on the crack path we use (a) the tessellation technique to measure local second phase spatial and volume fraction distributions and (b) a modified linear intercept method to characterize the inhomogeneities of the grain structures. The utility of all techniques has been tested by characterizing initial and fatigued microstructures of the 7050 alloys. Obtained results, together with the results of the fatigue testing acquired from Alcoa group, have been used to develop Paris/Erdogan type microstructure based fatigue life prediction model. We anticipate that different specialized microstructural models may be needed to describe behavior during different stages of fatigue life and intend to integrate them using Markov chain approach.

B. Materials

The investigated materials included through-thickness sections and the open hole fatigue specimens made from the "high" porosity (old pedigree) and "low" porosity (new pedigree) 7050-T7451 plate alloys[2,3].

Both alloys have been obtained from Alcoa group as a result of the Alcoa/UCLA/ONR collaboration on the program. Up to date we have completed characterizations of the grain, constituent particle and pore structures at the surface, quarter and the center depth locations of the as-received plates. All characterizations were performed on the TL, LS and ST planes. We have also characterized the morphology and the size distributions of the grain boundary precipitates in both alloys.

The open-hole fatigue samples used in this study have been fatigued to failure under cyclic load with $\sigma_{max} = 240$ MPa and $R = 0.1$. Four broken samples, two from each studied alloy, were used in the fractographic characterizations and in the identifications of the crack path features. These studies are still in progress thus only preliminary results are given in this report.

C. Quantitative Techniques

All stochastic life prediction models require as input not only the average values of the microstructural characteristics, but also their distributions. To facilitate required material characterizations we have assembled a PC-based image analysis system and developed a set of custom-made data acquisition programs. These programs analyze digitized images of microstructural features and automatically compile relevant characteristics of the grains, second phase dispersions, fracture surface profiles and perform tessellation analysis. The particular method used by the programs are described in detail below.

1. Grains

To characterize grain structures we use a modified linear intercept method described in [4,5]. In this method the average intercept length, $L_2(\alpha)$, of a two dimensional object at a scan angle α is defined as[6]

$$L_2(\alpha) = \frac{A}{H_2(\alpha)} \tag{1}$$

where A is the measured object area and $H_2(\alpha)$ its tangent height or, in other words, the length of the projection of the measured object on the direction perpendicular to the scan lines. The average grain size, D, is defined by us as the average of all intercept lengths, $L_2(\alpha)$, over all scan angles. The scan angles used for averaging vary from 0 to 180° in 5° increments. The same definition of size has also been applied to pores and constituent particles.

To quantify the grain shapes the plots of the normalized average intercept length, d, defined as:

$$d = \frac{L_2(\alpha)}{\max_{0<\alpha<180} L_2(\alpha)}$$

vs. scan angle, α (e.g. Ref. 4, Fig. 7) were used. The shape index, SI, proposed by us is defined as the area under the d-α curve[4] and is equal to:

$$SI = \frac{1}{\alpha_p} \int_0^{\alpha_p} d \, d\alpha \qquad (2)$$

where α_p is the period of the d-α curve. As demonstrated in reference [5], SI has values between zero and one and is independent of the object size and its orientation with respect to the scan lines. This shape index can be viewed as a measure of the deviation from the circular shape: it is equal to one for a perfect circle and decreases as the shape becomes elongated. The intercept length vs. scan angle data have been also used in calculating the coefficients of the spherical harmonic functions describing the change of grain dimensions with orientations[3,7,8] and in characterizing grain orientations and alignment[4,5]. We also use the traditional shape descriptor, aspect ratio, to characterize shapes of dispersions and grains in this work.

Since the investigated alloys were partially recrystallized, the fractions of both recrystallized and unrecrystallized grains had to be

4

estimated. In all measurements it was assumed that the area fractions occupied by different types of grains were equal to their volume fractions. The recrystallized grains were identified as the ones which (1) were more elongated and positioned along the grain boundaries of the equiaxed grains; (2) appeared lighter under the optical microscope after etching with Keller's agent; (3) contained more constituent particles.

The magnification used in all grain size measurements was 100 X. The measurements were carried out on all previously described 9 sections for both studied alloys. To ensure satisfactory statistics approximately 290 grains have been measured for each section.

2. Second Phase Dispersions

Both studied alloys contained pores and constituent particles. Their sizes, size distributions, shapes, orientations, area fractions and aspect ratios have been measured using the same methods as for grains. In addition, the tessellation method [1, 9-11] was used to characterize the distributions of particle spacings, local area fractions and the clustering indexes. The tessellation method was used because it allows for the quantification of minute changes in dispersion spatial characteristics and for the determination if the particle clusters are real or accidental. The reason that we choose to use the area fractions rather than volume fractions in all characterizations was that this quantity was measured without conversion error. In addition, since fatigue cracks are usually planar, the measurement on the plane sections are more representative of the microstructural features encountered by the cracks.

To obtain reliable measurements of the particle or pore spatial distribution, one needs to compile data about relative coordinates of as many features as possible. The problem with their collection is the need for scanning large areas under high magnification; this assures easy second phase detection and at the same time gives good representation of their spatial distribution. The best way to proceed is to make a large composite 'map' from several fields representing smaller areas and this

method has been used in this work. The outlines and the local coordinates of the centers of second phase dispersions were recorded for each field and then used in calculating the absolute coordinates from the reference coordinates of each field. The process is very time-consuming as about 200 view fields are needed to make one composite map.

The magnification used in the second phase characterizations was 900 X. It was chosen as the best compromise between the efficiency and accuracy. The total number of the constituent particles measured was 3908, which is approximately 220 particles per section. This corresponds to the total scanned area of 22.42 mm² or 1866 fields under the microscope. The number of pores detected during the scan of 3699 fields was 3261, that is about 181 pores/section. The total scanned area was in this case 44.45 mm² which is about twice the area scanned for constituent particles. The difference is due to the pores' lower volume fraction.

3. Precipitates

Precipitates sizes were measured from enlarged bright- and dark-field images using a digitizer. The size of the precipitates was defined as the longest dimension of the precipitate as seen in the photograph. This measure was used because the precipitates on the boundaries can be approximated as circular plates, thus their longest dimension corresponds to the diameter.

In addition to measuring the size and size distributions, the density of the grain boundary precipitates in terms of area fraction (A_f) and spacing (center-to-center and surface-to-surface) were calculated. The area fraction has been defined as the total area of the precipitates divided by the area of the grain boundary. It can be calculated from the following equation:

$$A_f = \frac{\frac{\pi}{4}\langle d\rangle^2 N_p}{l \cdot w} \qquad (3)$$

where N_p is the number of precipitates observed on the boundary, $\langle d\rangle$ is their average size, and l and w are the grain boundary length and width.

The length of the grain boundary was measured directly from photographs while foil thickness measurements were used to obtain the boundary width. As already indicated equation (3) assumes that all the precipitates are thin circular plates.

The precipitate spacing was calculated using formula [12]:

$$\text{center-to-center spacing} = 1.2 \times N_a^{-1/2} \qquad (4)$$

where:

$$N_a = \frac{N_p}{l \cdot w} \qquad (5)$$

and is the number of precipitates per unit grain boundary area. Surface-to-surface spacing was calculated as center-to-center spacing minus the precipitate average diameter. Although the above equations are strictly valid only for identical and evenly spaced precipitates, they give a good approximation in the considered case.

To determine the width of the grain boundaries used in the calculation of the number of precipitates per unit boundary area, N_a, the foil thickness measurements had to be made. They were performed using the convergent beam method as described by Kelly et al. [13].

4. Fractography

The method used for characterizing fracture surfaces of fatigued open-holc samples has been based on the measurements of (1) the orientation distributions of the line elements along the fracture surface profiles and (2) the *profile* roughness parameter. This approach was chosen because it makes possible calculation of the fracture *surface* roughness parameter and the measurement of the fractal dimensions [14-18]. To obtain the fracture surface profiles we have adopted the sectioning method proposed by Gokhale et al. [18]. The four open-hole fatigue specimens used in this study had TL orientation and they have been cycled to failure at Alcoa. All specimens had been used for general fractographic examinations. One new pedigree specimen had been selected for detailed fracture surface

characterizations at three different regions along the crack path. All measurements have been automated by developing a specialized software.

The surface roughness parameter was measured using the technique recommended by Gokhale et $al.$ [17,18]. The method involves characterizations of the fracture surface profiles of three sections, 120° apart, and estimation of the surface roughness parameter, R_s, using the formula:

$$R_s = R_L \psi \tag{6}$$

where R_L is the profile roughness parameter and ψ is profile structure factor. R_L is obtained from the ratio of the true length of the crack profile to the crack projected length. ψ is completely described by the profile segments orientation distribution function, $f(\alpha, \Phi_p)$, where α is the angle between the profile segment and the normal of the crack plane and Φ_p is the angle between the section plane with the surface of the open-hole specimen. The value of $f(\alpha, \Phi_p)$ is the frequency of α for profile line elements.

Surface roughness characterizations have been supplemented with the measurements of fractal dimension using the Mandelbrot plots method [19]. The fractal analysis is based on the principle that the number of ruler lengths, N, required to cover the length of an irregular line depends on the ruler size, R. Small ruler resolves finer details than larger one, requiring a disproportionately greater number of steps to cover the line length. A plot of $\log(N)$ vs. $\log(1/R)$ for an ideal fractal curve should yield a straight line, thus it can be described by the relation:

$$N = k(\frac{1}{R})^m \tag{7}$$

where m is the fractal dimension and k is a constant. Such plots have been used in this work to obtain fractal dimensions.

5. Sample Preparation

i. Optical and SEM

Specimens for optical and scanning electron microscopy (SEM) were first mechanically ground to a surface finish of 600 grit using wet SiC paper. They were then polished on a felt wheel wetted with ethanol using 1 μm and finally 0.25 μm diamond pastes. This new procedure provides a cleaner surface with less particle pull-outs than the one we reported earlier[2].

All samples for the grain size measurement were etched with Keller's agent to reveal grain boundaries. Etching for about 1 minute produced the best results for both unrecrystallized and recrystallized grains as well as for the subgrains. The characterizations of the porosities and constituent particles were made on as-polished specimens. We have found that large percentage of constituents etches out after just a few seconds exposure to the Keller's agent. Therefore the etching was not used although it would enhance the images of both pores and the particles.

ii. Fatigued Fracture Surface

To prevent any possible damage during the cutting process, the fracture surfaces of the open hole fatigued samples were coated with a layer of copper approximately 20 μm thick. The electroplating solution used for coating was a modification of the one used by Cheng *et al.*[20]. The plating was carried out at room temperature in a solution of 250 g $CuSO_4 \cdot 5H_2O$ + 50 ml H_2SO_4 + 1 liter H_2O. The voltage used was 5 V and the optimum time turned out to be about 30 minutes. The procedure was first calibrated on several dummy samples to check the quality of the coating before the real specimens were used.

iii. TEM

Samples for use in the transmission electron microscope were prepared from the surface and center sections of the plate. Slices cut from the material were thinned to approximately 250 μm and used to make 3 mm disks. The disks were dimpled using a room temperature solution of 10 % nitric acid and 90 % water at a voltage of 25 V. Final polish and perforation were accomplished using a solution of 30 % nitric acid and 70 % methanol at a temperature of -30 °C and a voltage of 15-18 V. The samples were examined in a 100 KeV JEOL transmission electron microscope.

D. Results

1. Grains

We have completed characterizations of grain structures on all nine sections for both pedigree 7050-T7451 plate alloys. The locations of all examined sections are shown in Fig. 1. The collected data include quantification of the recrystallization levels and the size and shape distributions of recrystallized and unrecrystallized grains and subgrains. To our knowledge this is the first complete set of such data for the 7050-T7451 alloys.

A typical grain structure of 7050-T7451 alloy is shown in Fig. 2. The recrystallized grains appear white and elongated while the unrecrystallized are darker, equiaxed with fine subgrain structure. The dark spots in Fig. 2 are constituent particles. Figure 3 shows typical subgrain structure at higher magnification.

Both investigated plate alloys were partially recrystallized with recrystallization levels from about 2% at the surface to about 20% at the center. Table 1 and 2 list recrystallization level and Fig. 4 shows the change of the degree of the recrystallization with depth. The area fractions of the recrystallized grains are always lower for the old pedigree material, particularly at the quarter depth. The differences can be

attributed to the differences in the thermal processing conditions and compositions of both plates.

The sizes of the recrystallized grains are summarized in Table 1. They ranged from 22 to 54 μm with slightly larger grains in the new alloy. For both pedigrees the grains were larger at the center than in the quarter depth. The higher recrystallization levels in the center regions are clearly responsible for the larger sizes of the recrystallized grains. Figure 5 shows the size distributions of recrystallized grains at different locations for both new and old pedigrees alloys. The grain sizes in the figure (and in all the cumulative distribution plots in this report) are obtained by feature to feature scanning. Each data point in the figure is the average of 1000 intercept lengths scanned for each grain. The size differences at different locations can be easily seen in Fig. 5.

The collected data on the unrecrystallized grains are summarized in Table 2. Their sizes varied and were largest at the quarter depth for the old and in the center region for the new plate alloys. The new alloy had finer overall grain structure with the sizes, depending on the test plane orientations, ranging from 45 to 170 μm. For the old alloy the grains were in the 75 to 220 μm range. The cumulative size distributions of unrecrystallized grains for both pedigrees are shown in Figure 6 and the differences between pedigrees are obvious. The same trend can be seen in Figs. 7 and 8 which show the change of an average grain size with direction for different test planes and for different plate locations. The plots are in polar coordinates (from 0 to 180°) and they show the change of average diameters with directions on a given test plane. Figures 7 and 8 are then visual representations of the change of the grain size with orientation and location. If the grains are assumed to be ellipsoidal, then the diameters at 0 and 90° on the plots represent major axes. They can be thus used in calculating constants in the spherical harmonic representing the grain shapes[3].

The change of the unrecrystallized grain sizes with position is not always monotonous. For instance in the new alloy the unrecrystallized grains are the largest at the quarter depth. One of the reasons for this

anomaly is a strong dependence of the unrecrystallized grain sizes on the recrystallization level which can be described by the relation[3]:

$$D = D_0 \sqrt{1 - f} \qquad (8)$$

where D is the observed unrecrystallized grain size, f is the area fraction of the recrystallized grains and D_0 is the starting, i.e. true unrecrystallized grain size. Since both investigated alloys are almost unrecrystallized at the plate surfaces, only the grains near that location have the characteristics of the true, unrecrystallized grains. The sizes of the unrecrystallized grains at the quarter and center depths are smaller and reflect both the original unrecrystallized grain sizes and the recrystallization levels. If one compares the grain sizes of the old and new pedigrees at the surfaces, it is found that the new alloy has much finer grain structure. The same holds for the grain sizes at the quarter depth and the center if they are corrected for the effects of the recrystallization using Eq. (8).

As reported earlier, only unrecrystallized grains had subgrains[3]. Their sizes were measured in the new alloy and only on the TL planes. The average subgrain size for the surface, center and quarter depth was 6.17 μm and subgrain size distribution is shown in Fig. 6, Ref. 4. The morphology of the subgrains can be represented by arrays of squares oriented at either 0 or 45° to the rolling direction[4].

The grain shapes have been characterized in both alloys for all nine sections using aspect ratio and shape index, SI. Typical plots used in these measurements are shown in Fig. 7, Ref. 4. The aspect ratios obtained from these plots varied from 1.80 to 4.25 for the unrecrystallized grains and from 1.71 to 3.88 for the recrystallized ones. They were 1.05 for the subgrains. The average aspect ratios are 2.07 and 2.29 for recrystallized grains of new and old pedigrees respectively, and 2.50, 2.75 for unrecrystallized grains of new and old pedigrees. The average shape indexes, SI, defined earlier[4], were 0.66 and 0.65 for recrystallized grains of new and old pedigrees, 0.62 and 0.61 for unrecrystallized grains of new

and old pedigrees respectively. The values of aspect ratio and shape index for each individual location can be found in Tables 1 and 2.

To characterize the grain size distributions, the experimental size data were fitted with both the normal and lognormal distributions using appropriate probability plots[21]. The correlation coefficient R^2 were used as a measure of the goodness of fit. Both the recrystallized and unrecrystallized grain size distributions turned out to be normal. For example, the distribution of the unrecrystallized grain sizes for the new alloy (LS plane, quarter depth) had R^2 value of 0.9487 when using the normal distribution fit. This value is only 0.8482 for the lognormal distribution fit. The parameters of the distributions obtained from the above analysis are listed in Tables 3 and 4. Typical fitting curves for both recrystallized and unrecrystallized grains are shown in Fig. 9.

2. Second Phase Dispersions

i. Pores

All quantitative characterizations of pores have been carried out on a PC-based image analysis system. A typical pore is shown in Fig. 10 and a collection of 201 pores found on the ST plane at the center section of the old 7050 alloy is shown in Fig. 11. The locations of pores in Fig. 11 are arbitrary but their real locations with respect to each other were recorded in a separated data file for subsequent tessellation analysis. The results of pore characterization are summarized in Table 5 and in graphical form, in Figs. 12, 13 and 14. The average pore sizes were 3.39 μm for the old and 3.47 μm for the new alloys. The pore volume fractions, assumed equal to the area fractions, were 0.134% for the old and 0.102% for the new plate alloys. The porosity level in the new alloy has been reduced by 24%. The results also indicate that the pore volume fractions are the highest at the centers and the lowest at the surfaces of the plates. The pore sizes, as shown in Figs. 12, 13 and 14, are also the smallest at the surface regions. Analysis of variance of the pore sizes in the new and old alloys resulted in the F value of 3.177 which is smaller than the critical F

of 3.844 corresponding to 0.05 significance level. This means that the average pore sizes for the two pedigrees are statistically the same at 95% probability. Our pore volume fractions are slightly higher than those reported by Magnusen et al. [22] for the same materials. We believe that the discrepancies are due to the differences in the sample preparation techniques and, as a result, in the differences in the number of detected pores, pull-outs assumed as pores, etc.

As for the grains, the pore size distributions were identified by fitting the data with straight lines on the normal and lognormal probability plots using R^2 as the measure of the goodness of fit. Unlike that for grain sizes, the pore sizes followed the lognormal distribution with R^2 close to one. The calculated size distributions parameters are compiled in Table 6. Typical size frequency distribution and the lognormal fit are shown in Figs. 15 and 16.

As described earlier, to characterize shapes we use the plots of the average intercept length versus scan angle (d-α plots)[4,5]. Examples of such plots are shown in Figs. 17 and 18. Note that Fig. 17 has two different normalized average lengths: the average d and overall d[4,5]. As explained in Refs. 4 and 5, the *average d* reflects the pure shape while *overall d* has also alignment component. The polar plot in Fig. 18 represents the average pore profiles. In this case the orientation effect has been eliminated by aligning the pore's major axes before scanning. The average pore aspect ratios were 1.45 and 1.51 for the old and new alloys respectively suggesting similar pore morphology in both pedigrees. The shape indexes were 0.8311 for the old and 0.8158 for the new alloys.

The pore spatial distribution has been quantified using the Tessellation method[1,9-11]. Figure 19 shows an example of the Dirichlet tessellation cell construction for pores on the ST plane at the center section of the old plate and Table 7 lists all characteristics obtained from the analysis. The most important parameters listed in the Table 7 are local volume fractions, near neighbor distances and nearest neighbor distances - these quantities can be obtained unambiguously only from the tessellations.

14

To classify the spatial distribution of pores we used following indexes[1]:

$$Q = \frac{\text{Observed Nearest Neighbor Distance}}{\text{Expected Nearest Neighbor Distance}} \qquad (9)$$

$$R = \frac{\text{Observed Nearest Neighbor Distance Standard Deviation}}{\text{Expected Nearest Neighbor Distance Standard Deviation}} \qquad (10)$$

where the expected values are calculated by assuming that the pores have random spatial distribution. As an example, pores on ST plane at the center of the old plate alloy have an expected nearest neighbor distance of 48.2 µm with a standard deviation of 33.2 µm. This gives values of Q = 0.929 and R = 1.224 which suggests that the distribution of the pores, which are collected in Fig. 11, can be classified as random with clusters.

We have also applied the linear intercept method [3,4] to the tessellation cell constructions to identify the pore spatial distribution patterns. The method was based on the principle that for a totally random set of points representing pore centers, the Dirichlet tessellation cells are also random with shape index[3,4] equal to one. On the other hand, if the point distribution is regular, for example in a form of rectangular or a hexagonal network, the shape indexes are less than one. The methodology developed for characterizing two-dimensional grain shapes can be thus used to characterize tessellation cells. Consequently, by comparing the curves of the normalized intercept length vs. scan angle for the tessellation cells constructed on pores with those on the random and on the regular patterns, the spatial distributions of pores can be identified. An example of such analysis is given in Fig. 20 where the distribution of intercept lengths for the pore cells was compared with those for the patterns of 500 random points and points arranged in a rectangular network. The pores' d-α curve lies between the ideal random pattern and the rectangular pattern. This again suggests that the pores have tendency to form clusters.

In addition to the above-mentioned methods for quantifying spatial distribution, we are developing a technique for characterizing clusters. In particular we are evaluating the methods of characterizing the distributions of cluster, point densities within the clusters and the methods of identifying pattern of random points with clusters. This work is currently in progress and results will be included in the forthcoming reports.

ii. Constituents

The constituent particles were characterized using optical microscopy, SEM and EDX techniques. As reported earlier[3] there are two types of particles in both investigated alloys. The particles of the first type are Al_7Cu_2Fe constituents. They appear as clusters of stringers of various lengths and shapes as shown in Fig. 21. The second type of constituents have been identified as $Al_xMg_xSi_x$. These particles also form stringers, but their surfaces were smooth and without clusters as shown in Fig. 22. We also observed a number of cracks in the constituents of both types. Although some of the constituents cracking took place during polishing process we have no doubt that the majority of the cracked constituents were there from the beginning. This observation is again the first report on the cracked constituents in the 7050-T7451 alloy that we are aware of. A typical collection of 236 particles from the ST plane at center section of the old alloy is shown in Fig. 23.

The constituents were quantified using the same analytical methods as for pores. The average sizes for both constituent types, measured on all sections, were 4.02 μm for the new and 4.77 μm for the old alloy, Table 8. The cumulative size distribution of the particles is shown in Fig. 24. The change of diameters with direction for different planes and positions within the plates is shown in Figs. 25 and 26. They indicate that particle size increases with depth. For example, the average sizes for the new alloy increases from 3.25 μm at the surface to 4.93 μm at the center. The differences are most likely a result of the variation of the temperature

during thermal processing and/or casting of the plates. The analysis of variance showed that the particle sizes in the old pedigree alloy are, at 95% probability, statistically larger than those in the new alloy. As expected, the average particle sizes are always the smallest for the ST plane sections. This is due to the particles' deformation during rolling.

The constituent particle area fractions were 0.61% for the new pedigree and 0.70% for the old one. This difference is the most significant improvements in the microstructure of the new 7050-T451 plate alloys which came out from our analysis. We again note that although the particle sizes obtained in this study were comparable to those reported by Magnusen et al.[22] our area fractions are slightly higher. As before we attribute these differences to the different sampling techniques.

The average d versus scan angle, α, plots[3,4] for particles from Fig. 23 are shown in Figs. 27 and 28. They were used in the analysis of the constituent shapes. The shape index SI for those particles (old pedigree) turned out to be 0.74 and their aspect ratio was 1.86. For the new alloy these values were 0.68 and 2.28 respectively. This indicates that the constituents are elongated, ellipsoidal in shape and that they were aligned with the rolling direction[4]. However, we have also observed instances of isolated, round and slightly oval constituent particles as well. Detailed results of shape analysis have been summarized in Table 8.

The size distributions of the constituents have been identified by fitting the data to both normal and lognormal distributions. As in the case of the pores the sizes of the particles follow the lognormal distribution with R^2 very close to one. Typical size frequency distribution and the lognormal fit are shown in Figs. 29 and 30. The parameters obtained from the above analysis are listed in Table 9.

The particle spatial distributions have been analyzed using both the tessellations and the linear intercept techniques described in the previous sections. Typical results from the tessellation analysis are listed in Table 10. In this particular case the expected nearest neighbor distance was 25.2 μm with standard deviation 19.2 μm. This gives Q = 0.879 and R =

17

1.281 which suggests that the distribution of the constituent particles on ST plane in the center of the plate can be classified as random with clusters.

iii. Precipitates

To identify the precipitate phases present in the studied alloy the obtained diffraction patterns were compared with those found in the literature on 7075 and 7050 alloys. The patterns of the studied alloy turned out to be identical to those obtained by Park and Ardell for overaged 7075 [23]. Since the predominate phases in the 7050 alloys have been identified as η', η_1, η_2, and η_4 with the grain boundary precipitates being one or more of the η phase variants (η_2 and η_4 are predominate on low angle boundaries) the same phases are expected to be present in the studied alloy. All grain boundary precipitates appear as thin hexagonal plates varying in size for different boundaries (Fig. 31). The only exceptions have been found in the center section (Fig. 32) where some boundaries contain a multiple of precipitate variants that are not all hexagonal plates.

Although the average size and density of the grain boundary precipitates are effected by the boundary type [24,25], this distinction (in particular high versus low angle) was not taken in to account in this study. This was because the material was partially recrystallized thus it contained a large number of subgrains. In such a material high angle grain boundaries are difficult to locate and a high percentage of the boundaries examined were low angle. To locate high angle boundaries, each TEM sample was rotated to a known zone axis and then the entire thin area was scanned in the diffraction mode to find large shifts in the diffraction patterns across boundaries. In all cases the shifts in the Kikuchi pattern and the rotation of the diffraction pattern were very small.

Even though most of the boundaries were low angle, they did exhibit a wide range of precipitate sizes. We also observed instances where low angle boundaries contained large precipitates. For example, the grain

boundary precipitates in Figure 33 have an average size, $\langle d \rangle$, of approximately 150 nm, while shift in the diffraction patterns on either side of the boundary is only 2.7 °. The wide range of precipitates sizes on low angle boundaries is contrary to what was reported by Park and Ardell [25]. In the 7075 alloy investigated by them, the low angle boundaries always contained small precipitates while the high angle boundaries always had large precipitates. Unfortunately, their paper did not contain quantitative information on the precipitate size which precludes direct comparison.

Size distributions

Low magnification photographs were used to study the features of the boundaries with precipitates and to asses the size distributions of precipitates on various boundaries (Fig. 34). Although the precipitate sizes vary widely, both surface and center regions of the studied plate showed that approximately 90 % of the boundaries contained some sort of precipitates. The precipitates observed on these boundaries were divided into size categories of small, medium, and large. Surface sections of both alloys contain 75 % of the boundaries with small precipitates while the precipitates on the rest of the boundaries could be considered as medium. The center sections showed the reverse trend with 60 % of the grain boundaries containing medium or large precipitates.

Results of a more quantitative evaluation of the grain boundary precipitates size distribution can be seen in Figure 35. The surface sections of both alloys exhibit lognormal distributions of the precipitate sizes while for the center sections the distribution is bimodal. The bimodal distribution is not unusual and it has been reported in alloys that are doubly aged, particularly as thick plate, which is exactly the condition of the investigated alloys. For example, Unwin and Nicholson [24] reported bimodal distributions of precipitates in doubly aged 7050 and attributes formation of the larger precipitates to the quench (the center of the plate quenches slower than the surface) and the smaller precipitates to the regular aging process. The precipitates that nucleate during quench have more time to grow thus giving a bimodal distribution. Also,

the size range is much greater for the center sections than for the surface sections.

To determine whether the distributions of the precipitates on the boundaries are governed by the theoretical coarsening law, their size distributions were normalized by the average size for each boundary. The normalizations were performed for individual boundaries and for all boundaries from each section (Figures 36 and 37). The experimental distributions on all figures can be compared with the theoretical distribution for coarsening given by the equations [26]:

$$g(u) = \left(\frac{3}{4}\right)^4 u^3 \left(1 - \frac{3u}{4}\right)^{-19/6} \left(\frac{3u^2}{16} + \frac{u}{2} + 1\right)^{-23/12}$$

$$\times \exp\left\{\frac{1}{2} - \frac{\frac{2}{3}}{\frac{4}{3} - u} - \frac{1}{6\sqrt{2}} \times \left[\tan^{-1}\left(\frac{1 + \frac{3u}{4}}{\sqrt{2}}\right) - \tan^{-1}\frac{1}{\sqrt{2}}\right]\right\}; u < \frac{4}{3} \tag{11}$$

and

$$g(u) = \frac{4u^2}{9} \left(\frac{3}{3 - 2u}\right)^{11/3} \left(\frac{3}{3 + u}\right)^{7/3} \exp\left(\frac{-2u}{3 - 2u}\right); u < \frac{3}{2} \tag{12}$$

Equations (11) and (12) correspond to coarsening when volume fractions are equal to zero and one respectively. Normalized size, u, is defined as u = r/⟨r⟩, where ⟨r⟩ is average precipitate size.

It appears that the experimental distributions are better approximated by the theoretical distribution for volume fraction equal to one, although the heights are lower. The effect of volume fraction on theoretical distributions is non-linear and is the strongest between 0 and 0.05 with very little change between 0.05 and 1 [26]. Since the area fractions of precipitates on the studied boundaries were greater than 0.05 the

agreement should be considered as very good. The discrepancies can be attributed to the fact that the theoretical equations were derived assuming high angle grain boundaries while all boundaries investigated in this study were low angle [26].

Area fraction and spacing

The area fraction and spacing calculations for surface and center sections of both alloys can be seen in Table 11. There is a large variation in A_f and spacing of the precipitates. Most of the boundaries examined contained single variants of the η phase although a few of the boundaries contained multiple variants of η. For the data where $<d>$ or A_f are uniform, the spacing, as expected, is dependent on both $<d>$ and A_f in the following manner:

$$\text{spacing} \propto \frac{\langle d \rangle}{\sqrt{A_f}}$$

If the number of precipitates per area (N_a) is plotted versus the average size of the precipitates on the boundary (Fig. 38) it is found that N_a decreases exponentially as $\langle d \rangle$ increases for $\langle d \rangle$ greater than 50 nm. For $\langle d \rangle$ less then 50 nm there appears to be no correlation between N_a and $\langle d \rangle$. This is because the boundaries containing precipitates in this size range came from the surface sections where differences in precipitate area fraction and precipitate shapes are large, thus causing large scatter in the data.

3. Fatigued Fracture Surfaces

The fracture surfaces of the open hole fatigue samples were first examined using SEM under the secondary electron mode and then sectioned for the surface roughness measurements. The objective of the SEM general survey was to find the crack origins and to identify fracture modes and the mechanisms involved. Figure 39 shows an example of a fatigue crack initiating pore in the open-hole specimen cut from the center

section of the new plate. The pore is located next to the hole in the area where stress concentration is the highest. Figure 39 also shows a smooth featureless region around the pore where the local roughness is expected to be small. The diameter of the pore in Fig. 39 is about 15 μm. Of the four examined open-hole samples (two from each pedigree), crack initiating pores were found on both sides of the hole in three samples. In one sample from the new alloy the crack initiated from the surface flaw. We have not observed any evidence of the crack initiation from the constituent particles. However, such nucleation sites are expected in other variants of the 7050 alloy [27].

In addition to the main fatigue crack there were also evidences of smaller secondary cracks, Figs. 39 and 40. Another reoccurring feature of the fracture surface (Fig.40) was the traces of cleavage planes which suggest a transgranular fracture mode. The center region in Fig. 40 also shows river patterns crossing several grains. This region has been magnified (Fig. 41) showing changes in facet orientations. It also shows a constituent particle at the upper left corner. Stage II fatigue crack growth region can be seen in Fig. 42 and in Fig. 43 at high magnification. The striation spacing in Fig. 43 is about 330 nm.

Fracture surface profile has been quantified for one new pedigree open-hole fatigue sample. Figure 44 shows the experimentally measured profile orientation distribution functions, $f(\alpha, \Phi_p)$, for sections at Φ_p=0, 60 and 120° to the specimen surface. The profile roughness parameters (ruler length 4 μm), profile structure factor ψ and fractal dimensions m are summarized in Table 12. Experimental results of fractal dimension plots for the three sections are shown in Fig. 45 (a) to (c). In the ruler length used, i.e. 1 to 100 μm, the plots have excellent linearity. The slopes, which are the fractal dimension m, are between 1.05 and 1.11 with standard error less than 0.4%. The obtained fractal dimensions are comparable with those for Al-Cu-Li alloys reported by Alexander[28].

The change of surface roughness and fractal dimensions along the crack path are shown in Fig. 46. The samples were in this case cut from the crack initiation site, specimen outer edge and one location in between.

Obtained surface roughness parameters are the smallest at the crack initiation site, increase with the crack length and tend to level off for long cracks. The fractal dimensions show the same trend. The increase can be related to the different fracture mechanisms associated with different regions. At the crack initiation region, stage I growth, the fracture surface is relatively smooth and featureless thus roughness and fractal dimensions are small. On the other hand, near the specimen edge the fracture mode is ductile giving rise to very rough surface. Thus the fatigue fracture surface can not be characterized using average roughness parameter or fractal dimension. The crack has to be divided into different regions in order to facilitate meaningful comparisons. To confirm these preliminary results we are currently measuring fractal dimension and roughness parameter for other parts of the fracture surface and for samples of both the old and the new pedigrees.

E. Modeling

1. Fatigue Crack Initiating Flaw Sizes

All existing fatigue life prediction models require as input either average size of the initial cracks or crack size distribution. Since in the investigated 7050 alloys fatigue crack always initiates from micropores, it would be tempting to assume that the micropore and the initial crack size distributions are equivalent. As evident from Figure 47 such an assumption would be incorrect. The figure compares maximum pore dimensions obtained by us from metallographic characterizations with the actual sizes of the crack initiating pores obtained from fractographic examination by Alcoa group. In both alloys the actual crack initiating pores are at least order of magnitude larger than those measured on metallographic sections. The reason for this discrepancy is that the dominant fatigue crack does not initiate from a randomly chosen pore but from the one with the largest stress intensity. The stress intensities are the largest at the largest surface pores, hence the size distributions of such pores, one from each sample, constitutes distribution of the actual crack initiating pores. The problem of finding this distribution reduces thus to finding the extreme values of the parent size distribution obtained

from metallographic sections[29, 30]. The procedure for obtaining such extreme value distributions is described in the next section, followed by the section on experimental verifications.

i. Extreme value statistic

The true size distributions of pores or particles, or dispersions in general, can be obtained from metallographic measurements using well known procedures[33]. Let's assume that both the cumulative distribution, $F_D(d)$, and the probability density function, $f_D(d)$, obtained from such measurements are known and call them parent cdf and pdf respectively. Let us also assume that the number of pores or particles in the sample surface region is known and equal to n, which will be referred to as "sample size". The extreme value distributions of the largest dispersions in the surface region can be then obtained from the following relations[30]:

$$\text{cdf:} \quad F_{D_n}(d) = \left[F_D(d)\right]^n$$
$$\text{pdf:} \quad f_{D_n}(d) = \frac{dF_D(d)}{dd} = n\left[F_D(d)\right]^{n-1} f_D(d) \qquad (13)$$

The above equations are useful only for small sample sizes. For large n, expected in our case, the results from Eq. (13) degenerate and give probabilities either 0 or 1. To eliminate this problem, equations (13) can be replaced with their asymptotic equivalents [31]:

$$\text{cdf:} \quad F_{D_n}(d) = \exp\left\{-n\left[1 - F_D(d)\right]\right\}$$
$$\text{pdf:} \quad f_{D_n}(d) = nf_D(d)\exp\left\{-n\left[1 - F_D(d)\right]\right\} \qquad (14)$$

which give finite results for all n.

Equations (13) and (14) are valid for a constant sample size. When sample size varies, which is expected for the number of pores or particles

at the sample surface region, equation (13) for cdf has to be replaced with[30]:

$$\text{cdf:} \quad F_{D_n}(d) = \sum_{n=0}^{r} p_n \left[F_D(d) \right]^n \tag{15}$$

where p_n is the probability that sample has size n. In the considered case p_n can be adequately described by the Poisson distribution[32]:

$$p_k(k,n) = \frac{n^k}{k!} e^{-n} \tag{16}$$

where n is an expected average. Thus, combining Eqs. (15) and (16) leads to:

$$\begin{aligned}
\text{cdf:} \quad F_{D_n}(y) &= \sum_{k=0}^{\infty} \frac{n^k}{k!} e^{-n} \left[F_D(d) \right]^k \\
&= e^{-n} \sum_{k=0}^{\infty} \frac{1}{k!} \left[n F_D(d) \right]^k \\
&= e^{-n} e^{n F_D(d)} \\
&= \exp\left\{ -n \left[1 - F_D(d) \right] \right\}
\end{aligned} \tag{17}$$

where relation

$$\sum_{n=0}^{\infty} \frac{x^n}{n!} = e^x \tag{18}$$

has been employed. Note that the final result, equation (17), and previous expression for cdf , equation (14a), are identical. This means that for the Poisson distribution of sample sizes the extreme value distribution does not degenerate. Equations (14) are then valid for both constant and variable sample sizes.

The asymptotic cdf 's for extreme values have, theoretically, only three possible forms [29, 30]. These asymptotic forms depend on the type of the

parent distribution and are sometimes referred to as domains of attraction. In particular, if the parent distribution is of the exponential type, its domain of attraction is Type I or Gumbel distribution in the form:

$$F(x) = \exp[-\exp(A_n x)] \qquad (19)$$

For the parent of the polynomial type, the limiting distribution has Type II of Frechet form:

$$F(x) = \exp(-A_n x^{-k}). \qquad (20)$$

Finally, when the parent has an upper bound, then Type III or Weibull given by:

$$F(x) = \exp[-A_n(B_n - x)^k] \qquad (21)$$

serves as the limiting distribution. In all cases k is a constant and A_n and B_n are functions of the sample size. The domains of attractions for the most important distributions have been tabulated and they can be found for instance in reference [30]. Thus if the parent distribution is identified, the type of its extreme value asymptote is automatically known.

ii. Parent distributions

The problem of identifying parent distribution for the extreme value calculation purposes is slightly different from finding the best fit to the experimental data. Since estimates of the extreme largest values are based on the extrapolations of the parent right tail, the parent should be obtained by weighting tail values the most. The recommended weight function has following form [30]

$$w_i = \frac{1}{1 - p_i} \qquad (22)$$

26

where p_i is empirical probability of ordered point number i and this weight method has been adopted in this work. Moreover, the assumption about the shape of the parent distribution and its tail in particular is also detrimental to the precision of the extreme value estimations. Since there is no reliable information about the distributions describing pore or constituent particle sizes in 7050 alloys, we have assumed that they are either lognormal or Gumbel. The lognormal distribution was chosen because it usually adequately approximates size distributions of precipitates, dispersoids, grains, etc.[33]. The Gumbel distribution is on the other hand a domain of attraction, for the largest values, for the lognormal cdf [30]. It should be thus tail equivalent with lognormal, hence it would be reasonable to expect that it would also be a good approximation of the parent.

iii. Experimental Verifications

The most efficient method of verifying the distribution type is to plot data on the appropriate probability paper. Such plots for porosities and for lognormal and Gumbel distributions are shown in Figure 48 (linear plots are included for comparison). The plotted data comprise the distributions of (1) maximum pore dimensions on LS planes in the plate center regions for both old and new 7050 alloys (parent distributions) and (2) maximum dimensions of the actual fatigue crack initiating pores obtained from fractographic examinations of the failed smooth fatigue samples (extreme values). The parent distributions on both lognormal and Gumbel probability plots are not straight. However, in all cases the right tails can be approximated with straight lines suggesting that the choice of both lognormal and Gumbel cdf's are justified. The extreme value distributions in both cases are reasonably linear except for few points corresponding to the largest pores. These largest pores have approximately the same size, about 450 μm for old and 200 μm for the new alloy, suggesting that for each pedigree there is a maximum size limit.

27

To find which distribution was more appropriate for the extreme value calculations, the parent distributions were approximated with the ˅gnormal and Gumbel cdf's. The equations used were:

$$\text{Lognormal cdf}: \quad F(x) = \frac{1}{\sqrt{2\pi}\sigma} \int_{-\infty}^{x} \frac{1}{t} \exp\left[-\frac{1}{2}\left(\frac{\ln t - \mu}{\sigma}\right)\right] dt$$

$$\text{Gumbel cdf}: \quad F(x) = \exp\left[-\exp\left(-\frac{x - \mu}{\sigma}\right)\right]$$

(23)

Both the standard and the weighted least-square fit, with weights calculated using equation (22), were used. The standard fit was chosen to simulate an indiscriminate use of the metallographic data and/or us of data obtained from measurements taken under high magnification. The weighted fit made better use of the distribution tails and simulated metallographic examinations under low magnification. The results are shown in Figures 49-52 and summarized, in the "parent" column, in Tables 13 and 14. In all cases the correlation coefficients, R^2, for the standard least-square fits were greater then 0.95. The weighted fit lines had slopes intermediate between those for the standard fit and these for the distributions tail sections. There was no difference in the goodness of fit between lognormal and Gumbel approximations.

As the next step the least-square method was used to estimate the sample sizes, N, which gave in the best fit of the extreme values obtained from the parents to the fractographic data. In this case Eq. (14a) combined with Eq. (23) were used. Results are again compiled in Figures 49-52 and listed in Tables 13 and 14. They show clear superiority of Gumbel distribution in describing the experimental extremes for both investigated alloys. The failure of the lognormal distributions was due to the incorrect slopes, even when the parents were obtained using weighted fit. In all considered cases the approximation of the parent by Gumbel cdf using weighted fit resulted in the best fit to fatigue crack initiating pore size data, particularly in large size ranges. This is specially evident for the new alloy (Table 14) which has correlation coefficient for Gumbel extreme obtained using standard fit higher than that for the weighted fit

case. However, examination of the probability plots clearly suggests that this is due to large deviations in the small pore range, thus in the region which is not critical for the worst case design. For the large pore sizes the fit of the Gumbel extremes obtained from weighted fit are clearly superior.

The values of sample sizes, N, which gave the best approximations of fracture surface data require additional consideration. As already indicated, they represent the number of pores in the sample surface region which were interrogated, for the largest stress intensity, by the cyclic stress. To find if the obtained values were realistic, they were compared, see Table 15, with the number of pores in the entire gage section and/or with the number of pores intersected by the gage section surface. For both alloys the sample sizes for lognormal distributions were either larger then the total number of pores in the sample or equal to the number of pores in the surface layer from 1.4 to 2.7 mm thick. Both results for lognormal distributions are then unrealistic. For Gumbel distribution the N-values correspond to the number of pores either in the sample surface band from 0.6 to 5.5 mm wide or from the surface layer from 8 to 157 mm thick. The last two numbers are for the case of Gumbel distribution obtained using weighted fit: they are the most physically appealing, as they correspond to the surface layer of the order of pore size. This suggests that the fatigue crack initiating pore size distributions are extreme value cdf's of the pore size distribution obtained from metallographic sections for the sample size equal to the number of pores in the sample surface layer about pore size thick.

We are currently verifying predictive capabilities of the above extreme value method on two additional materials (Alcoa 7050 low porosity and thin plates) and for the fatigue failures in open hole samples. The new materials were chosen to allow test of the method when failure initiates from constituent particles and/or grains instead of pores. The open hole samples will let us investigate the effect of the change of the size of the interrogated volume due to the stress concentration on the predictions [34].

29

We are also evaluating methods of improving accuracy of the estimates of the right tails of the experimental pore or particle size distributions. One of the possibilities is performing metallographic characterizations under lower magnification to facilitate detection of rare large features [34]. Another is use of non-parametric method of approximating distribution tails without prayer assumption about their character. We are exploring here the Pickands method [35] which combines use of generalized Pareto distribution to describe the tail with the percentile method to estimate the parameters. Finally, the conversions of the size distributions obtained from plane sections to the true three dimensional size distributions are also under way.

2. Life Predictions

Results of material characterization are currently used in the development of the relationships between the distributions of microstructural characteristics and the distributions of fatigue lives. The goal of this part of the program is to develop microstructure based fatigue life prediction models which will predict not only the average fatigue lives but also life distributions. So far our modeling efforts have been focused on the test of the utility of the existing methodologies and on the ways of incorporating microstructural parameters into them.

The existing life prediction models can be divided into phenomenological and statistical. The first group contains models based either on the Miner's type law describing damage accumulation or on the Paris/Erdogan crack growth equation[36]. These models always contain at least one parameter related to material properties and since material properties are related to microstructure, hence phenomenological models have potential for linking microstructural parameters with fatigue life. The statistical models are usually derived from the statistical characteristics of the fatigue process and their parameters rarely have physical meaning[37]. Such models provide good fit to data but are unsuitable for linking fatigue life with the microstructure. They are however useful for incorporating several models together, for instance

different crack nucleation models with different crack propagation models, etc., to provide full description of the fatigue process. Up to data we have tested the sensitivity of life predictions based on the crack growth models and verified capabilities of the Markov chain approach [38] for potential use in integrating various models together. The results of these tests are described below.

i. Microstructural Model

Most of the phenomenological life prediction models are based on the Paris/Erdogan type crack growth equation which can be written in following general form[39]:

$$\frac{da}{dN} = F\{Load, Properties, Microstructure\} \qquad (24)$$

This equation is deterministic, thus suitable for predicting the average fatigue life. The variability can be introduced by augmenting Eq. (24) as *follows*:

$$\frac{da}{dN} = X(t) \, F\{Load_{av}, Properties_{av}, Microstructure_{av}\} \quad (25)$$

where X(t) is a non-negative stationary stochastic process. Such an approach, where X(t) is an experimentally measured function, has been proposed by Yang *et al.* [40] as an alternative to the equivalent initial flaw size (EIFS) approach. In a more rigorous description it would be necessary to assume that all parameters and/or variables in Equation (25) are stochastic. This leads to the following stochastic differential equation:

$$\frac{da}{dN} = F\{Load_{distr}, Properties_{distr}, Microstructure_{distr}\} \quad (26)$$

which, when solved for N, gives the distribution of fatigue life. Since the close form solution of equation (26) is usually possible only for one or two stochastic variables, it is often necessary to use alternative method to

obtain the distribution of fatigue lives. One of such method, based on the estimates of the expected mean and variance of the stochastic variables controlling fatigue process, was proposed by Besuner [41] and has been adopted in this work. The method assumes that the Paris/Erdogan equation describing crack propagation rate has the following form

$$\frac{da}{dN} = C \, \Delta K^m = C \, (A \, \Delta\sigma \, a^{1/2})^m \qquad (27)$$

where C and m are material constants, ΔK is a stress intensity, A is a crack geometry dependent constant and $\Delta\sigma$ is the stress amplitude. Solving equation (27) for number of cycles to failure, N, leads to:

$$N = N_o + \frac{a_f^{1-m/2} - a_o^{1-m/2}}{(1 - \frac{m}{2}) \, C \, A^m \, \Delta\sigma^m} \qquad (28)$$

where N_O is number of cycles to nucleate the initial crack of length a_o and a_f is the final crack size. In the 7050 alloys investigated so far the cracks always start at pores. It is thus reasonable to assume that the nucleation stage is insignificant, e.g. $N_O = 0$. Moreover, since a_f is at least two orders of magnitude larger than a_O and $m > 2$, thus term $a_f^{1-m/2} \approx 0$. Equation (28) can be thus simplified to

$$N = \frac{a_o^{1-m/2}}{(\frac{m}{2} - 1) \, C \, A^m \, \Delta\sigma^m} \qquad (29)$$

The only microstructural parameter in Equation (29) is the initial crack length, a_O, which is also in this case of the only random variable. If the distribution of initial crack lengths, $a_O(a)$, is known, the distribution of cycles to failure, $F_N(n)$, can be obtained from:

$$F_N(n) = \Pr\left[\frac{a_o^{1-m/2}}{(m/2-1)CA^m\Delta\sigma^m} < n\right] \qquad (30)$$

32

where Pr stands for probability and n is an instance of N. Other microstructural parameters can be introduced to Equation (30) through parameters C and A, using relations [36]:

$$C = \frac{C'}{(M\tau_{crss})^k} = \frac{C''}{M^k} \qquad (31)$$

$$A = A' \cdot A_{defl} \qquad (32)$$

where C', C'' and k (assumed equal 2 in all calculations [36]) are constants, M is a Taylor factor, τ_{crss} is critical resolved shear stress and A_{defl} is a correction for crack deflection. Substituting equations (31) and (32) to (30) leads to

$$N = \frac{a_o^{1-m/2} M^k}{(\frac{m}{2}-1)\, C''\, \left(A'A_{defl}\right)^m \Delta\sigma^m} \qquad (33)$$

which relates distribution of the cycles to failure, N, to the distributions of (1) initial crack lengths, a_0, (2) texture, through distributions of Taylor factors, M, and (3) crack deflections, A_{defl}, along the crack path. Finding the close form expression for the distribution of cycles to failure, N, is in this case a formidable task, as it is now the function of three random variables a_0, M and A_{defl}. However, it is possible to find the mean and variance of N by using theorems about the mean and variance of the sum of random variables [41]:

$$\overline{\ln N_f} = (1 - m/2)\overline{\ln a_o} + k\overline{\ln M} - m\overline{\ln A_{defl}} - \ln\left[(m/2-1)C''A'\Delta\sigma^m\right] \qquad (34)$$

and

$$V_{\ln N} = \left(1 - m/2\right)^2 V_{\ln a_o} + k^2 V_{\ln M} + m^2 V_{\ln A_{defl}} \qquad (35)$$

33

where bars indicate average value and V_x stands for variance of stochastic variable X. Consequently, if the average values and the variances of all stochastic variables are known, the variance and average value of cycles to failure can be estimated. Moreover, since most of the known distributions can be easy reproduced from their average values and variances, thus also in this case the full cumulative fatigue life distribution curve can be obtained if the type of the distribution which describe fatigue lives the best has been identified. This method is thus ideal for evaluation of the importance of different stochastic variables.

The above method of estimating distributions of fatigue lives has been verified using fatigue results for smooth fatigue samples made from both the old and the new 7050-T7451 alloys. The samples were subjected to tensile fatigue loading with maximum stress of 240 MPa, R = 0.1 and $\Delta\sigma$ = 216 MPa. The crack growth equation for both tested 7050-T7451 alloys can be described by equation [27]:

$$\frac{da}{dN} = 6.662*10^{-12} \Delta K^{4.175} \quad (36)$$

(it gives results in m if ΔK is in MPa m$^{1/2}$) which gives, Eq. (27), C = $6.662*10^{-12}$ and m = 4.175.

The first step in the proposed procedure was finding average values and variances of all stochastic variables controlling crack growth process. To simplify the problem it was assumed that the crack was straight, hence A_{defl} = 1 and the only two stochastic variables needed to be considered were a_O and M. In the considered case the average values and variances of the logarithms of the initial crack lengths, a_O, were equal to mean and variances of the logarithms of the maximum pore dimensions. They were obtained (1) from the pore size estimates using extreme value approach (weighted Gumbel fit) and (2) from the actual fractographic pore size data. Results are listed in Table 16.

Taylor factors, M, describe the effects of texture on fatigue life. Their distributions can be calculated if the strain states and textures on the

crack path are known. Since both are not available, it was assumed that the distribution of Taylor factors is uniform with the upper and lower bounds equal to expected minimum and maximum values. These bounds. for various strain states in the fcc metal are between 2.5 and 4.5 [43]. Accordingly, one hundred random numbers between 2.5 and 4.5 have been used to find the average value and variance of their logarithms needed in our calculations. Results have been listed in Table 16.

The geometrical constant, A, has been estimated to be 1.51. It was obtained by averaging A values for different surface elliptical crack sizes in a smooth round fatigue sample. The cracks aspect ratios were assumed equal 0.8 which is the elliptical crack equilibrium shape [42].

The next step in the analysis was identification of the best distribution describing fatigue data. Only the normal, lognormal, Gumbel and two parameter Weibull distributions were taken under consideration. The best fit, both for old and new pedigree materials was obtained for lognormal distribution with correlation coefficients 0.84 and 0.91 respectively. Comparison of the data with the best fit lines on both linear and lognormal probability plots is shown in Figure 53. The fit could be improved by using either three parameter distributions or fitting separately low and high cycle-to-failure ranges, but that would preclude use of the propose method. It was thus assumed that the fatigue lives can be adequately described using lognormal distributions.

Obtained data were subsequently used to estimate averages and variances of the fatigue lives assuming:
a. fractographically measured pore size distributions as random variables (designated as Pore Data in Table 17)
b. predicted extreme pore size distributions from weighted Gumbel parents as random variable (designated as Extreme/Pores)
c. texture described by Taylor factors as random variable (Designated as Extreme/Texture)
d. both predicted extreme pore sizes and texture as random variables (designated as Extremes/Pores and Texture).

The obtained average cycles to failure and their variances are listed in Table 17. They were used to generate cumulative lognormal fatigue life distributions using parameters obtained from relations:

$$\mu = \overline{\ln N_f} \qquad (37)$$

$$\sigma = V_{\ln N_f} \qquad (38)$$

The predictions can be compared with the experimental data, for both studied alloys, in Figure 54.

For the old alloy the predictions obtained using fractographic pore size data are the best. Other predictions for old material underestimate short fatigue lives but adequately described data in the long life ranges. The predictions for the new alloy are more accurate. The best agreement for short fatigue lives are for the pore sizes estimated using extreme values. For long fatigue lives the predictions are the best when both the pore size and texture variations are taken into account. This suggests that the low fatigue lives are controlled by the size of the largest pores while longest lives are influenced by the distribution of microstructural features on the crack path.

In summary, it appears that the approximation of fatigue lives using the proposed method is quite accurate, particularly for new pedigree alloy. It is also worth noting that the estimates of crack initiating pore sizes obtained using extreme value approach give excellent predictions when used as input to the fatigue life prediction model. This suggests that the extreme value method of estimating pore sizes together with the fracture mechanics approach can serve as starting blocks for developing a microstructure based life prediction methodology. We are currently working on the refinement of the method, particularly on finding the means of incorporating crack deflection into the model. We are also verifying the predictive capabilities of the model for the case of the open hole fatigue samples.

ii. Markov Chain Model

A complete description of fatigue process require incorporation of several specialized models for different stages of fatigue life. This kind of approach is necessary to accommodate different sequences of events ...ng to the final failure. We proposed to use Markov chain model for ...rpose [38].

...e core of the Markov chain approach is a matrix containing pr... abilities of transitions between different states. In our case such a matrix will consist of the probabilities of crack moving forward from one position to another, and it will have following general form:

$$
\mathbf{P} = \begin{bmatrix}
p_{11} & p_{12} & p_{13} & \cdot\cdot & \cdot\cdot & p_{1n} \\
0 & p_{22} & p_{23} & \cdot\cdot & \cdot\cdot & p_{2n} \\
0 & 0 & p_{33} & \cdot\cdot & \cdot\cdot & p_{3n} \\
\cdot & \cdot & \cdot & \cdot\cdot & \cdot\cdot & \cdot \\
\cdot & \cdot & \cdot & \cdot\cdot & \cdot\cdot & \cdot \\
0 & 0 & 0 & \cdot\cdot & \cdot\cdot & 1
\end{bmatrix} \quad (39)
$$

where p_{11} is the probability that initial crack does not grow during some predetermined number of cycles, called duty cycle, p_{12} is the probability that cracks grows one step forward and so on. The last column contains probabilities of catastrophic failures for different crack lengths. All terms below matrix diagonal are zero, because crack healing has been excluded.

The distribution of initial crack lengths can be incorporated into the model by assigning different probabilities to the initial crack positions through the so called probability vector:

$$
\mathbf{v} = (v_1, v_2, v_3, .., v_n) \quad (40)
$$

where $\sum_{i=1}^{n} v_i = 1$, v_1 is the fraction of cracks with the smallest lengths, v_2 is fraction of cracks with lengths corresponding to the second position in the transition matrix etc. Finding distribution of crack lengths after one duty cycle can be then calculated from [32, 38]:

$$v_1 = v \cdot P \qquad (41)$$

and after n duty cycles it is described by a vector:

$$v_n = v \cdot P^n \qquad (42)$$

The last component of the probability vector is of particular interest as it describes the cumulative probability of failure. Plotting the value of that component versus number of duty cycles gives plot of cumulative failure probabilities.

Up to date we have tested the most basic version of the above Markov chain model for its ability to reproduce the expected behaviors. The model used by us, the B-model [38], assumes that probability matrix has following form:

$$P = \begin{bmatrix} p & q & 0 & .. & 0 & 0 \\ 0 & p & q & .. & 0 & 0 \\ 0 & 0 & p & .. & 0 & 0 \\ .. & .. & .. & .. & .. & .. \\ 0 & 0 & 0 & .. & p & q \\ 0 & 0 & 0 & .. & .. & 1 \end{bmatrix} \qquad (43)$$

which means that the model assumes that after one duty cycle probability that crack does not grow is p and that it grows on unit forward is q. The optimum size of the matrix, n, and the probabilities p and q which best fit fatigue data can be calculated from equations[38]:

$$p + q = 1 \qquad (44)$$

$$\overline{N} = (n-1)\left(1 + \frac{p}{q}\right) \qquad (45)$$

$$\sigma^2 = (n-1)\left(1 + \frac{p}{q}\right)\frac{p}{q} \qquad (46)$$

where $\overline{N}$ and σ are average and standard deviation of the number of cycles to failure. The cumulative failure probability after x duty cycles, $F(x;\ 1,\ n)$, can be in this case calculated from expression [38]:

$$F(x;1,n) = \sum_{i=n-1}^{x} \binom{i-1}{i-n+1} p^{i-n+1} q^{n-1} \qquad (47)$$

The above model was tested on the fatigue data for 7050-T7451 alloys obtained by Owen et al.[44]. The results of the best fit, solid lines, are compared with the experimental data in Figure 55. The probability vector used in the calculations for both alloys was (1, 0, 0, ..). The results show that the optimum matrix size is 12 for the old alloy and 27 for the new pedigree data. As a consequence, the probability p that crack moves forward during each duty cycle is larger for the new than for the old alloy. To eliminate this anomaly it was necessary to sacrifice best fit for the new alloy to obtain the same size of the transition matrix for both alloys. The result is shown as dotted line in Figure 55. The probabilities p and q for both alloys can be now directly compared and they indicate that the probability that crack moves forward during each duty cycle in an old alloy is twice that of the new one.

The model has been also interrogated to find if it correctly reacts to the increased initial crack sizes and to the changes in the crack growth rates. The increased crack size was simulated by changing the staring probability vector. Results from one of such simulation for twelve-step model for new alloy are in Figure 56. They show that by increasing initial crack size in the new alloy to the one corresponding to position number six

in the probability vector, the new alloy would have the distribution of fatigue life similar to that of the old alloy.

The changes of the crack growth rates were simulated by changing some of the values in the transition matrix. Figure 57a shows change in the failure distribution function when the value of p in the first row of the transition matrix was changed from 0.922 to 0.95. This simulates initial retardation of the crack growth. As expected, the distribution curve shifted to the right. When all p values were changed to 0.95 the change in the fatigue life distribution, as shown in Figure 57b, was more significant.

The interrogation of the Markov chain model showed that it is capable of reproducing all expected behaviors. The components of the probability matrix have been obtained by the best fit method, but they can be alternatively coupled to the probabilities of the microscopic crack propagation events through appropriate crack nucleation and crack propagation models. Based on the results of the fatigue life predictions obtained by us and by Alcoa group for the 7050 alloys, the crack propagation models alone are sufficient to describe fatigue life distribution in the studied alloys [34]. Hence it appears that there may be no need for model integration using Markov chain approach. However, the nucleation models will have to be employed, as we anticipate in the case of 7050 alloys with low porosity levels and small constituents, the Markov chain approach will become a viable tool for their integration.

F. Summary of the Technical Accomplishments

- The focus during the reporting period was on the characterizations of the starting microstructures in the "high" and "low" porosity 7050-T7451 commercial alloys at the surface, quarter depth and center locations within the plates and on the development of the fatigue life prediction models. Up to date we have completed characterizations of the grain structures, constituent particles, pores and precipitates in both alloys. This is the first ever exhaustive microstructural characterizations of the 7050-T7451 plate alloys that we are aware of. The characterizations have been made possible by the use a new

version of the linear intercept method which has been developed as part of this investigation and which is ideally suited for detecting microstructural inhomogeneities.

- Both investigated alloys were partially recrystallized. The recrystallization levels varied from 2% at the surface to 20% in the plates center regions. The unrecrystallized grain sizes were from 45 to 220 μm, while recrystallized grains were 22 to 54 μm. The new pedigree alloy had finer grain structure with average unrecrystallized grain size of 87 μm. Recrystallized grains in the new alloy were 38 μm in size. The sizes of unrecrystallized and recrystallized grains in the old alloy were 138 and 34 μm respectively. In both alloys the unrecrystallized grains were elongated with average aspect ratios of 2.62. Both unrecrystallized and recrystallized grains had normal size distributions.

- The volume fractions, sizes and spatial distributions of the constituent particles and pores have been measured using the intercept method and the tessellation technique. The average sizes of the pores were 3.39 μm for the old and 3.47 μm for the new alloys with the corresponding area fractions of 0.134% and 0.102%. The average sizes of the constituent particles were 4.77 and 4.02 μm and area fractions 0.70% and 0.61% for the old and new pedigree alloys respectively. Our results showed that the new pedigree alloy contains 24% less pores and 13% less constituent particles than the old one. The size distributions of pores and constituent particles were lognormal and their spatial distributions were random with clusters.

- The most common precipitating phases present in the alloy were η', η_1, η_2 and η_4-variants of the η phase ($MgZn_2$). The precipitates inside the grains were small, ranging from 5 to 45 nm in diameters, while those on the grain boundaries were generally larger with sizes between 20 - 250 nm.

- Fractographic analysis of the new pedigree open hole fatigue samples showed that the fatigue fracture surface roughness and fractal dimension change along the crack path. Both the roughness parameter and fractal dimension are the smallest near the crack initiation site, increase gradually with crack length and eventually

level off at the fast failure region. Further characterizations of the fracture surfaces are in progress.

- Metallographic and fractographic pore size distributions for smooth fatigue samples have been analyzed using the statistics of extremes. It was possible to show that the crack initiating pore sizes were extreme values of the parent pore size distributions obtained from metallographic characterizations. The best predictions of crack initiating pore sizes have been obtained by approximating parent distribution with Gumbel cdf and using sample size equal to number of pores in the sample surface layer about average pore size thick.

- The predictive capabilities of two types of life prediction models have been studied. The first model was of the Paris/Erdogen type with initial crack sizes, texture and crack deflections as stochastic variables. The model allowed for the prediction of the distributions of fatigue lives and for the study of the effects of different stochastic variable and their combinations on the predictions. The model has very good predictive capabilities, particularly for the new pedigree alloy. *The second tested model was of the Markov chain type.* Interrogation of this model showed that it was capable of correctly predicting changes in fatigue lives due to the fluctuations in the initial crack sizes and nucleation and growth rates. This model is intended for linking several specialized microstructural models describe different stages of fatigue life.

G. Future Efforts

1. Complete fractographic characterizations of the 7050-T7451 new and old pedigree plate alloys including characterizations of the fracture surface profiles and identification of the microstructural features on the crack path.

2. Initiate microstructural and fractographic characterizations of the low porosity and thin plate variants of the 7050 alloys.

3. Refine extreme value methodology for predicting size distributions of the fatigue crack initiating microstructural features.

4. Incorporate results of the microstructural characterizations into the next versions of the life prediction models.

H. Acknowledgments

I. Publications and Presentations

PUBLICATIONS:

1. J. Zhang, A. J. Luévano and M. A. Przystupa, "Quantitative Analysis of Heterogeneous Grain Structures on Plane Sections", Scripta Metallurgica et Materialia, vol. 26, pp. 1061 - 1066, 1992.

2. J. Zhang, A. J. Luévano and M. A. Przystupa, " Microstructural Models for Quantitative Analysis of Grains and Second-Phase Particle Shapes", submitted to Materials Characterization.

3. A. J. Luévano, M. A. Przystupa and J. Zhang, "Accumulation of Microstructural Damage Due to Fatigue of High Strength Al Alloys", in preparation.

4. J. Zhang, A. J. Luévano and M. A. Przystupa, "Analysis and Modeling of the Second Phase Populations in the Aluminum 7050 Alloy", in preparation.

5. A. J. Luévano, M. A. Przystupa and J. Zhang, "Characterization of Precipitate Microstructure on the Grain Boundaries of 7050 T7451 Aluminum Alloy", in preparation.

PRESENTATIONS:

1. M. A. Przystupa, J. Zhang, A. J. Luévano, "The Effect of Microstructural Fluctuations on the Fatigue Life Distributions in Aluminum Alloys", TMS Annual Meeting in San Diego, March 1-5, 1992.

2. J. Zhang, A. J. Luévano and M. A. Przystupa, "Quantitative Evaluation of Grain Sizes and Shapes of Aluminum 7050 Alloys", TMS Annual Meeting in San Diego, March 1-5, 1992.

3. A. J. Luévano, J. Zhang and M. A. Przystupa, "Precipitate Phase Identification and Grain Boundary Precipitate Characterization of the Aluminum Alloys 7050 in the T7 Temper", TMS Annual Meeting in San Diego, March 1-5, 1992.

4. M. A. Przystupa, J. Zhang and A. J. Luévano, "Distribution of Microstructural Features on the Fatigue Crack Path in Aluminum 7050 Alloy", TMS Fall Meeting in Chicago, November 2-5, 1992.

5. A. J. Luévano, J. Zhang and M. A. Przystupa, "Characterization of Grain Boundary Precipitates in the Aluminum 7050-T7451 Alloy", TMS Fall Meeting in Chicago, November 2-5, 1992.

6. J. Zhang, A. J. Luévano and M. A. Przystupa, "Quantitative Characterizations of Pores and Constitutive Particles in the Aluminum 7050 Alloy", TMS Fall Meeting in Chicago, November 2-5, 1992.

7. J. Zhang, A. J. Luévano and M. A. Przystupa, "Quantitative Analysis of Fatigue Fracture Surfaces of the Aluminum 7050 Alloy", TMS Annual Meeting, Denver, February 21-25, 1993.

8. M. A. Przystupa, J. Zhang and A. J. Luévano, "Predictions of the Size Distributions of the Fatigue Crack Initiating Flaws", TMS Annual Meeting, Denver, February 21-25, 1993.

9. M. A. Przystupa, "Estimation of the Size Distributions of the Fatigue Crack Initiating Pores in Aluminum Alloys", invited presentation, Conference on Extreme Value Theory and its Application, Gaithersburgh, Md., May 2-7, 1993.

10. A. J. Luévano, J. Zhang and M. A. Przystupa, "Accumulation of Microstructural Damage During Fatigue of High Strength Al Alloys", AeroMat'93, Anaheim, Ca., June 7-10, 1993.

J. References

1. M. A. Przystupa, ONR Proposal Titled "Development of the Microstructure Based Stochastic Life Prediction Models", Dep. of Material Sci. and Eng., UCLA, November 1990.

2. M. A. Przystupa, Progress Report, ONR Grant No: N00014-91-J-1299, UCLA, June 1991

3. M. A. Przystupa, Progress Report, ONR Grant No: N00014-91-J-1299, UCLA, February, 1992.

4. J. Zhang, A. J. Luévano and M. A. Przystupa, "Quantitative Analysis of Heterogeneous Grain Structures on Plane Sections", Scipta Metallurgica et Materialia, 26, pp 1061-1066, (1992).

5. J. Zhang, A. J. Luévano and M. A. Przystupa, "Microstructural Models for Quantitative Analysis of Grains and Second-Phase Particles," Submitted to *Materials Characterization.*

6. S. I. Tomkeieff, "Linear Intercepts, Areas and Volumes", *Nature*, 155, pp. 24, January, (1945).

7. J. A. Szpunar and B. K. Tanner, J. of Mater. Sc., vol. 19, p. 3254, 1984.

8. H.-J. Bunge, "Texture Analysis in Materials Science", Butterworth & Co 1982.

9. P. J. Wray, O. Richmond, H. L. Morrison, Metallography, vol. 16, p. 39, 1983.

10. W. A. Spitzig, J. F. Kelly, O. Richmond, Metallography, vol. 18, p. 235, 1985.

11. M. A. Przystupa, "Application of the Dirichlet Tessellation Procedure for Microstructure Characterization", Progress Report DM16-1, Alcoa Laboratories, Alloy Technology Div., 1985

12. A. Uguz and J. W. Martin, Materials Characterization, vol.27, pg. 147 (1991)

13. P.M.. Kelly, A. Josten, R. G. Blake and J. G. Napier, Phys. Stat. Sol. 31A, pg. 771 (1975)

14. M. Coster and J. L. Chermant, Int. Metals Rev., vol. 28, p. 228, 1983.

15. S. M. El Soudani, Metallography, vol. 11, p. 247, 1978.

16. E. E. Underwood, "Recent Advances in Quantitative Fractography", in Fracture Mechanics: Microstructure and Micromechanisms, ed. by S. V. Naïr et al., p. 87, ASM International, Metals Park, Ohio, 1989.

17. A. M. Gokhale and E. E. Underwood, "A general method for estimation of fracture surface roughness: Part I. Theoretical Aspects", Met. Trans. A, vol. 21A, pp 1193-1199, May 1990.

18. A. M. Gokhale and W. J. Drury, "A general method for estimation of fracture surface roughness: Part II. Practical Considerations", Met. Trans. A, vol. 21A, pp 1201-1207, May 1990.

19. B. B. Mandelbrot: The Fractal Geometry of Nature, W. H. Freeman and Company, New York, NY, 1982.

20. J. Cheng, M. Yuan, C.N.J. Wagner and A.J. Ardell, "Fractographic fingerprinting of proton-irradiation-induced disordering and amorphization of intermetallic compounds", J. Mater. Res., Vol. 4, No. 3, pp565-78, May/June 1989.

21. H. C. Hamaker, "approximating the cumulative normal distribution and its inverse", Applied Statistics, vol. 27, pp76-79, (1978).

22. P. Magnusen, A. J. Hinkle, R. J. Bucci, R. L. Rolf and D. A. Lukasak, "Methodology for the Assessment of Material Quality Effects on Airframe Fatigue Durability," Alcoa Lab. Technical Report, No. 57-89-40.

23. J. K. Park and A. J. Ardell, Metallurgical Transactions A, vol 14A, pp. 1957, (1983).

24. Unwin and Nicolson, Acta Metall vol 17, pp. 1379, (1969).

25. J. K. Park and A. J. Ardell, Acta Metall. vol. 34, No. 12, pp. 2399-2409, 1986.

26. A. J. Ardell, Acta Metall, vol 20, pp 601, (1972).

27. P. E. Magnusen, A. J. Hinkle, W. T. Kaiser, R. J. Bucci and R. L. Rolf, "Durability Assessment Based on Initial Material Quality", Alcoa Laboratories Report No. 57-89-07.

28. D. J. Alexander, "Quantitative analysis of fracture surfaces using fractals", Quantitative Methods in Fractography, ASTM STP 1085, B. M. Strauss and S. K. Putatunda, Eds., American Society for Testing and Materials, Philadelphia, pp 39-51, 1990.

29. E. J. Gumbel, "Statistics of Extremes", Columbia University Press, New York, 1958.

30. E. Castillo, "Extreme Value Theory in Engineering", Academic Press, Inc., San Diego, 1988.

31. H. Cramer, "Mathematical Methods of Statistics", Princeton University Press, Princeton, 1946.

32. W. Feller, "An Introduction to Probability Theory and Its Application", vol. I, 3rd edition, John Wiley & Sons, Inc., New York, 1968.

33. E. E. Underwood, "Quantitative Stereology", Addison-Wesley Publishing Company, Inc., Reading, Mass., 1970.

34. J. R. Brockenbrough, R. J. Bucci, A. J. Hinkle, J. Liu, P. E. Magnusen and S. M. Miyasato, "Role of Microstructure on Fatigue Durability of Aluminum Aircraft Alloys", Alcoa Laboratories Progress Report, ONR contract No. F33615-92-C-5915, Alcoa Center, PA, April 1993.

35. J. Pickands III, The Annals of Statistics, vol. 3, No. 1, pp. 119-131, 1975.

36. S. Suresh, "Fatigue of Metals", Cambridge University Press, Cambridge, 1992.

37. "Probabilistic Fracture Mechanics and Reliability", ed. by J. W. Provan, Martinus Nijhoff Publishers, Dordrecht, The Hetherlands, 1987.

38. J. L. Bogdanov and F. Kozin, "Probabilistic Models of Cumulative Damage", John Wiley & Sons, Inc., New York, 1985.

39. D. W. Hoeppner and W. E. Krupp, Eng. Fract. Mech., vol. 6, p. 47, 1974.

40. J. N. Yang, W. H. Hsi, S. D. Manning and J. L. Rudd, "Stochastic Crack Growth Models for Applications to Aircraft Structures", in "Probabilistic Fracture Mechanics and Reliability", ed. by J. W. Provan, Martinus Nijhoff Publishers, Dordrecht, The Netherlands, 1987.

41. P. M. Besuner, "Probabilistic Fracture Mechanics" in "Probabilistic Fracture Mechanics and Reliability", ed. by J. W. Provan, Martinus Nijhoff Publishers, Dordrecht, The Netherlands, 1987.

42. I. S. Raju and J. C. Newman, in Fracture Mechanics: Seventeenth Volume, ASTM, STP 905, ed. by J. H. Underwood et al., pp. 789-805, ASTM, Philadelphia, 1986.

43. H. J. Bunge, Kristall und Technik, v. 5, pp. 145-175, 1970.

44. C. R. Owen, R. J. Bucci and R. J. Kegarise, J. of Aircraft, vol. 26, pp. 178-184, 1989.

K. Tables and Figures

Table 1. Characteristics of the Recrystallized Grains on Indicated Planes and
Positions within the Plate 7050-T7451 Alloys

Sample	Diameter (um)	Area%	AspectRatio	Shape Index	No. of Grains
New Pedigree					
TL, center	54.2301	21.97	1.8277	0.7068	173
LS, center	40.6966	17.48	2.2863	0.6541	197
ST, center	36.0557	17.22	1.9666	0.6725	249
TL, surface	36.5036	3.061	1.7063	0.5996	15
LS, surface	32.3285	3.69	2.1274	0.6824	26
ST, surface	40.4698	3.63	2.1404	0.6873	20
TL, quarter	39.4877	21.04	1.8342	0.6842	157
LS, quarter	33.3059	24.21	2.5692	0.5836	170
ST, quarter	29.4681	20.68	2.1308	0.6602	219
Average	38.0607	14.78	2.0654	0.6590	
Old Pedigree					
TL, center	44.5498	17.56	1.9199	0.6773	176
LS, center	35.9728	19.01	2.0837	0.6543	300
ST, center	36.2095	13.96	1.9627	0.6638	208
TL, surface	30.7823	1.13	1.942	0.6939	32
LS, surface	21.8066	0.07	1.9599	0.6965	6
ST, surface	31.1399	0.765	3.8782	0.4847	18
TL, quarter	39.296	2.3	1.9223	0.702	39
LS, quarter	31.2676	1.7787	2.8846	0.5851	48
ST, quarter	33.3381	2.305	2.0546	0.6785	60
Average	33.8181	6.54	2.2898	0.6485	

Table 2. Characteristics of the Unrecrystallized Grains on Indicated Planes
and Positions within the Plate 7050-T7451 Alloys

New Pedigree					
Sampie	Diameter (um)	Area%	AspectRatio	Shape Index	No. of Grains
TL, center	161.5078	78.03	1.9232	0.6935	85
LS, center	103.5287	82.52	3.3236	0.5312	156
ST, center	93.5879	82.78	2.4834	0.6141	203
TL, surface	71.5803	96.94	1.8791	0.6817	199
LS, surface	43.7909	96.31	3.0456	0.5532	367
ST, surface	49.5947	96.37	2.5596	0.6000	235
TL, quarter	111.4990	78.96	1.9268	0.7009	82
LS, quarter	74.8369	75.79	2.8491	0.5781	107
ST, quarter	76.7076	79.32	2.5510	0.6142	131
Average	87.4038	85.22	2.5046	0.6185	
Old Pedigree					
Sample	Diameter (um)	Area%	AspectRatio	Shape Index	No. of Grains
TL, center	116.0530	82.44	1.8024	0.7331	165
LS, center	79.0467	80.99	2.5908	0.5892	250
ST, center	75.9650	86.04	2.3843	0.5987	309
TL, surface	168.8661	98.87	1.8568	0.7041	104
LS, surface	139.3283	99.93	4.2512	0.4709	204
ST, surface	112.4845	99.23	2.8519	0.5737	197
TL, quarter	217.3948	97.70	2.2616	0.6984	72
LS, quarter	188.6366	98.22	3.8484	0.5057	65
ST, quarter	141.6075	97.69	2.8849	0.5766	127
Average	137.7092	93.46	2.7480	0.6056	

Table 3. Normal Distribution Parameters for the Unrecrystallized Grain Sizes on Indicated Planes and Positions within the Plate 7050-T7451 Alloys

New Pedigree					
Sample	Average (um)	Std. Dev.	Confidence, 95%	R^2	No. of Grains
TL, center	144.6696	106.71	22.69	0.8992	85
LS, center	105.9521	66.52	10.44	0.9256	156
ST, center	91.6362	60.12	8.27	0.9385	203
TL, surface	68.5967	43.61	6.06	0.9435	199
LS, surface	46.2802	25.17	2.58	0.9656	367
ST, surface	51.6937	29.89	3.82	0.9549	235
TL, quarter	111.3073	70.04	15.16	0.9204	82
LS, quarter	78.7504	45.38	8.60	0.9487	107
ST, quarter	82.4677	47.36	8.11	0.9509	131
Average	86.8171	54.98	9.5246	0.9386	

Old Pedigree					
Sample	Average (um)	Std. Dev.	Confidence, 95%	R^2	No. of Grains
TL, center	120.2984	69.79	10.65	0.9259	165
LS, center	73.6161	49.64	6.15	0.9221	250
ST, center	66.5111	45.74	5.10	0.8983	309
TL, surface	155.5154	110.52	21.24	0.8991	104
LS, surface	138.8137	95.67	13.13	0.9017	204
ST, surface	115.6617	68.79	9.61	0.9141	197
TL, quarter	190.0848	145.85	33.69	0.8181	72
LS, quarter	177.6609	135.26	32.88	0.8707	65
ST, quarter	143.0734	85.08	14.80	0.9449	127
Average	131.2484	89.59	16.3609	0.8994	

Table 4. Normal Distribution Parameters for the Recrystallized Grain Sizes on Indicated Planes and Positions within the Plate 7050-T7451 Alloys

New Pedigree					
Sample	Average (um)	Std. Dev.	Confidence, 95%	R^2	No. of Grains
TL, center	59.2726	30.0126	4.47	0.9421	173
LS, center	45.9964	20.3647	2.84	0.9422	197
ST, center	35.3065	7.4464	0.92	0.9346	249
TL, surface	39.4288	25.2842	12.80	0.8068	15
LS, surface	37.4699	16.1741	6.22	0.6265	26
ST, surface	32.8986	21.4105	9.38	0.7124	20
TL, quarter	40.3533	22.1218	3.46	0.9196	157
LS, quarter	33.3618	18.7392	2.82	0.9106	170
ST, quarter	33.0203	15.1271	2.00	0.9531	219
Average	39.6787	19.63	4.99	0.8609	

Old Pedigree					
Sample	Average (um)	Std. Dev.	Confidence, 95%	R^2	No. of Grains
TL, center	49.1299	24.1045	3.56	0.9571	176
LS, center	38.3609	17.5119	1.98	0.9591	300
ST, center	36.5098	19.5215	2.65	0.9128	208
TL, surface	33.9072	14.7401	5.11	0.8821	32
LS, surface	21.4674	5.735	4.59	0.3819	6
ST, surface	33.5727	16.5356	7.64	0.7658	18
TL, quarter	42.3891	19.7536	6.20	0.8248	39
LS, quarter	33.6168	16.7448	4.74	0.8901	48
ST, quarter	35.0319	16.9311	4.28	0.8538	60
Average	35.9984	16.84	4.53	0.8253	

Table 5. Characteristics of the Pores on Indicated Planes and Positions
within the Plate 7050-T7451 Alloys

New Pedigree					
Sample	Diameter (um)	Area%	Aspect Ratio	Shape Index	No. of Pores
TL, center	3.5453	0.1139	1.5527	0.8092	195
LS, center	3.6655	0.1987	1.4916	0.8002	231
ST, center	3.9109	0.1358	1.5605	0.8051	200
TL, surface	2.9098	0.0712	1.4707	0.8310	201
LS, surface	2.7290	0.0753	1.5212	0.8151	204
ST, surface	3.0741	0.0745	1.5312	0.8147	197
TL, quarter	3.9116	0.0800	1.5190	0.8152	100
LS, quarter	3.5044	0.0845	1.5153	0.8232	130
ST, quarter	4.0321	0.0927	1.4584	0.8288	132
Average	3.4759	0.1030	1.5134	0.8158	

Old Pedigree					
Sample	Diameter (um)	Area%	Aspect Ratio	Shape Index	No. of Pores
TL, center	3.2685	0.1248	1.5033	0.8108	207
LS, center	4.6850	0.3677	1.4499	0.8339	286
ST, center	5.4834	0.2863	1.5142	0.8203	201
TL, surface	3.0694	0.0709	1.5014	0.8128	157
LS, surface	2.4789	0.0584	1.4039	0.8454	201
ST, surface	2.7267	0.0416	1.4062	0.8417	128
TL, quarter	3.0700	0.1419	1.4536	0.8336	204
LS, quarter	2.6368	0.0418	1.4193	0.8387	122
ST, quarter	3.1114	0.0803	1.4118	0.8430	165
Average	3.3922	0.1349	1.4515	0.8311	

Table 6. Lognormal Distribution Parameters for the Pore Sizes on Indicated Planes and Positions within the Plate 7050-T7451 Alloys

	New Pedigree				
Sample	Average (um)	Std. Dev.	Confidence, 95%	R^2	No. of Pores
TL, center	3.5453	0.1139	0.02	0.8092	195
LS, center	3.6655	0.1987	0.03	0.8002	231
ST, center	3.9109	0.1358	0.02	0.8051	200
TL, surface	3.0363	0.3958	0.05	0.9374	201
LS, surface	2.9026	0.4231	0.06	0.9033	204
ST, surface	2.2268	1.4275	0.20	0.8601	197
TL, quarter	3.6212	1.5306	0.30	0.9293	100
LS, quarter	3.5281	1.4478	0.25	0.9492	130
ST, quarter	3.1765	1.5469	0.26	0.8980	132
Average	3.2904	0.8022	0.1317	0.8769	
	Old Pedigree				
Sample	Average (um)	Std. Dev.	Confidence, 95%	R^2	No. of Pores
TL, center	3.0239	0.4866	0.07	0.9571	207
LS, center	3.6682	0.6410	0.07	0.9771	286
ST, center	3.8713	0.5666	0.08	0.8898	201
TL, surface	2.8687	1.3655	0.21	0.8738	157
LS, surface	2.6069	1.3650	0.19	0.9059	201
ST, surface	2.3801	1.4152	0.25	0.8163	128
TL, quarter	2.6869	1.4899	0.20	0.8895	204
LS, quarter	2.5437	1.3993	0.25	0.8369	122
ST, quarter	3.0161	1.4329	0.22	0.8798	165
Average	2.9629	1.1291	0.1709	0.8918	

Table 7. Results of the Tessellation Analysis for Porosities in the Old 7050-T7451 Plate Alloy
(ST Plane, Center Section)

	Average	Minimum	Maximum	St. Dev.	Geom.Av.	Median
Near-Neighbor. (μm)	114.	2.83	324	65.3	91.5	116
Nearest-Nbr. (μm)	48.2	2.83	156	33.2	35	42.5
Local V.F. %	.00502	.00013	.156	.0141	.00168	.00146
Particle Area (μm^2)	30.8	2.30	520	61.9	14.1	11.7
Cell Area (mm^2)	.0108	.00044	.033	.00714	.00842	.00952
Particle Width (μm)	3.12	0.792	18.7	2.34	2.64	2.32
Particle Len. (μm)	4.47	1.04	22.6	3.12	3.84	3.5
Part. Aspect Ratio	1.51	1.01	4.42	.509	1.45	1.36
Neighbor Pos. (^{0})	3.26	-180.	180.			
Particle Orient. (^{0})	96.3	.000	180.			
Cell Sides No.	5.74	3.00	15.0			

Table 8. Characteristics of the Constituent Particles on Indicated Planes and Positions within the Plate 7050-T7451 Alloys

Sample	Diameter (um)	Area%	Aspect Ratio	Shape Index	No. of Particles
New Pedigree					
TL, center	6.2600	0.5416	1.7783	0.7479	204
LS, center	4.8355	0.4803	2.3484	0.6633	179
ST, center	3.6955	0.8453	2.2656	0.6627	322
TL, surface	3.4433	1.1247	2.3377	0.6738	245
LS, surface	3.3464	0.7445	2.4064	0.6516	223
ST, surface	2.9721	0.4575	2.0540	0.7119	213
TL, quarter	3.7220	0.3503	2.3256	0.6712	203
LS, quarter	4.1315	0.6381	2.4782	0.6590	208
ST, quarter	3.7689	0.3489	2.5261	0.6460	212
Average	4.0195	0.6146	2.2800	0.6764	
Old Pedigree					
TL, center	6.1387	0.6287	2.0561	0.7041	204
LS, center	6.3764	0.5239	2.3582	0.6554	201
ST, center	4.5700	0.9070	1.6211	0.7896	236
TL, surface	4.0404	0.7458	1.7119	0.7691	201
LS, surface	3.6416	0.5450	1.8957	0.7361	214
ST, surface	3.1187	0.4530	1.7610	0.7599	219
TL, quarter	5.6655	0.8387	1.7750	0.7614	202
LS, quarter	4.3843	0.7082	1.7676	0.7611	210
ST, quarter	4.9880	0.9311	1.8655	0.7472	212
Average	4.7693	0.6979	1.8680	0.7427	

Table 9. Lognormal Distribution Parameters for the Constituent Particle Sizes on Indicated Planes and Positions within the Plate 7050-T7451 Alloys

New Pedigree					
Sample	Average (um)	Std. Dev.	Confidence, 95%	R^2	No. of Particles
TL, center	6.2600	0.5416	0.07	0.9885	204
LS, center	4.8355	0.4803	0.07	0.6633	179
ST, center	3.6955	0.8453	0.09	0.6627	322
TL, surface	3.7591	0.5101	0.06	0.9151	245
LS, surface	3.7769	0.5335	0.07	0.8964	223
ST, surface	3.4051	0.4607	0.06	0.9076	213
TL, quarter	4.1295	1.4189	0.20	0.9215	203
LS, quarter	4.2891	1.4735	0.20	0.9408	208
ST, quarter	4.0687	1.4439	0.19	0.9408	212
Average	4.2466	0.8564	0.1136	0.8707	

Old Pedigree					
Sample	Average (um)	Std. Dev.	Confidence, 95%	R^2	No. of Particles
TL, center	5.2666	0.6659	0.09	0.9611	204
LS, center	5.7954	0.8333	0.12	0.9926	201
ST, center	3.8105	0.6320	0.08	0.9588	236
TL, surface	4.0729	1.4395	0.20	0.9556	201
LS, surface	4.0081	1.3856	0.19	0.9641	214
ST, surface	3.3401	1.4120	0.19	0.9312	219
TL, quarter	4.7356	1.6811	0.23	0.9428	202
LS, quarter	4.1788	1.5171	0.21	0.9282	210
ST, quarter	4.6203	1.5771	0.21	0.9296	212
Average	4.4254	1.2382	0.1676	0.9516	

Table 10. Results of the Tessellation Analysis for Constituent Particles in the Old 7050-T7451 Plate Alloy
(ST Plane, Center Section)

	Average	Minimum	Maximum	St. Dev.	Geom.Av.	Median
Near-Neighb. (μm)	58.0	1.0	194	38.2	44.0	66.6
Nearest-Nbr. (μm)	25.2	1.0	119	19.2	17.9	21.3
Local V.F. %	.0413	.000262	4.38	.292	.007	.00628
Particle Area (μm^2)	27.8	3.00	266	44.5	14.8	12.2
Cell Area (mm^2)	.0033	.000029	.0216	.0034	.0021	.0022
Particle Width (μm)	2.70	.861	11.5	1.30	2.48	2.37
Particle Len (μm)	4.27	1.46	15.0	2.31	3.84	3.59
Part. Aspect Ratio	1.62	1.02	4.63	.546	1.55	1.45
Neighbor Pos.(^{0})	.603	-180.	180.			
Particle Orient. (^{0})	96.3	.000	180.			
Cell Sides No.	5.76	3.00	15.0			

Table 11. Sizes, area fractions and spacings of the grain boundary precipitates in the old and new pedigree 7050-T7451 alloys.

material	$\langle d \rangle$ (nm)	A_f (%)	N_a (ppts/nm^2)	center-to-center spacing (nm)	surface-to-surface spacing (nm)
new surface	35.5	15.3	1.847×10^{-4}	88.3	55.8
	43.3	14.1	9.565×10^{-5}	112.7	79.4
	46.9	19.8	1.148×10^{-4}	112.0	65.1
	35.5	24.5	2.474×10^{-4}	76.0	40.8
	38.2	31.3	2.725×10^{-4}	72.7	34.5
	38.8	33.6	2.849×10^{-4}	71.1	32.3
	41.3	35.1	2.623×10^{-4}	74.1	32.8
	32.6	14.2	1.735×10^{-4}	91.1	58.5
	34.6	13.2	1.440×10^{-4}	100.0	65.8
	63.8	21.6	6.746×10^{-5}	146.1	82.3
	66.5	11.7	3.377×10^{-5}	206.5	140.0
	42.9	18.3	1.267×10^{-4}	106.6	63.7
new center	167.0	37.0	1.622×10^{-5}	298.0	131.0
	167.0	37.7	1.724×10^{-5}	289.0	122.0
	204.9	41.5	1.259×10^{-5}	338.2	133.3
	235.3	34.3	7.887×10^{-6}	427.3	192.0
	126.3	32.0	2.551×10^{-5}	237.6	111.3
	155.7	33.6	1.767×10^{-5}	285.5	129.8
	60.8	15.5	5.321×10^{-5}	164.5	103.7
	95.6	27.0	3.688×10^{-5}	197.6	101.1
	29.7	5.4	7.855×10^{-5}	135.4	105.7
old surface	37.9	7.4	6.530×10^{-4}	148.5	110.6
	27.0	9.5	1.665×10^{-4}	93.0	66.0
	38.8	12.6	1.665×10^{-4}	116.2	77.4
old center	50.0	12.7	6.486×10^{-4}	149.0	99.0
	31.0	8.5	1.128×10^{-4}	113.0	82.0
	219.3	17.7	1.282×10^{-4}	554.5	335.2
	187.0	52.6	1.910×10^{-4}	274.6	87.6
	36.6	9.0	8.547×10^{-4}	129.8	93.2
	144.6	17.3	1.015×10^{-4}	370.1	225.5
	149.3	49.5	2.824×10^{-4}	225.8	76.5
	138.2	33.5	2.230×10^{-4}	254.1	115.9
	156.6	25.5	1.322×10^{-4}	330.0	173.4

Table 12. Roughness and Fractal Dimension Data for the Fracture Surface of the Open-hole Fatigue Sample. New pedigree 7050 Alloy

Distance from Crack Origin (mm)	Φ_P	ψ	R_L	R_s	m
0	0	1.1562	1.5663	1.8109	1.1048
	60	1.1603	1.2883	1.4947	1.0601
	120	1.1467	1.3982	1.6034	1.0563
3.5	0	1.1742	1.4882	1.7474	1.0864
	60	1.1461	1.5800	1.8107	1.1142
	120	1.1937	1.4794	1.7660	1.0913
10	0	1.2368	1.6206	2.0044	1.1142
	60	1.1431	1.3875	1.5861	1.0751
	120	1.1427	1.5453	1.7659	1.1016

Φ_P angle between the section plane with the surface of the open-hole specimen.

ψ profile structure factor. ψ is completely described by the profile segments orientation distribution function

R_L profile roughness parameter.

R_s surface roughness parameter.

m   fractal dimension.

Table 13. Parameters of the Lognormal Approximations of the Pore Size Parent Distributions and of the Calculated from them Extreme Value Distributions.

Alloy	Standard Fit					Weighted Fit			
	Parent			Extreme		Parent		Extreme	
	μ	σ	R^2	N	R^2	μ	σ	N	R^2
Old	1.572	0.536	0.954	$2.36 \cdot 10^{14}$	0.420	1.151	0.795	$6.41 \cdot 10^7$	0.710
New	1.332	0.623	0.980	$8.93 \cdot 10^7$	0.554	1.626	0.453	$4.78 \cdot 10^{11}$	0.385

Table 14. Parameters of the Gumbel Approximations of the Pore Size Parent Distributions and of the Calculated from them Extreme Value Distributions.

Alloy	Standard Fit					Weighted Fit			
	Parent			Extreme		Parent		Extreme	
	μ	σ	R^2	N	R^2	μ	σ	N	R^2
Old	1.334	0.413	0.983	25,633	0.936	1.544	0.306	424,197	0.95
New	1.048	0.495	0.963	1,868	0.914	1.729	0.197	$6.46 \cdot 10^6$	0.85

μ - average
σ - standard deviation
R^2 - correlation coefficient
N - extreme value distribution sample size

Table 15. Interrogated Areas and/or Volumes Calculated from the Best Estimates of the Extreme Value Distribution Sample Size, N.

Alloy	N_v mm^{-3}	N_a mm^{-2}	No. of Pores in a sample	No. of Surface Pores	Distribut. Type	Fit Type	Sample size for best fit	Interrogated area or volume
Old	25,843	116	1.66·10^8	234,707	Lognormal	Standard	2.36·10^{14}	NA
						Weighted	6.41·10^7	1.37 mm thick surface layer
					Gumbel	Standard	25,633	5.55 mm wide surface band
						Weighted	424,197	8.1µm thick surface layer
New	20,513	76	1.32·10^8	154,039	Lognormal	Standard	8.93·10^7	2.74 mm thick surface layer
						Weighted	4.78·10^{11}	NA
					Gumbel	Standard	1,868	0.62 mm wide surface band
						Weighted	6.46·10^6	157µm thick surface layer

Note: All calculations assume smooth fatigue sample with 12.7 mm diameter and 50.8 mm gage length

N_v - Number of pores per unit volume

N_a - Number of pores per unit cross-section area

NA - sample size greater then the number of pores in a smooth fatigue sample

Table 16. Data Used in the Predictions of the Average Values and Standard Deviations of the Fatigue Lives of the 7050-T7451 Alloys.

Alloy	ln's of the Measured Pore Size Data		ln's of the Predicted Extreme Pore Sizes		ln's of the Taylor Factors, M	
	Average	S. Dev.	Average	S. Dev.	Average	S. Dev.
Old	5.51	0.551	5.69	0.392	1.24	0.171
New	4.86	0.364	4.93	0.253	1.24	0.171

Table 17. Parameters of the Predicted Lognormal Fatigue Life Distributions for the 7050-T7451 Plate Alloys. Assumed Stochastic Variable Indicated in the Column Headers.

Alloy	From Measured Pore Size Data		From Predicted Extreme Pore Size Distrib.		From Texture		From Texture and Predicted Extreme Pore Size Distrib.	
	Aver.	S.Dev.	Aver.	S.Dev.	Aver.	S.Dev.	Aver.	S.Dev.
Old	11.26	0.328	11.08	0.427	11.08	0.342	11.08	0.547
New	11.99	0.446	11.90	0.275	11.90	0.342	11.90	0.438
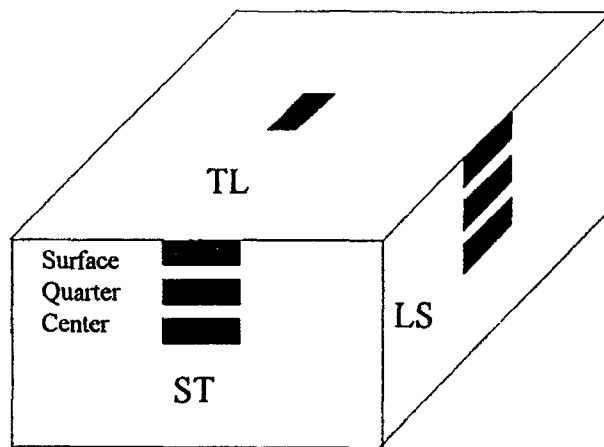
Figure 1. Locations of the metallographic test planes in the Al 7050 plate alloy.

180 μm
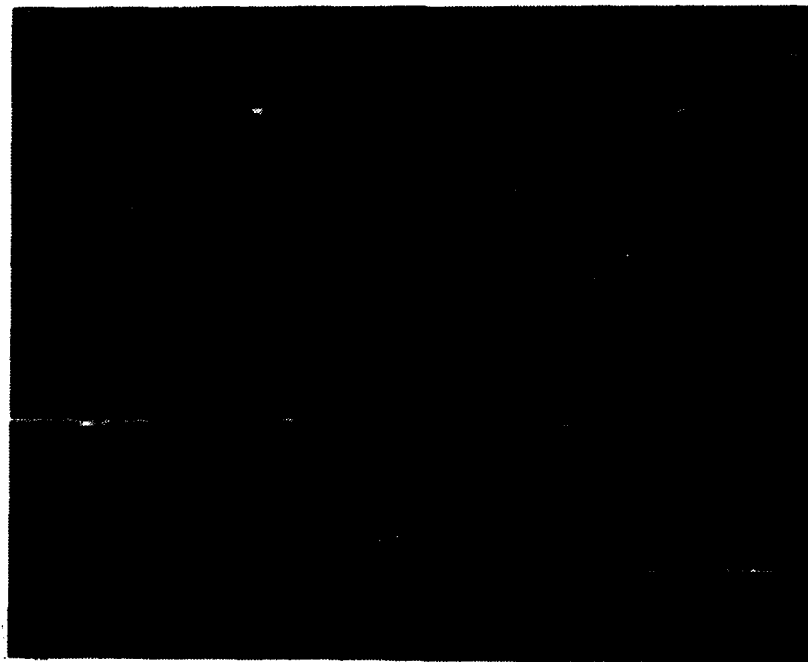
Figure 2. Typical grain structure of the 7050 Al plate alloy showing light recrystallized grains, dark unrecrystallized grains with subgrains and black constituent particles.

65
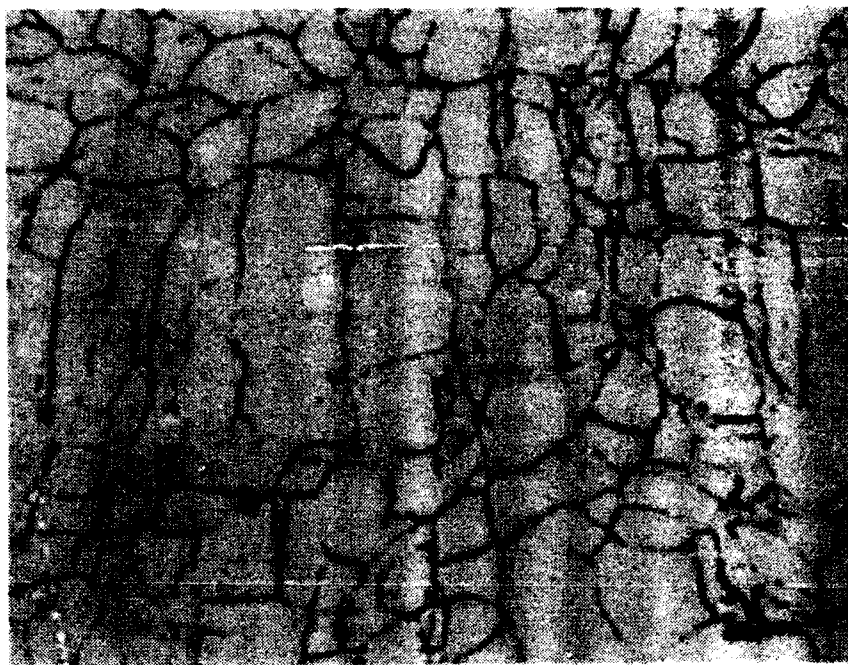
18 μm

Figure 3. Typical subgrain structure of the Al 7050 plate alloy.
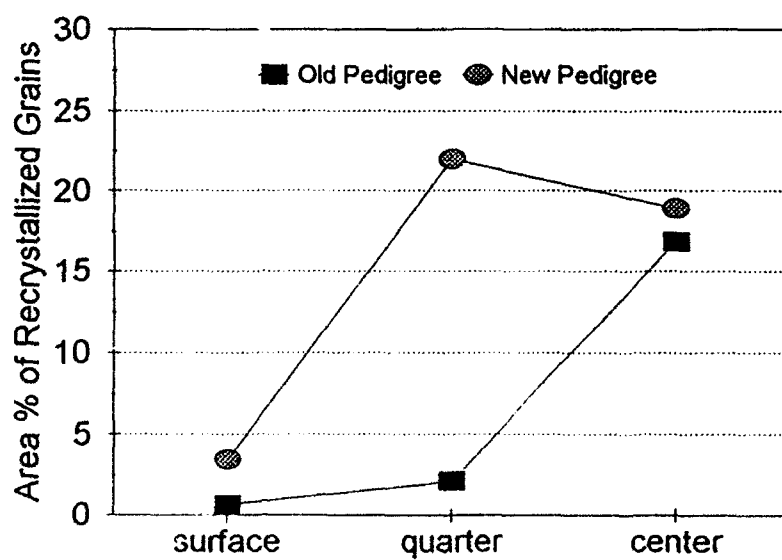
Figure 4. Change of recrystallization levels with location in the Al 7050 plate alloy.
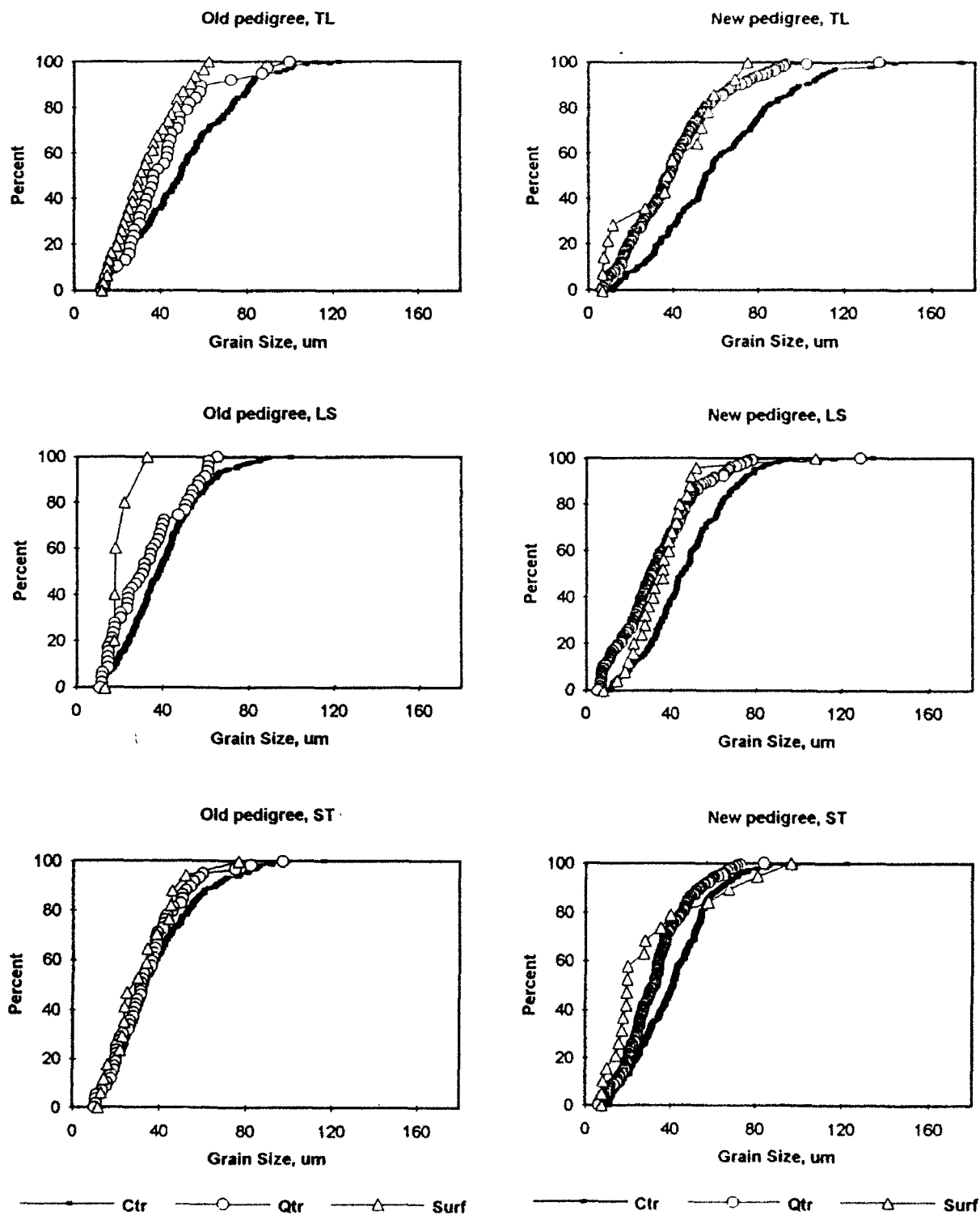
Figure 5. Cumulative distributions of the recrystallized grain sizes in the Al 7050-T7451 plate alloys.
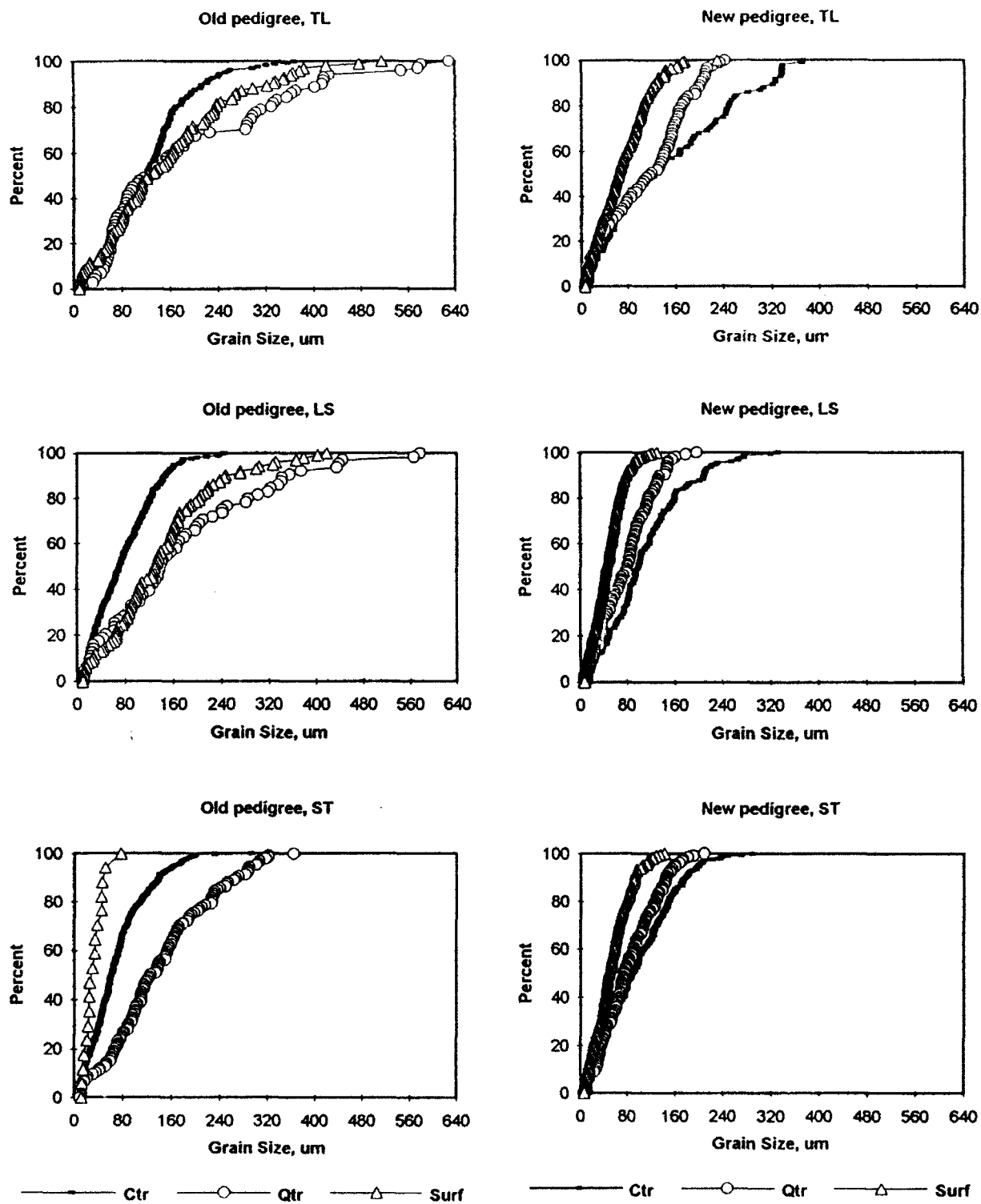
Figure 6. Cumulative distributions of the unrecrystallized grain sizes in the Al 7050-T7451 plate alloys.
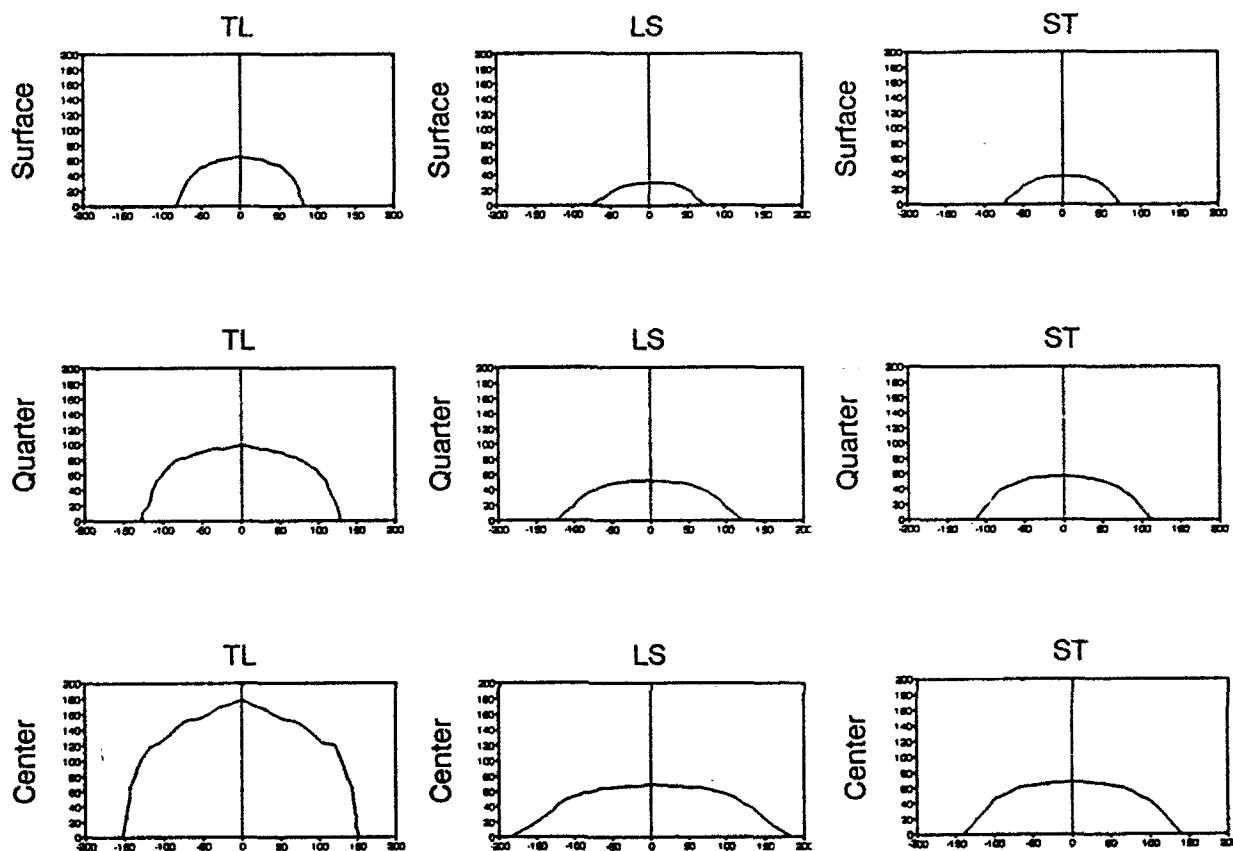
Figure 7. Change of the average dimensions of the unrecrystallized grains with direction for different planes and positions within the plate for *new pedigree* 7050-T7451 alloy. The locations are identified by the labels. All units are in micrometers.
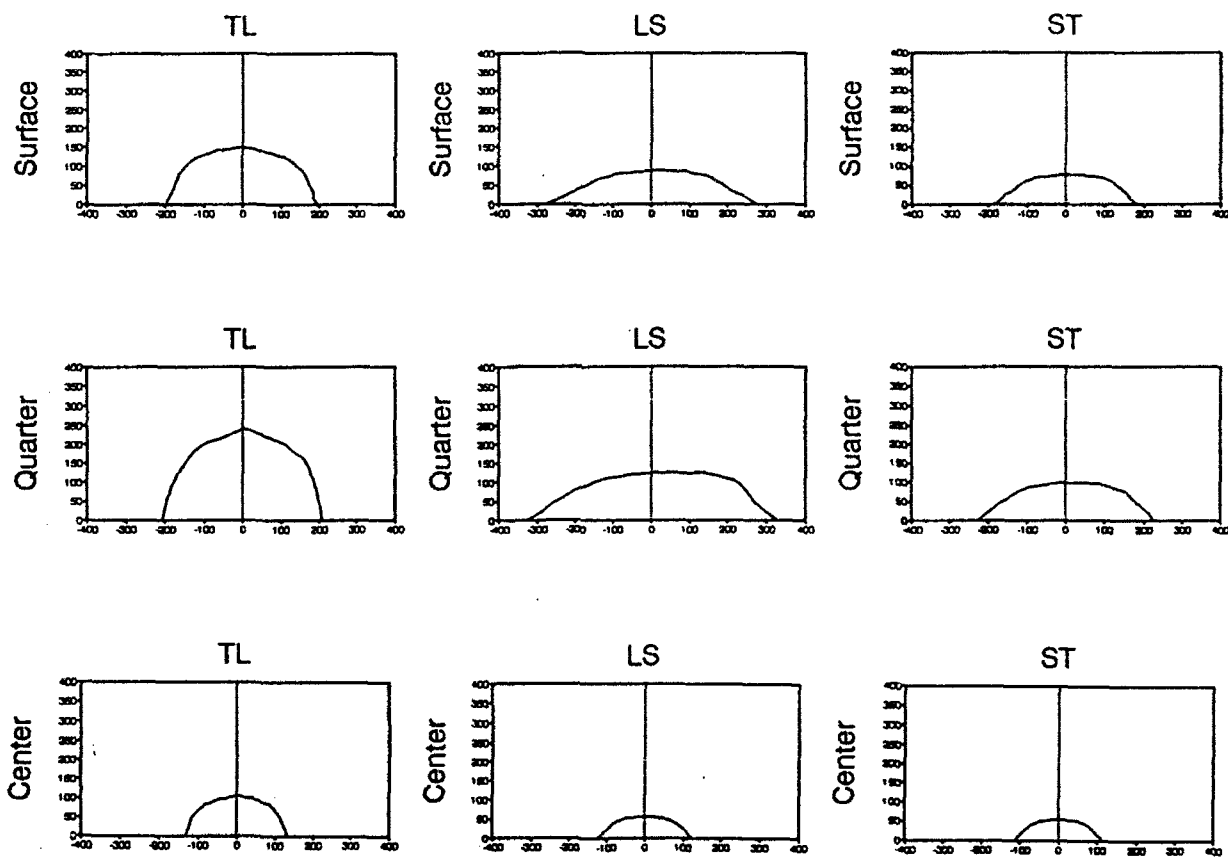
Figure 8. Change of the average dimensions of the unrecrystallized grains with direction for different planes and positions within the plate for *old pedigree* 7050-T7451 alloy. The locations are identified by the labels. All units are in micrometers.
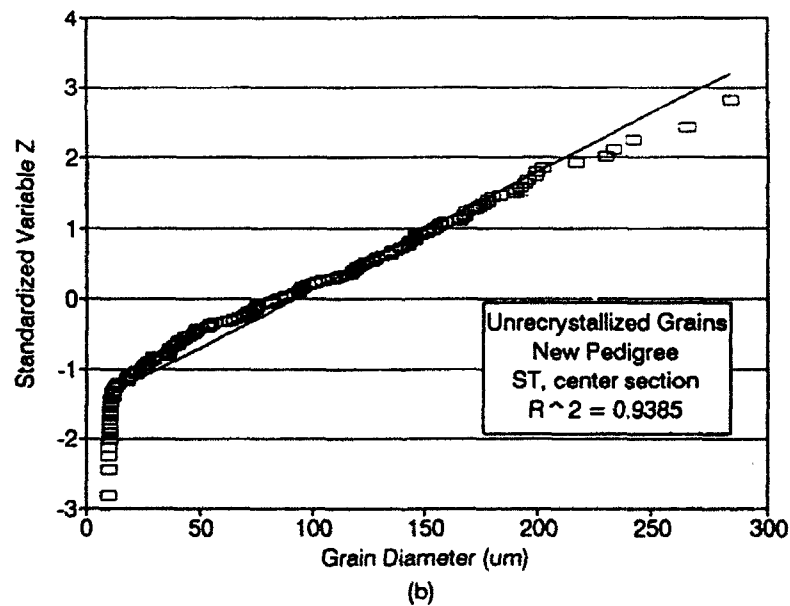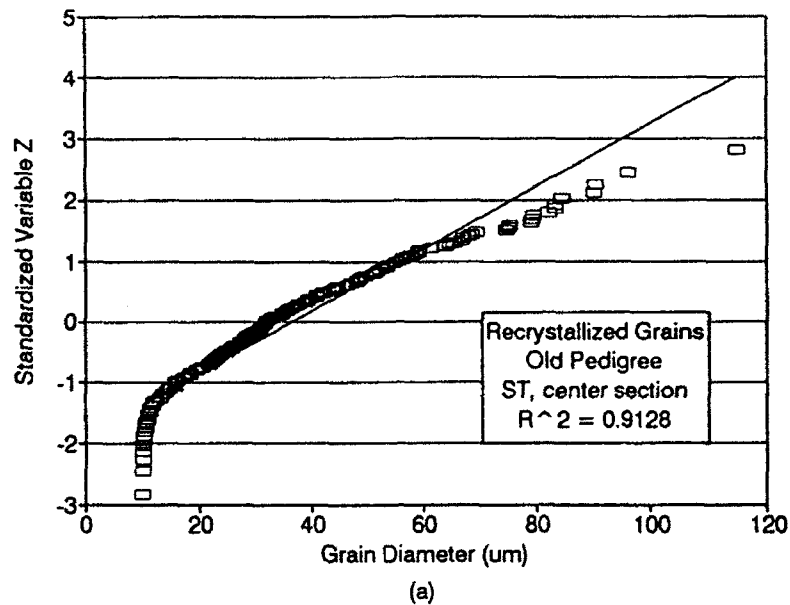
Figure 9. Normal probability plots for the grain size distributions in the 7050 plate alloys: (a) recrystallized grain sizes on ST-plane, center region of the old plate alloy; (b) unrecrystallized grain sizes on ST-plane, center region of the new plate alloy. Solid lines represent the best fit and open squares the experimental data.
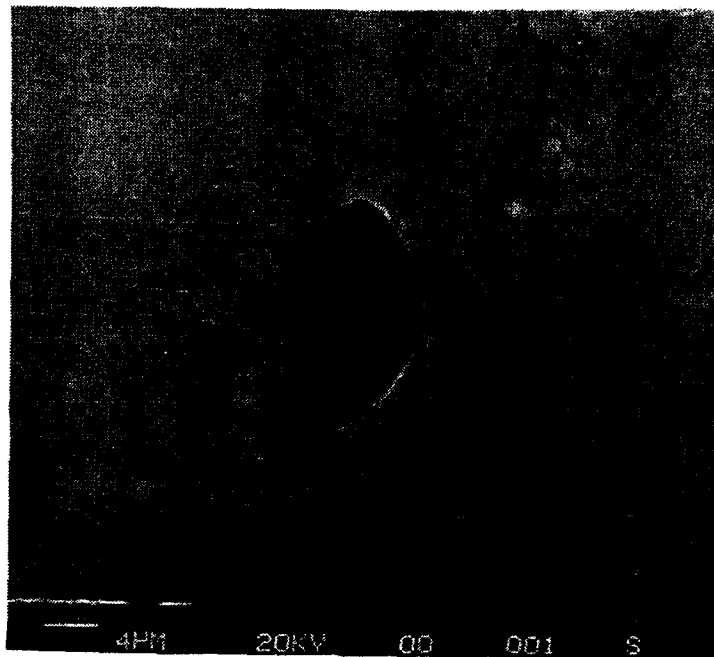
Figure 10. A typical pore in the 7050 Al plate alloy.

Pores in AL 7050
10 um
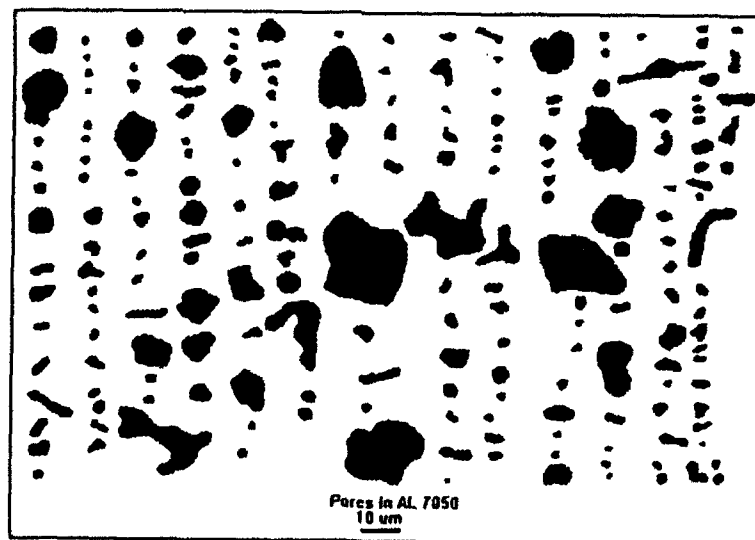
Figure 11. A collection of 201 pores found on the ST-planes, center region of the old pedigree 7050-T7451 plate alloy.
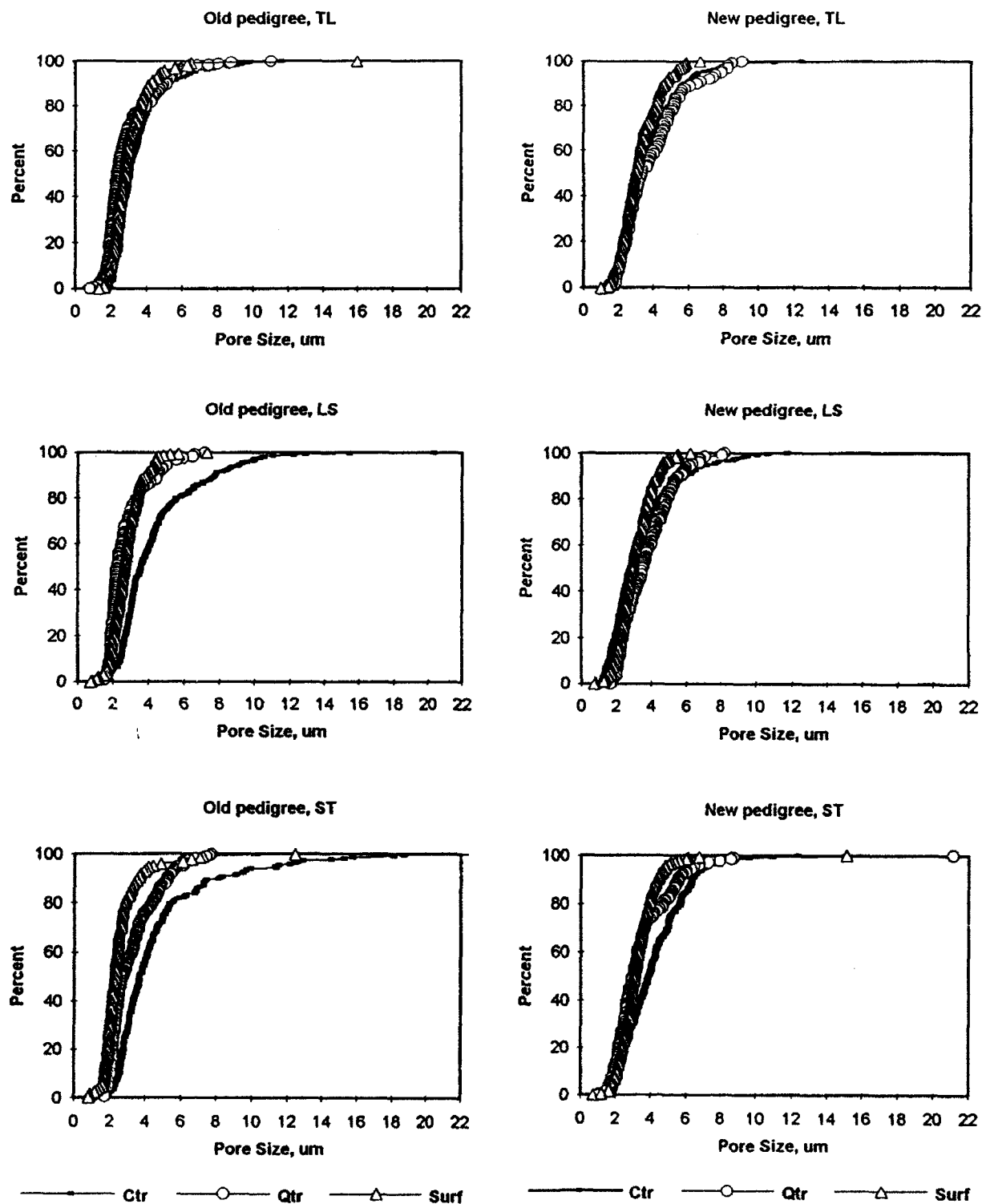
Figure 12. Cumulative pore size distributions in the 7050-T7451 plate alloys.

73
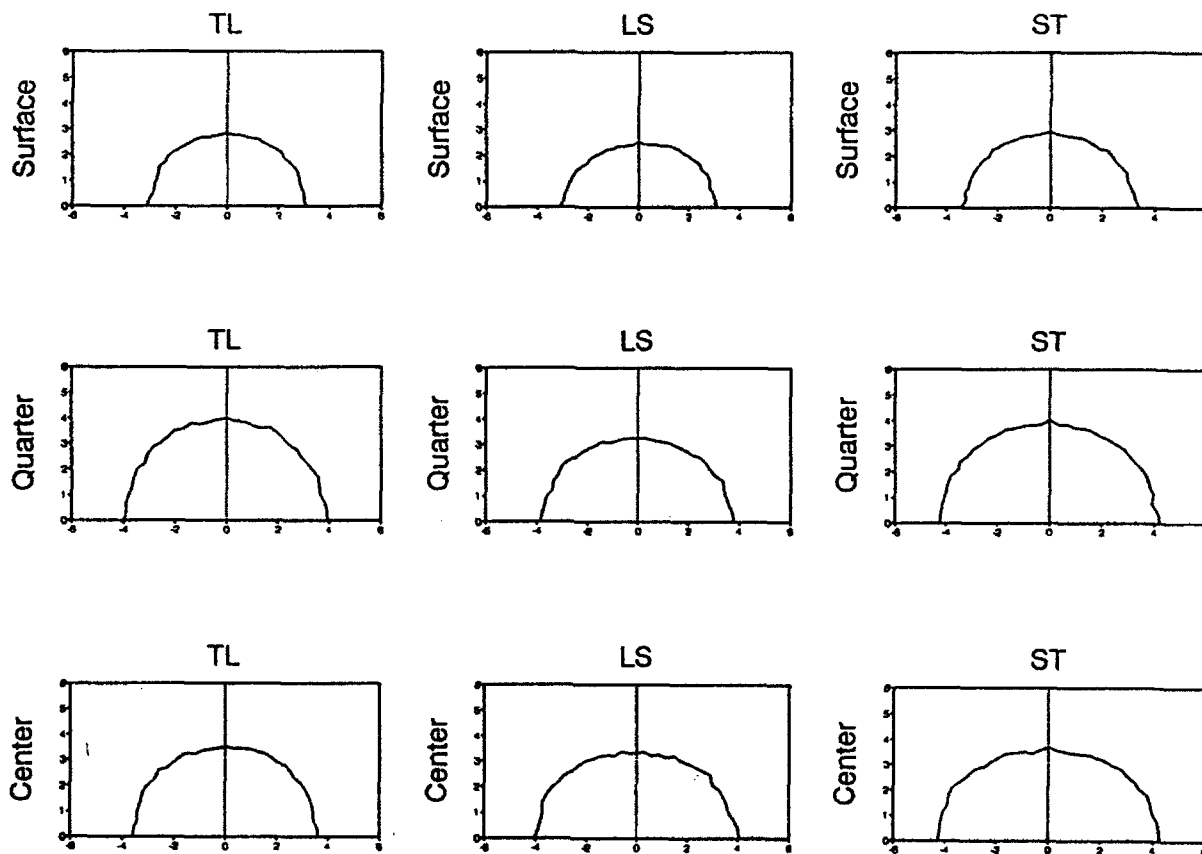
Figure 13. Change of the average dimensions of the pores with direction for different planes and positions within the plate for *new pedigree* 7050-T7451 alloy. The locations are identified by the labels. All units are in micrometers.
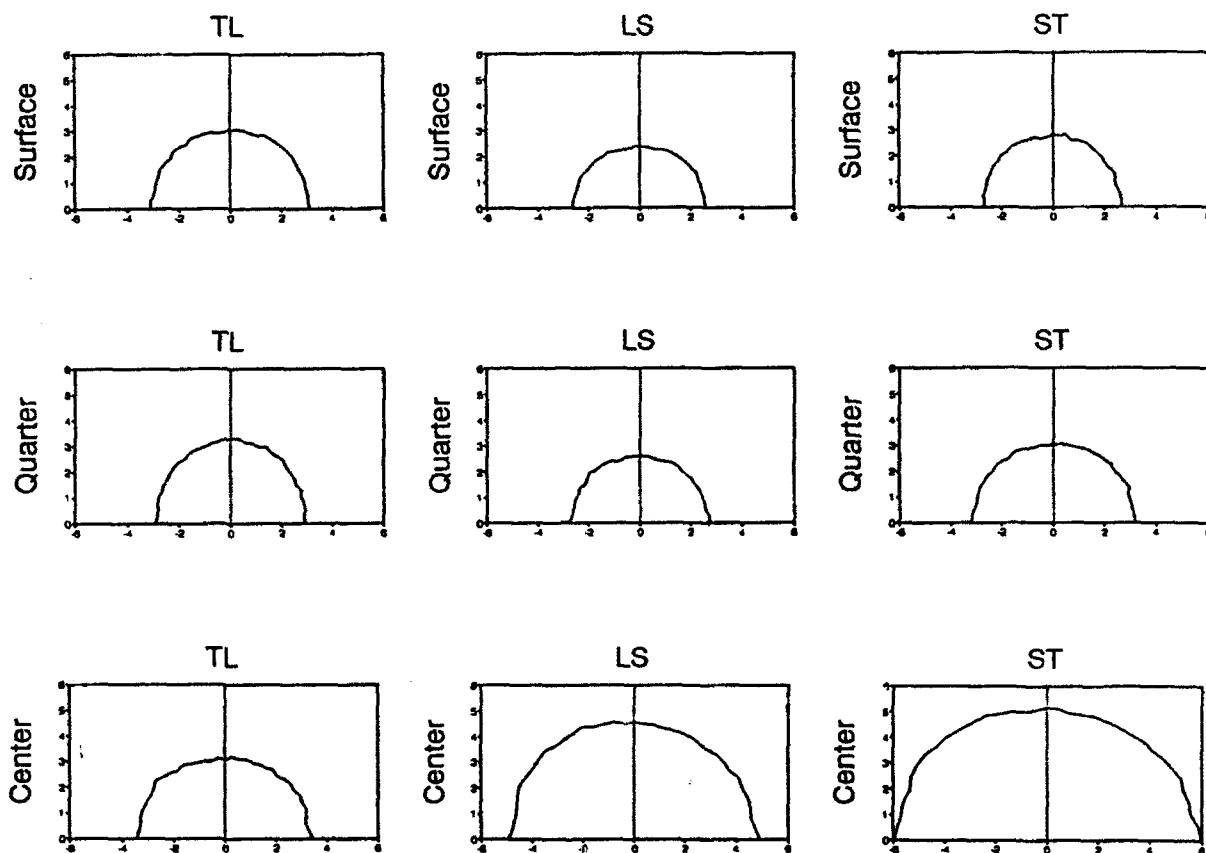
Figure 14. Change of the average dimensions of the pores with direction for different planes and positions within the plate for *old pedigree* 7050-T7451 alloy. The locations are identified by the labels. All units are in micrometers.
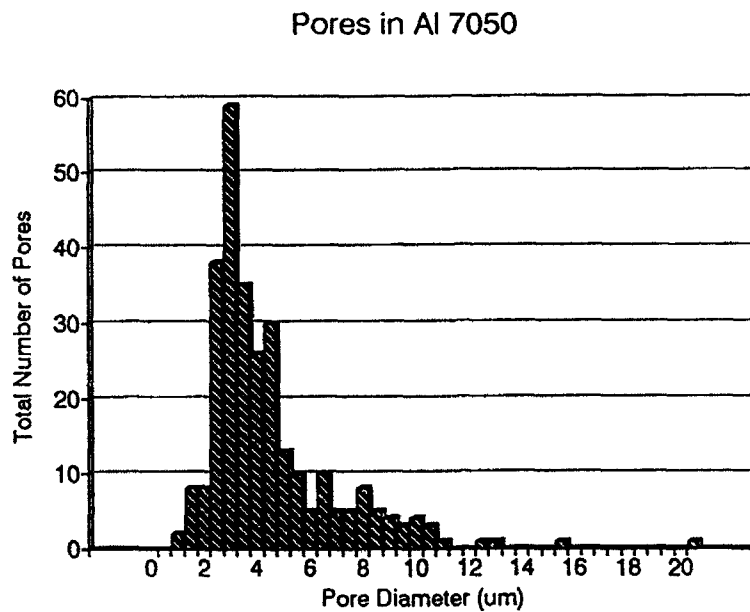
Figure 15. Pore size distributions for the ST-planes, center region of the old pedigree 7050 Al plate.
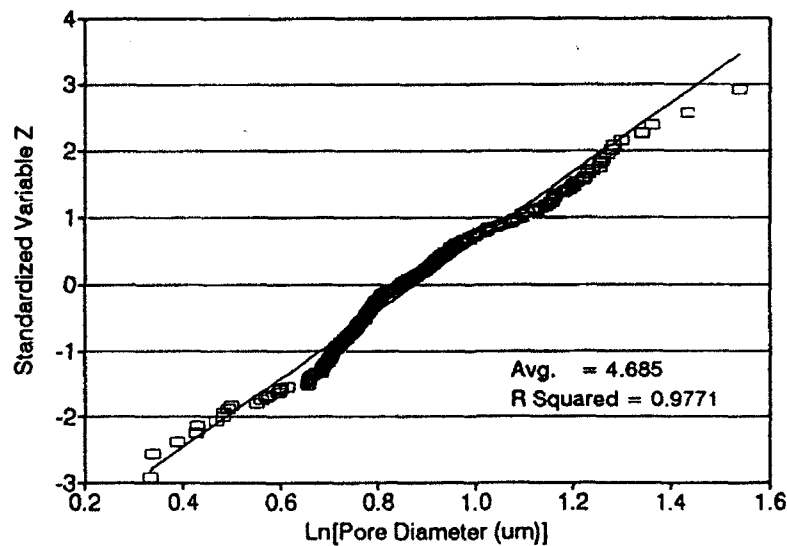
Figure 16. Lognormal probability plots of the pore size distribution for the ST-plane, center region of the old 7050 plate alloy; Solid lines represent the best fit and open squares the experimental data.
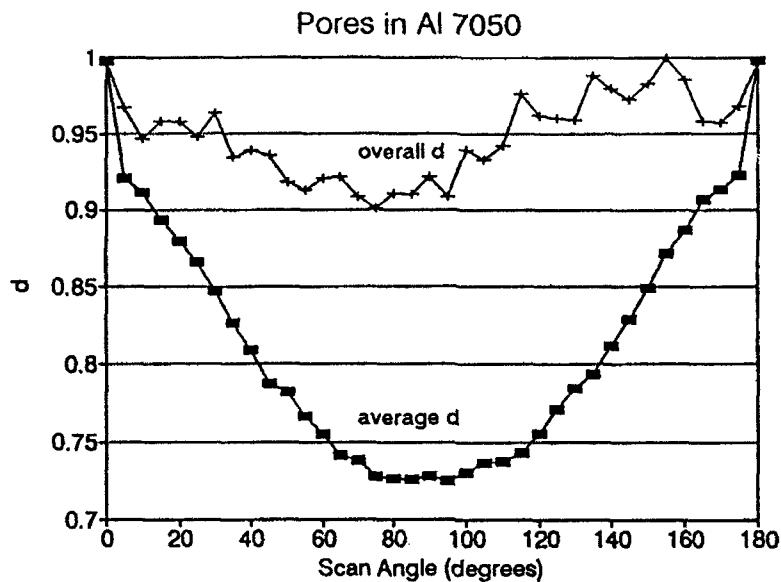
Figure 17. Change of the normalized average intercept length with scan angle for pores from Fig. 11. The overall d is the normalized pore size and average d represents the average shapes (see text)..
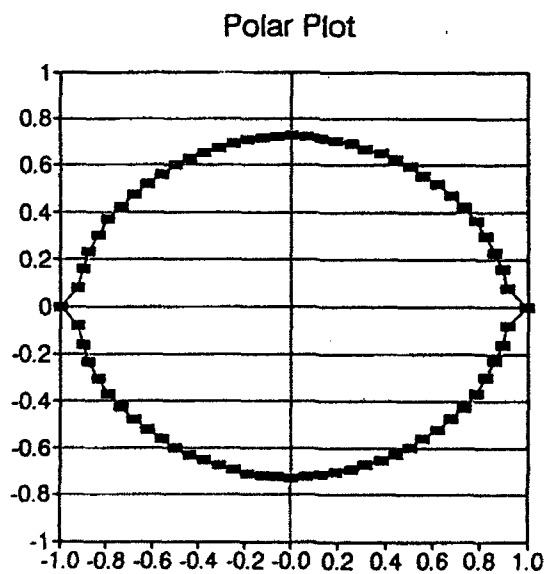
Figure 18. Polar plot of the normalized average d vs. scan angle for pores found on ST-planes, center region of the old 7050-T7451 plate alloy.
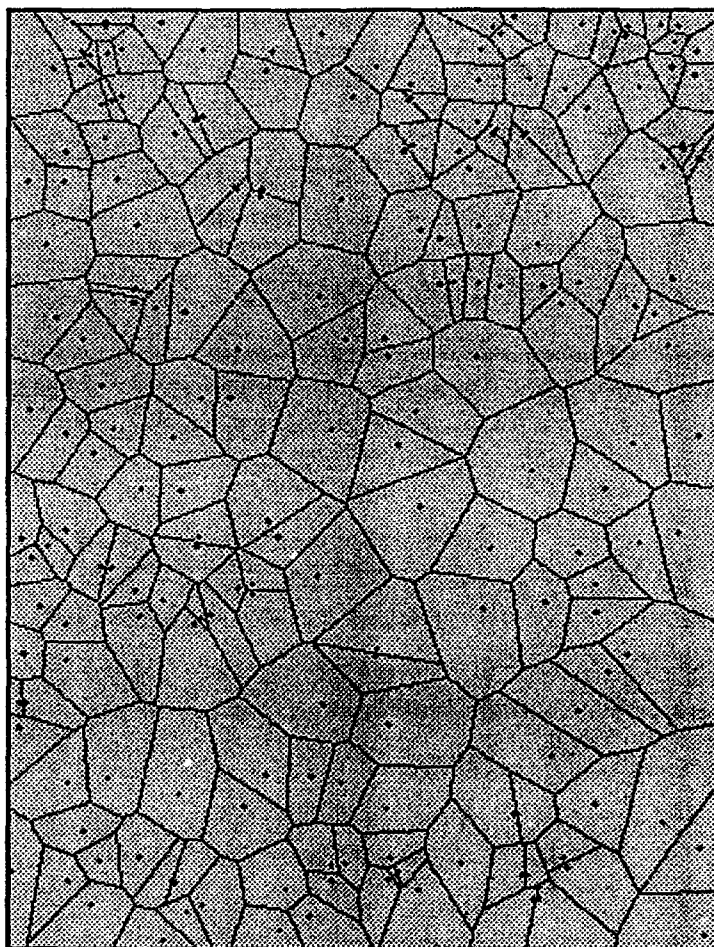
Pores in Al 7050
200 um

Figure 19. Dirichlet tessellation cell construction for pores from ST-planes, plate center, old 7050 alloy. (Points represent pore centers.)
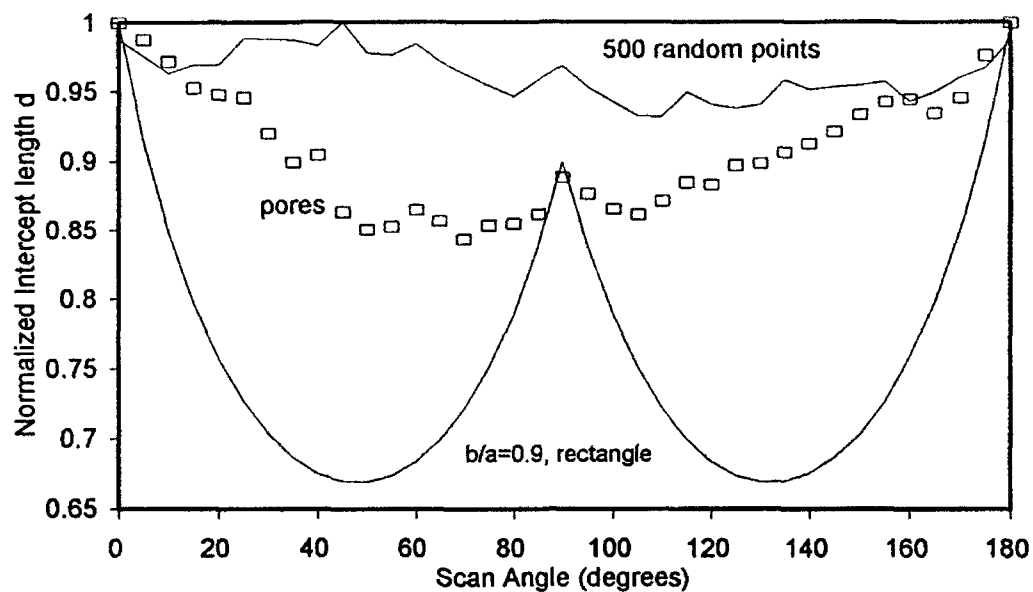
Figure 20. The normalized average intercept lengths vs. scan angles for the tessellation cells shown in Fig. 19. The d-α curves for a rectangular and random arrangements of points are shown for comparison.
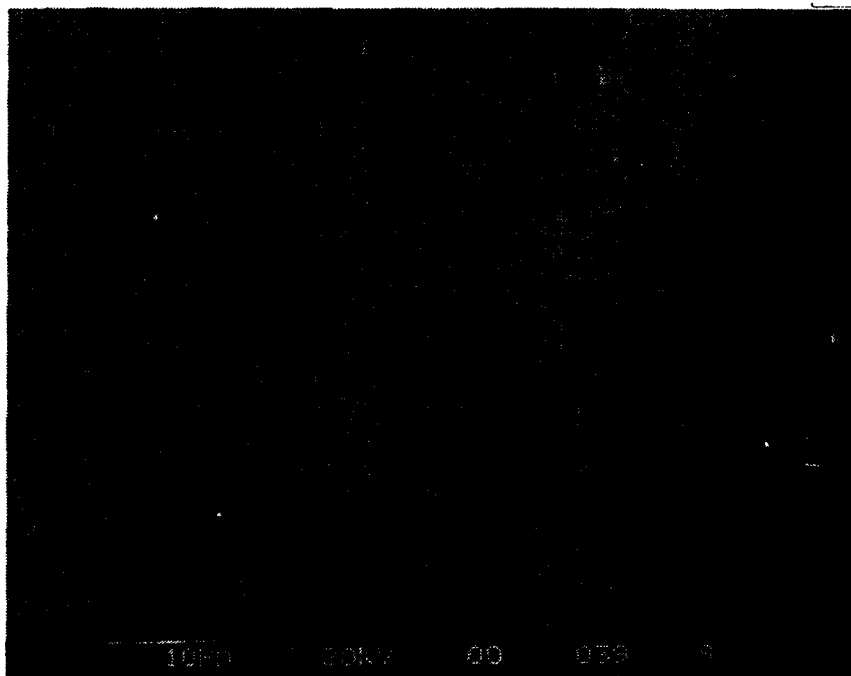
Figure 21. A typical cluster of stringers of the Al_7Cu_2Fe constituents in 7050-T7451 alloy.
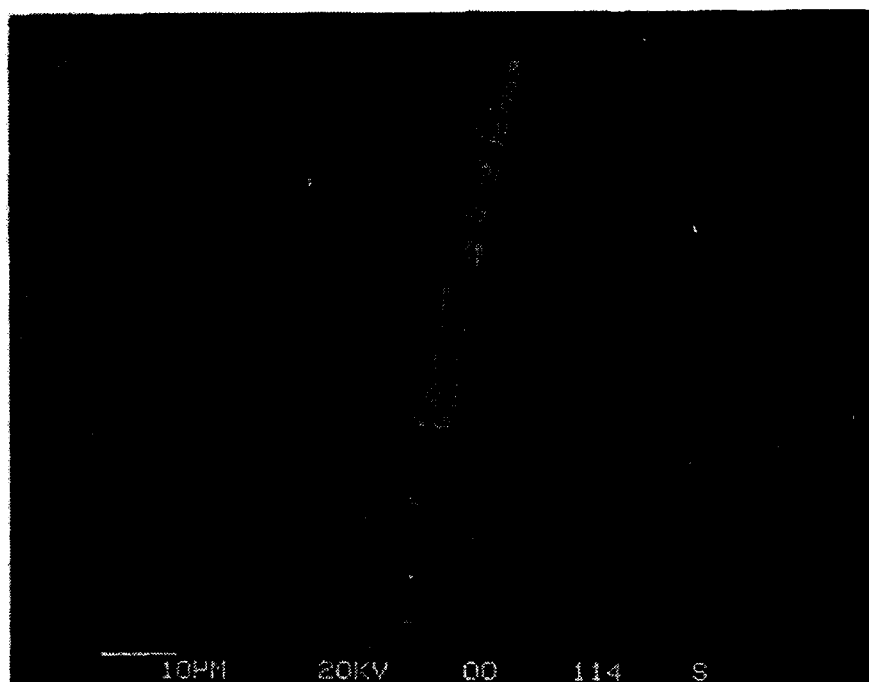
Figure 22. Characteristic stringer of the constituent of the $Al_xMg_xSi_x$ type in the 7050-T7451 alloy.

Constituent Particles In Al 7050
10 um
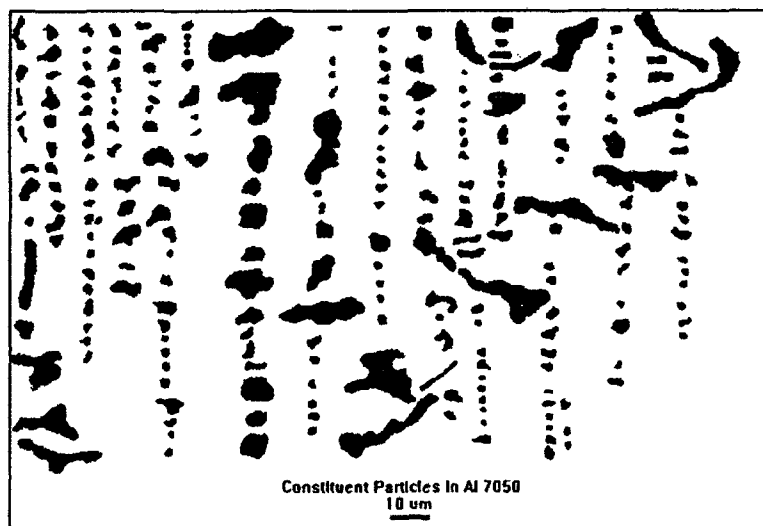
Figure 23. A collection of 236 constituent particles found on the ST-planes, center region of the old pedigree 7050-T7451 plate alloy.
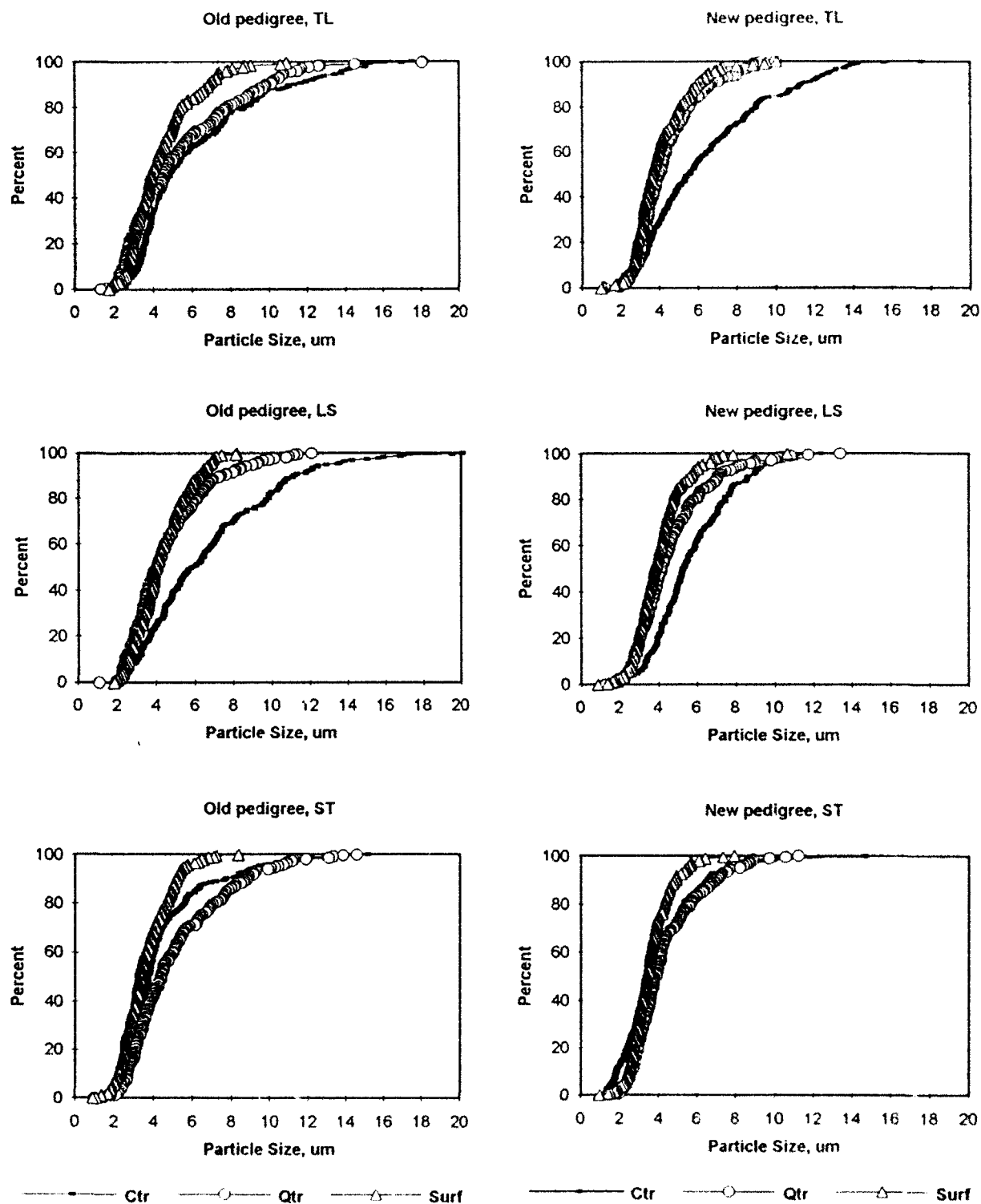
Figure 24. Cumulative particle size distributions in the 7050-T7451 plate alloy.
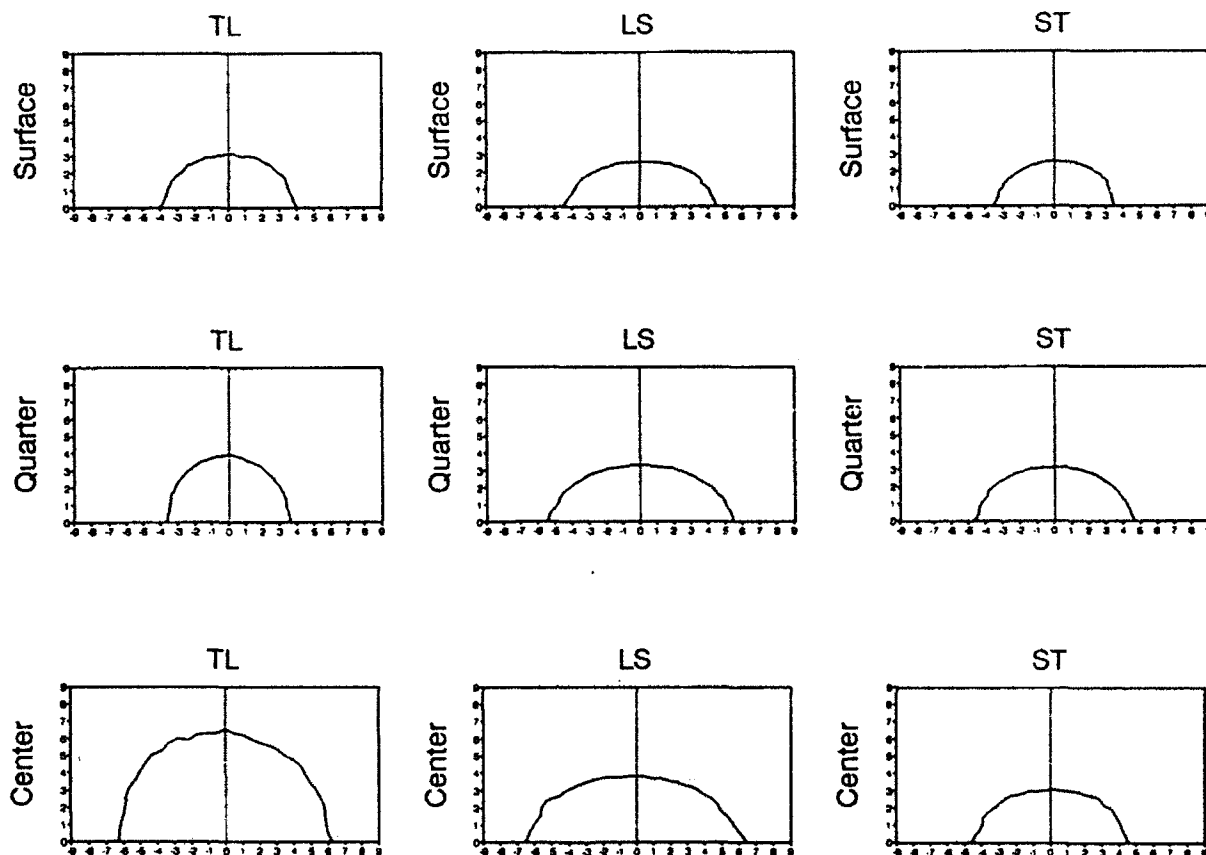
Figure 25. Change of the average dimensions of the constituent particles with direction for different planes and positions within the plate for *new pedigree* 7050-T7451 alloy. The locations are identified by the labels. All units are in micrometers.
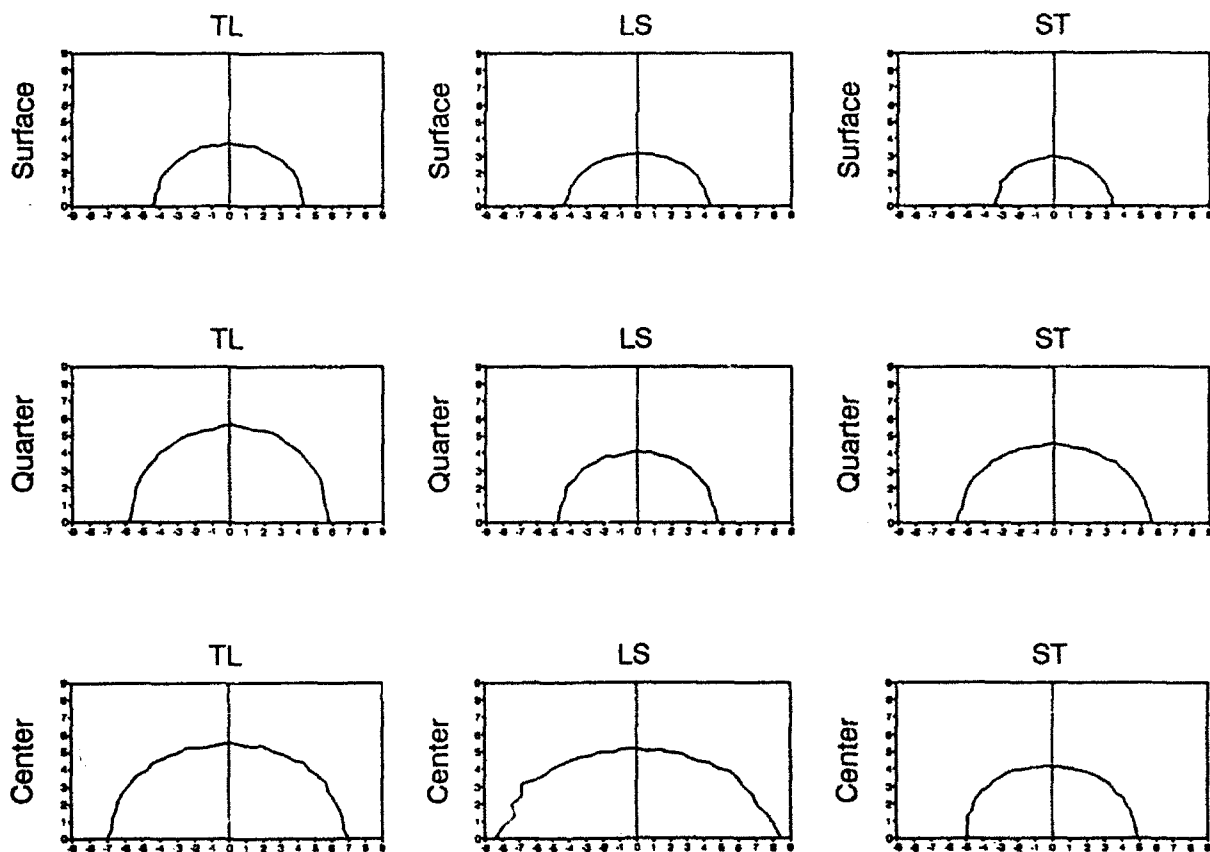
Figure 26. Change of the average dimensions of the constituent particles with direction for different planes and positions within the plate for *old pedigree* 7050-T7451 alloy. The locations are identified by the labels. All units are in micrometers.
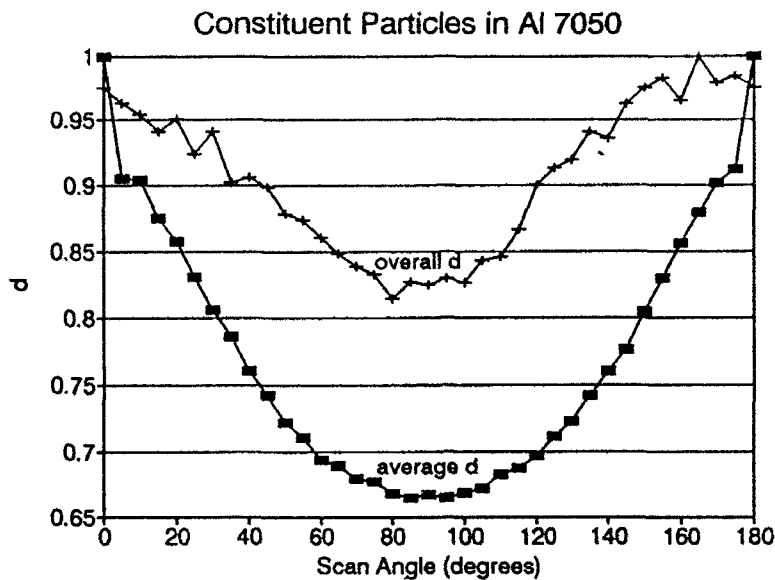
Figure 27. Change of the normalized average intercept length with scan angle for constituent particles from Fig. 23. The overall d is the normalized constituent particle size and average d represents the average shapes (see text).
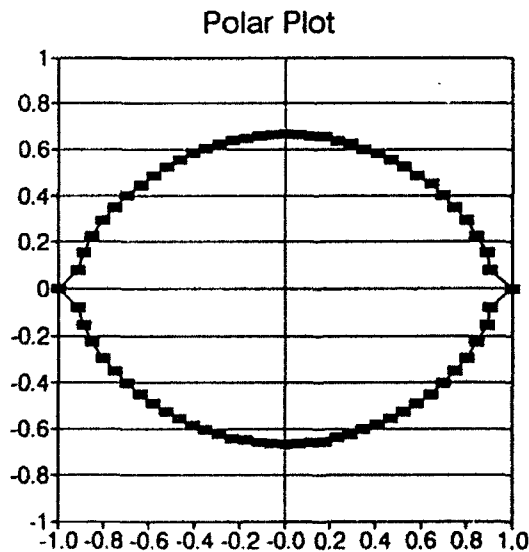
Figure 28. Polar plot of the normalized average d vs. scan angle for constituent particles found on ST-planes, center region of the old 7050-T7451 plate alloy.
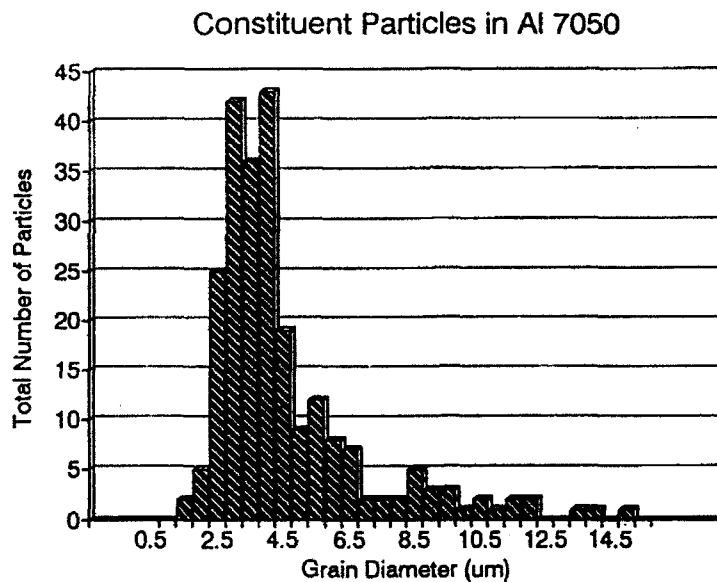
Figure 29. The constituent particle size distribution; ST-planes, center region, old pedigree 7050-T7451 plate alloy.
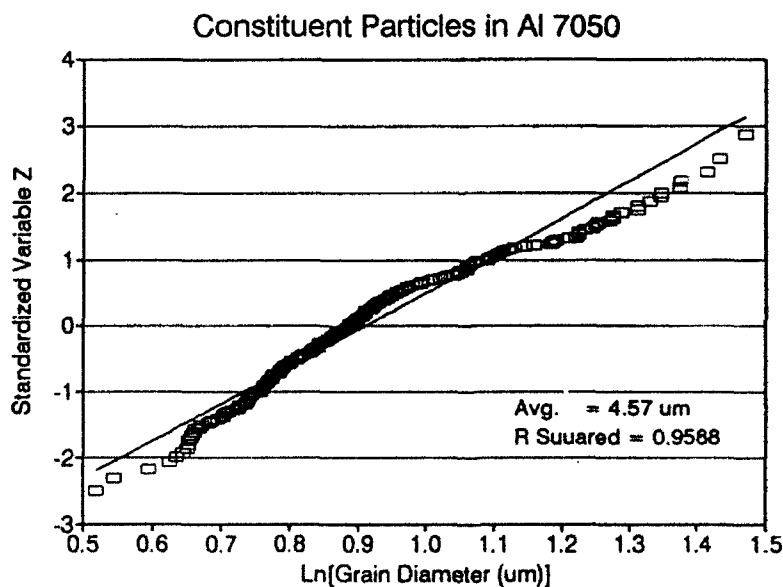
Figure 30. Lognormal probability plots of the constituent particle size distribution for the ST-plane, center region of the old 7050 plate alloy; Solid lines represent the best fit and open squares the experimental data.
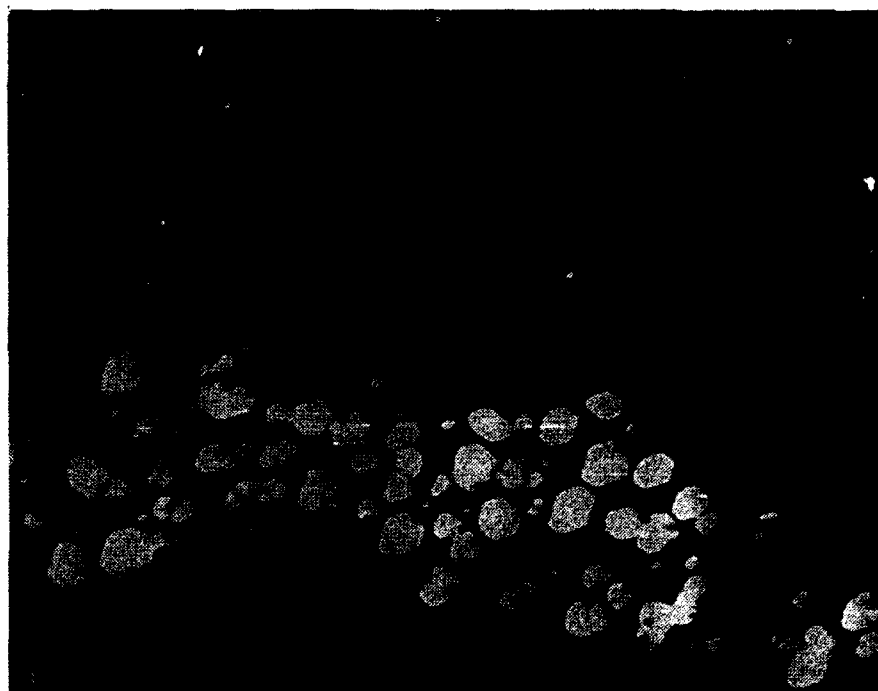
Figure 31. Dark field image of precipitates on boundary inclined to foil surface.
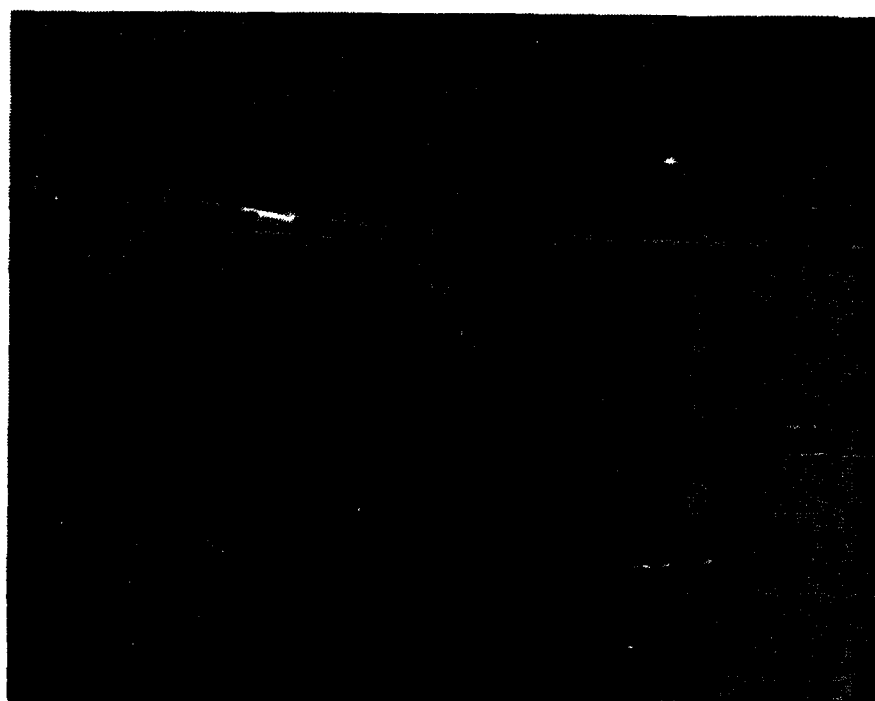
Figure 32. Grain boundary containing a multiple of precipitate variants.

GRAIN BOUNDARY
PRECIPITATES
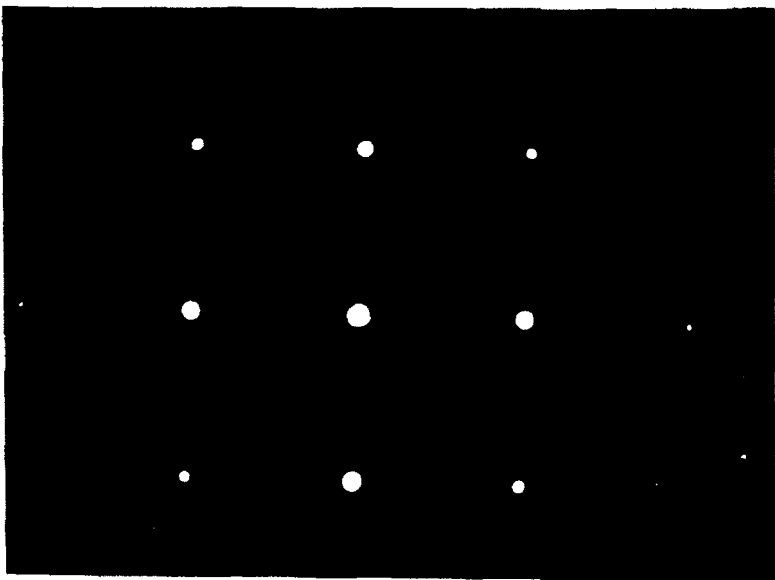
DIFFRACTION PATTERN FOR
ONE GRAIN (KICKUCHI
PATTEN CENTERED)

DIFFRACTION PATTERN FOR
OTHER GRAIN (KICKUCHI
PATTERN SHIFTED)

Figure 33. Micrographs demonstrating large precipitates on low angle grain boundary.
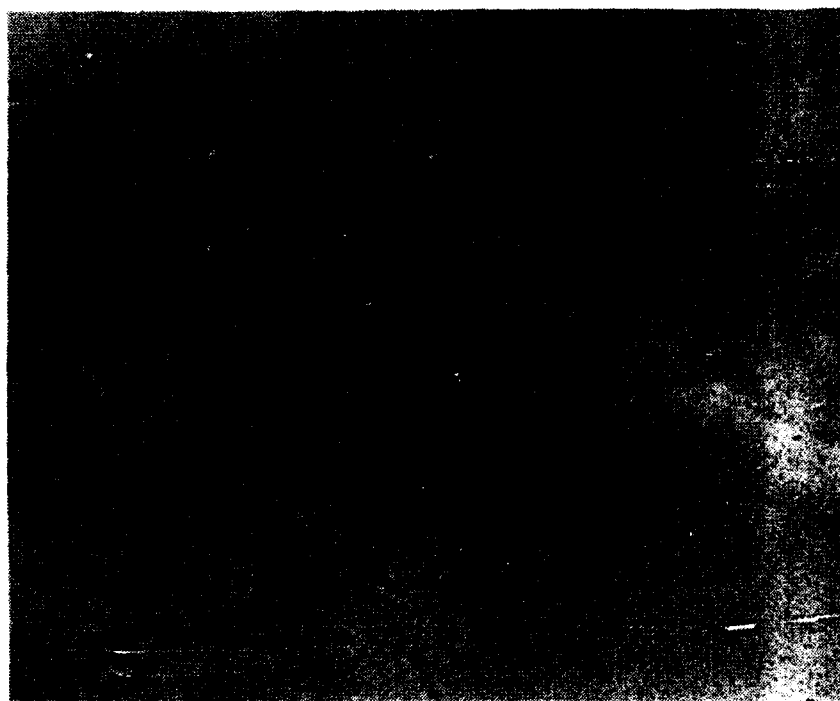
Figure 34. Low magnification photograph showing several grain boundaries containing precipitates.
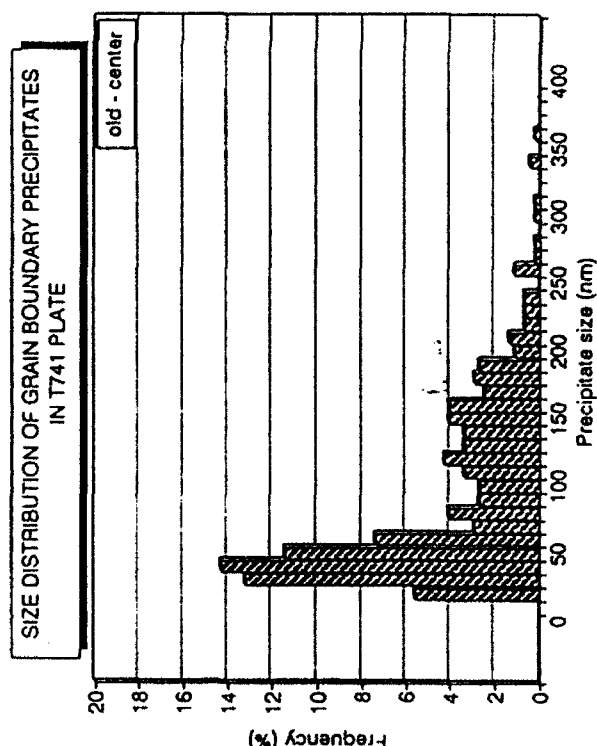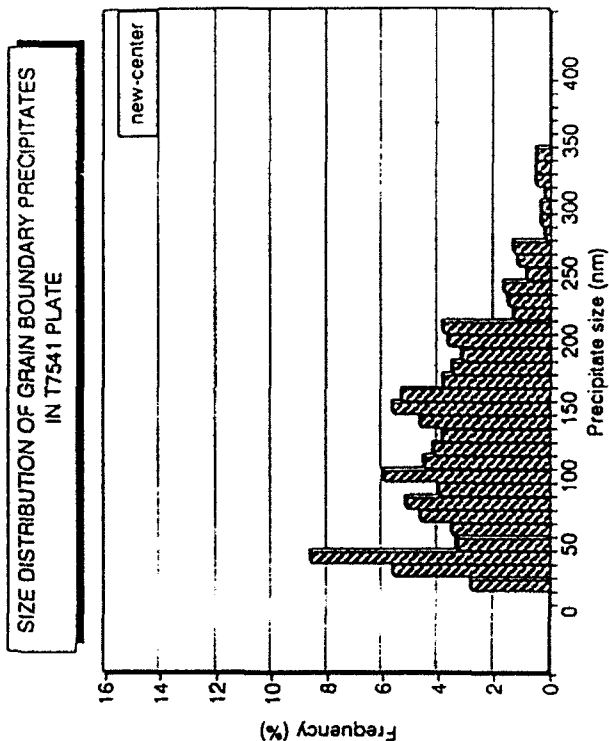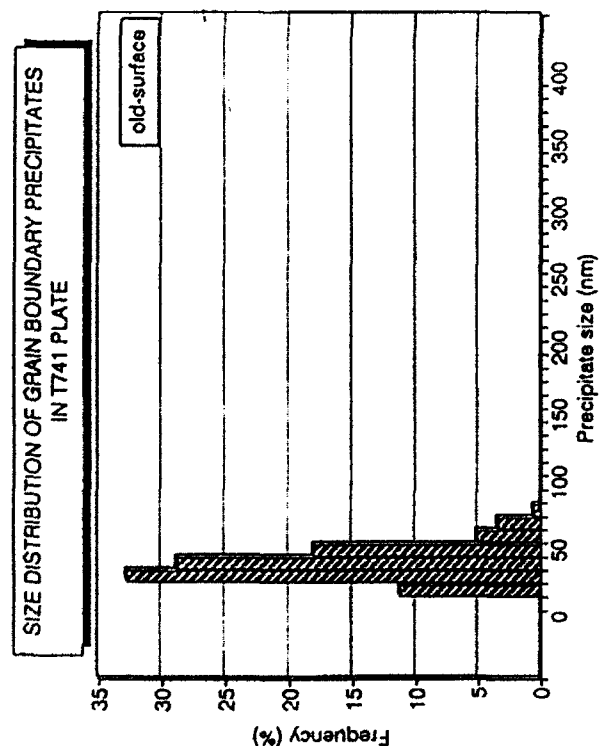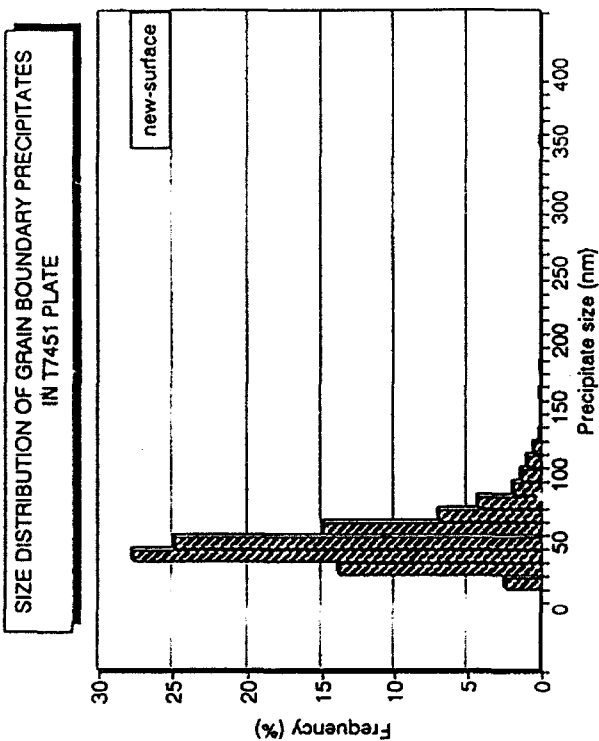
Figure 35. Size distribution of grain boundary precipitates for surface and center sections of old and new 7050 alloy.
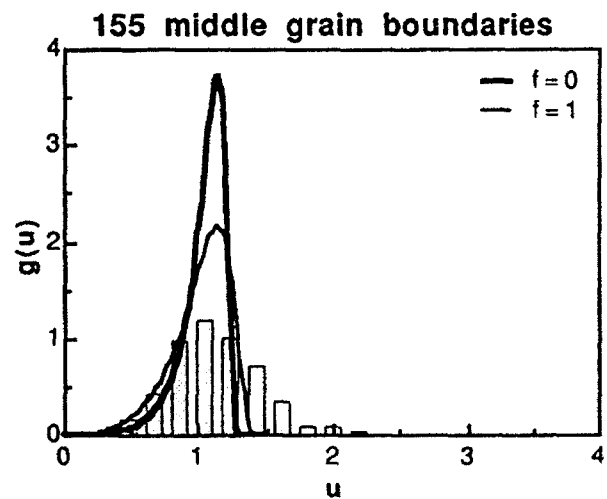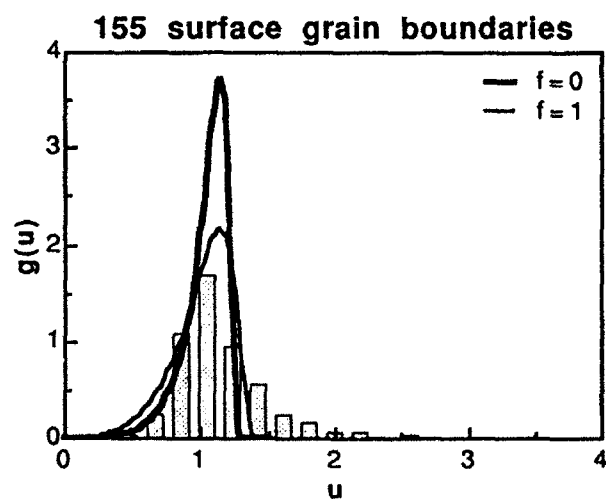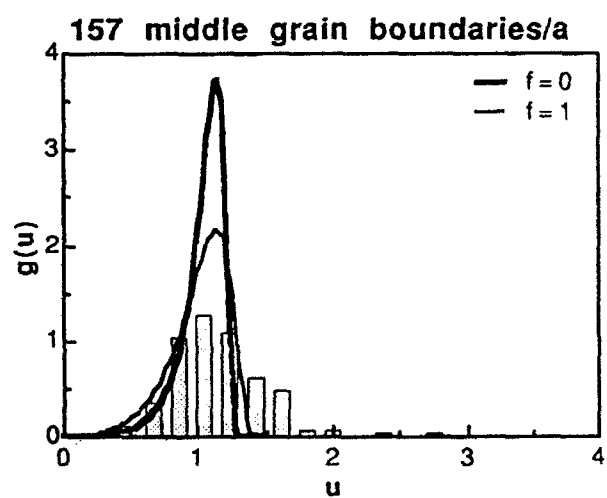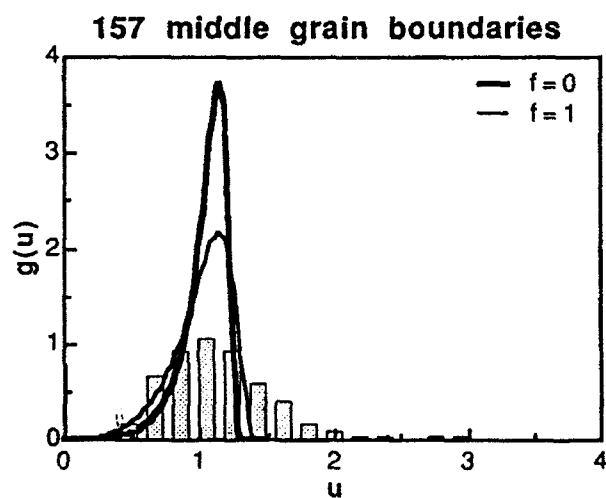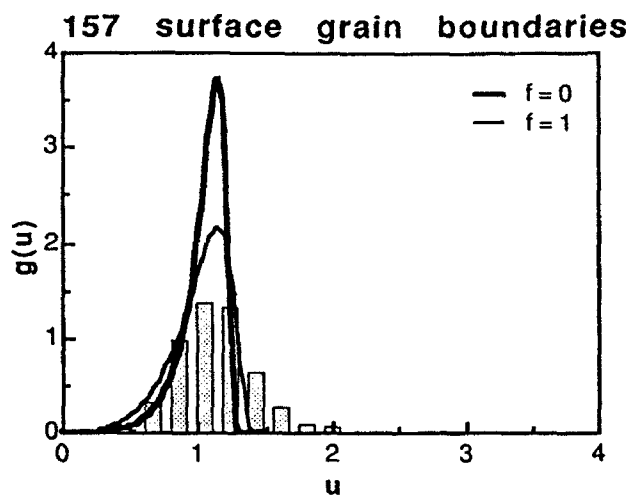
Figure 36. Normalized size distributions of grain boundary precipitates for surface and middle sections of old (155) and new (157) 7050-T7451 alloys.
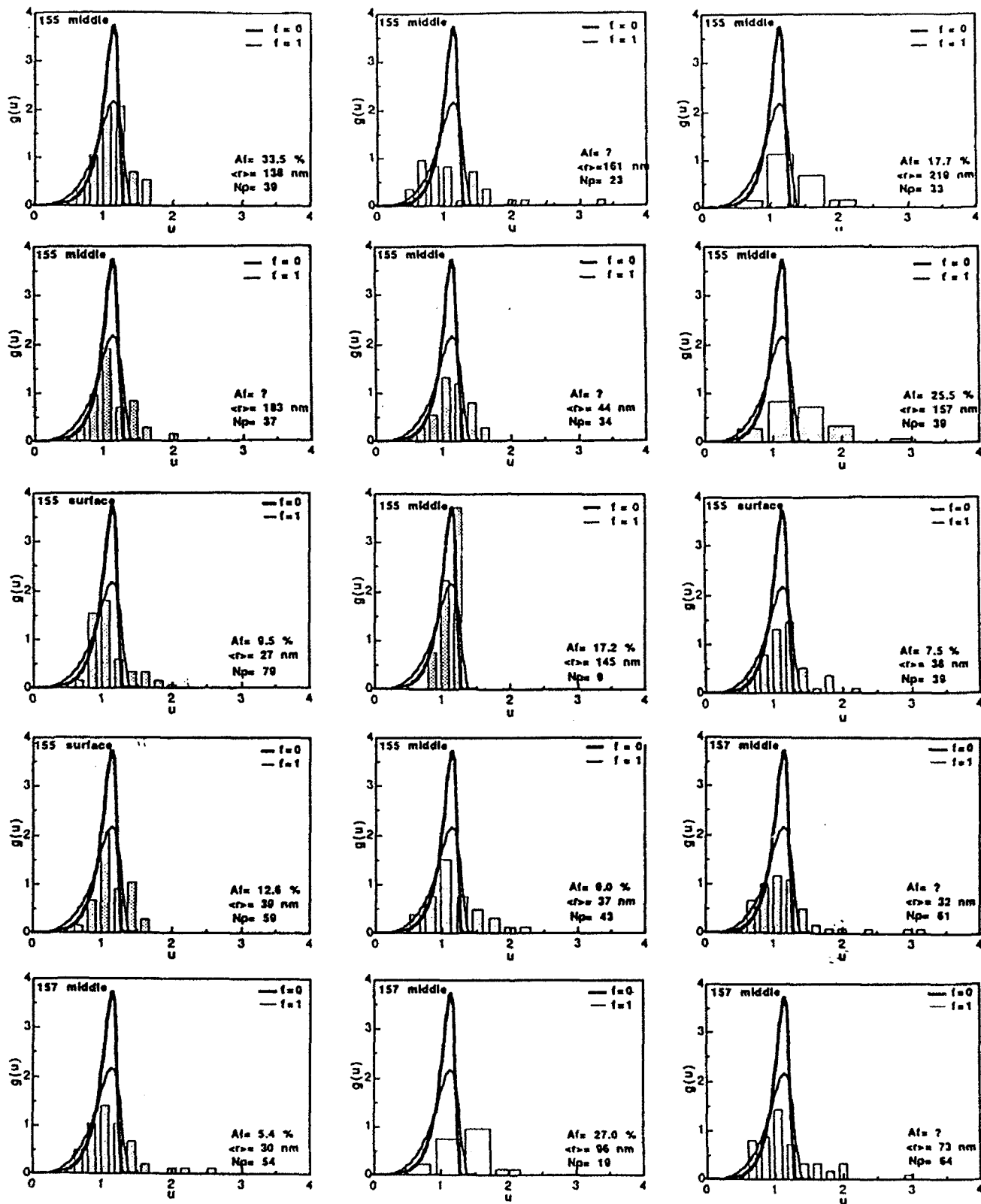
Figure 37. Normalized size distributions of grain boundary precipitates for individual boundaries.
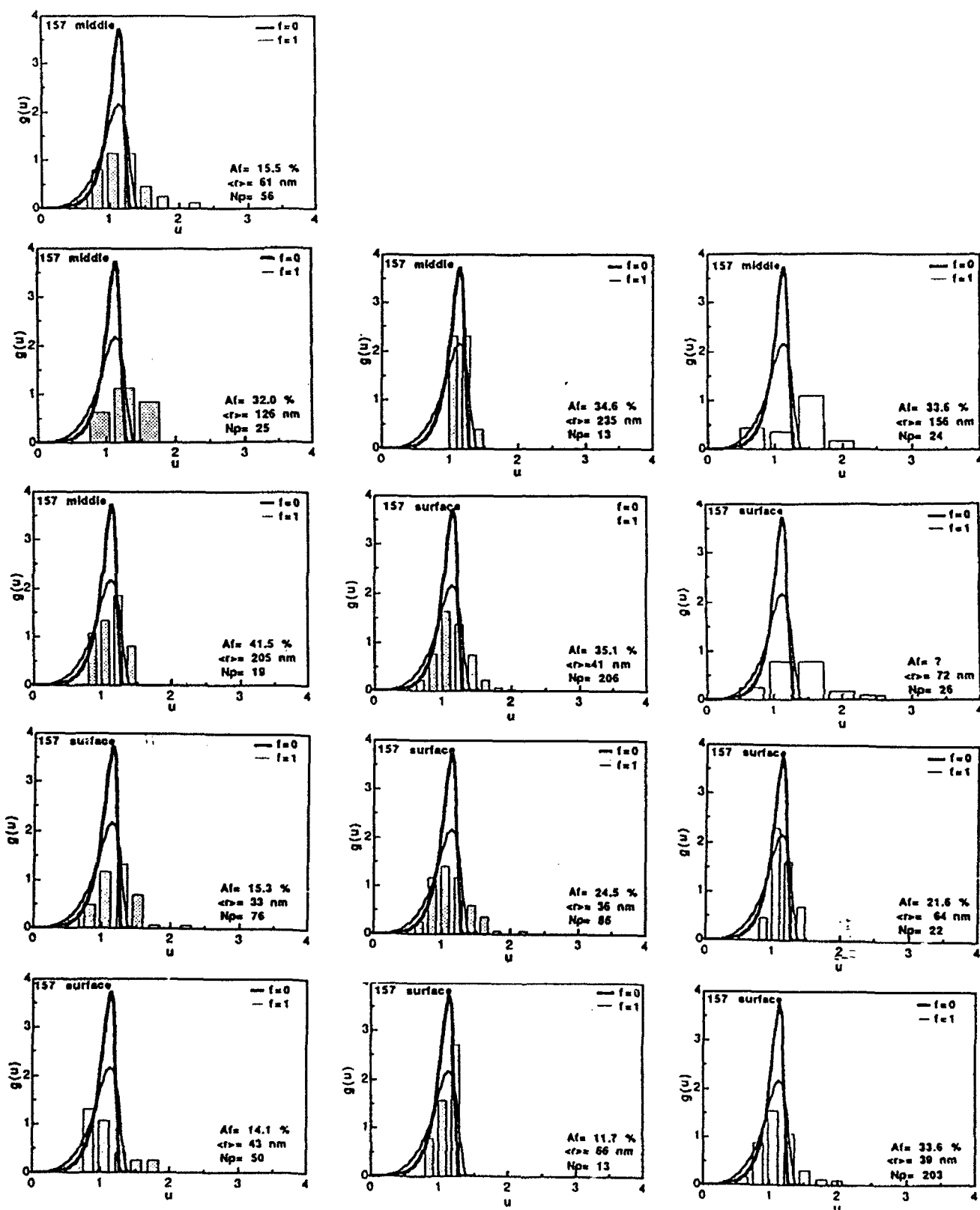
Figure 37. continued.
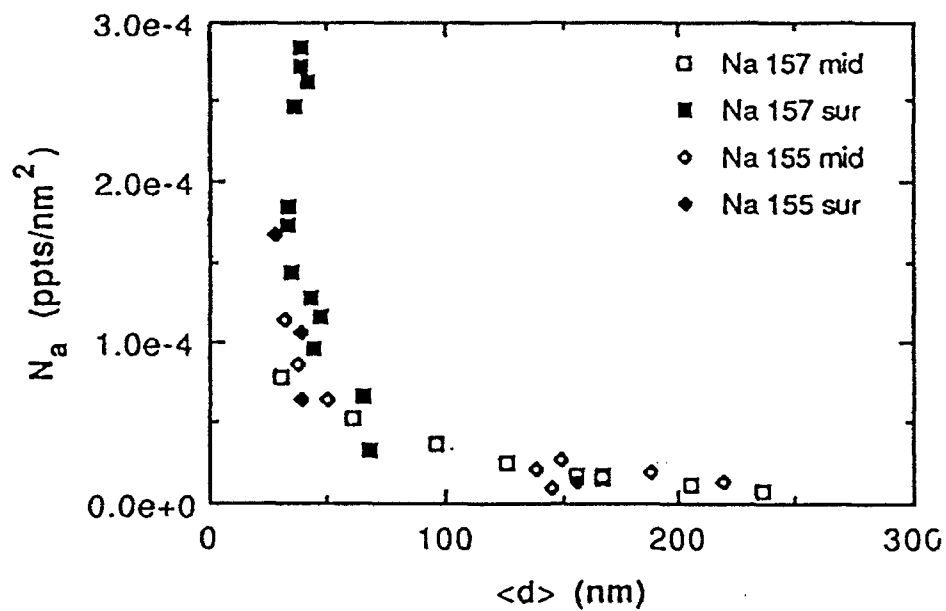
Figure 38. Number of grain boundary precipitates per unit area versus the average size of precipitates.

Figure 39. A pore found on the fracture surface of an open hole fatigue specimen of new 7050 alloy. The pore is located at the hole and acted as the origin of the fatigue crack.
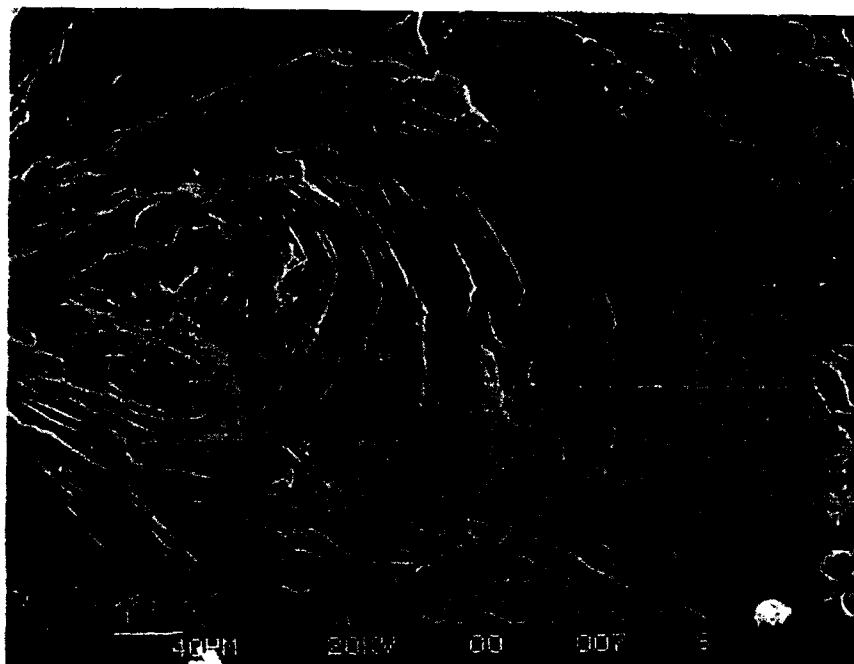
Figure 40. Fracture surface of the open hole fatigue specimen of new 7050 alloy with several cracks and cleavage planes.
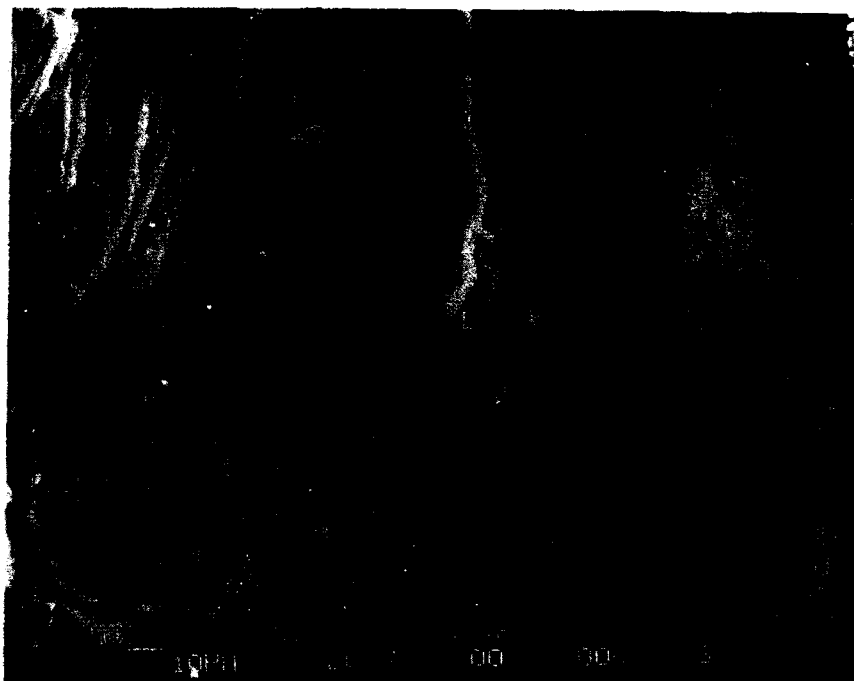
Figure 41. Grain structure from Fig. 40 at higher magnification.

Figure 42. Micrograph showing fatigue striations in the central region of the fracture surface.

Figure 43. Fatigue striations. as in Fig. 42, at higher magnification.

(a) Section angle = 120

(b) section angle = 60

(c) section angle = 0
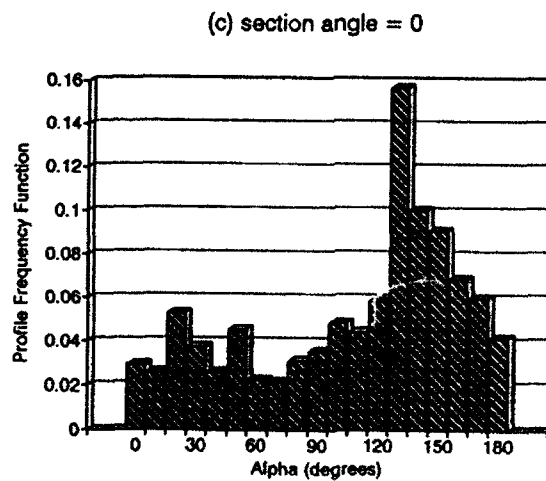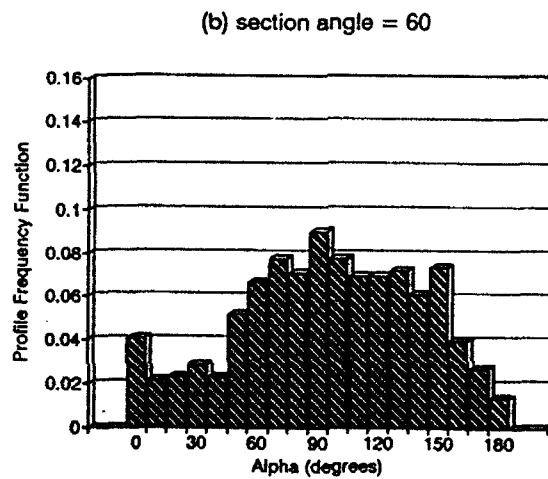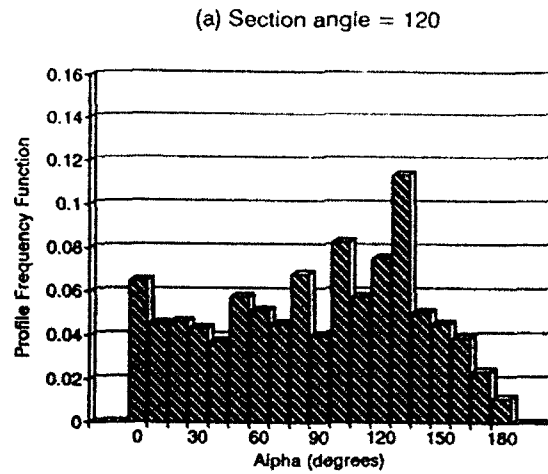
Figure 44. Profile orientation distribution functions for the fracture surface of the open hole fatigue sample of the new pedigree 7050 alloy. Sections at (a) 120 ° (b) 60 ° and (c) 0 ° to the specimen surface. The location of the fracture surface is about 10 mm away from the open hole.

(a) section angle = 120

(b) section angle = 60

(c) section angle = 0
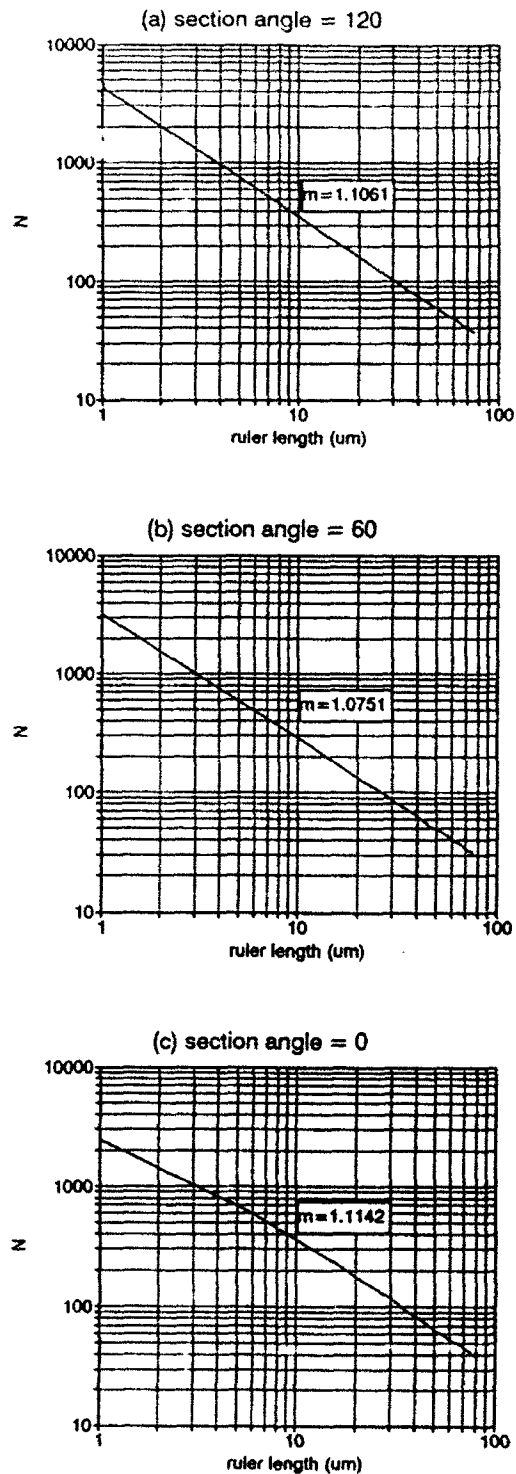
Figure 45. Plots of the number of steps, *N*, vs. the ruler length for the fatigue fracture surface of a new pedigree 7050 alloy specimen for sections at (a) 120 ° (b) 60 ° and (c) 0 °. The measurement is made near the edge of the open hole fatigue specimen   *m*'s are the fractal dimensions.

Fatigued Fracture Surface of Al 7050

(a)

Fatigued Fracture Surface of Al 7050

(b)
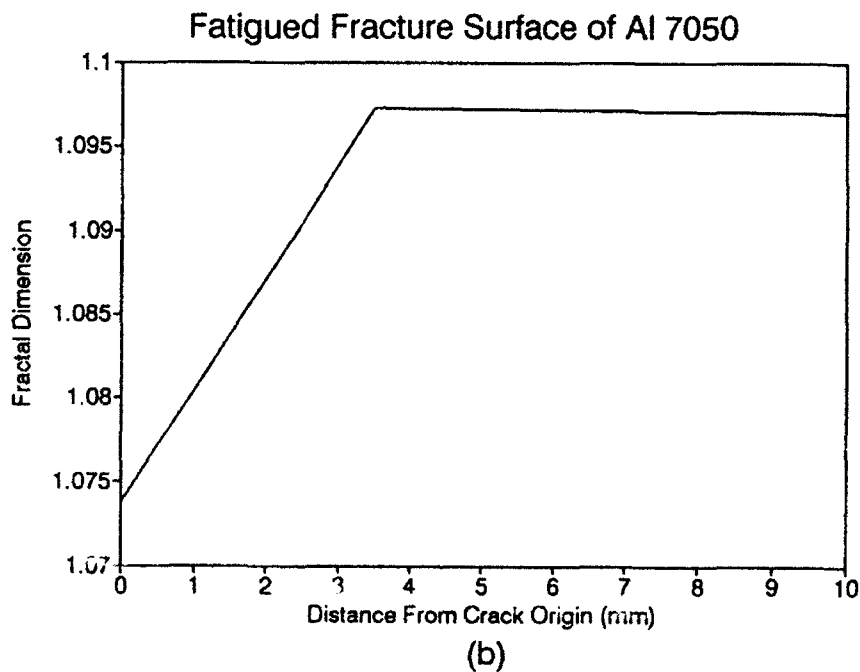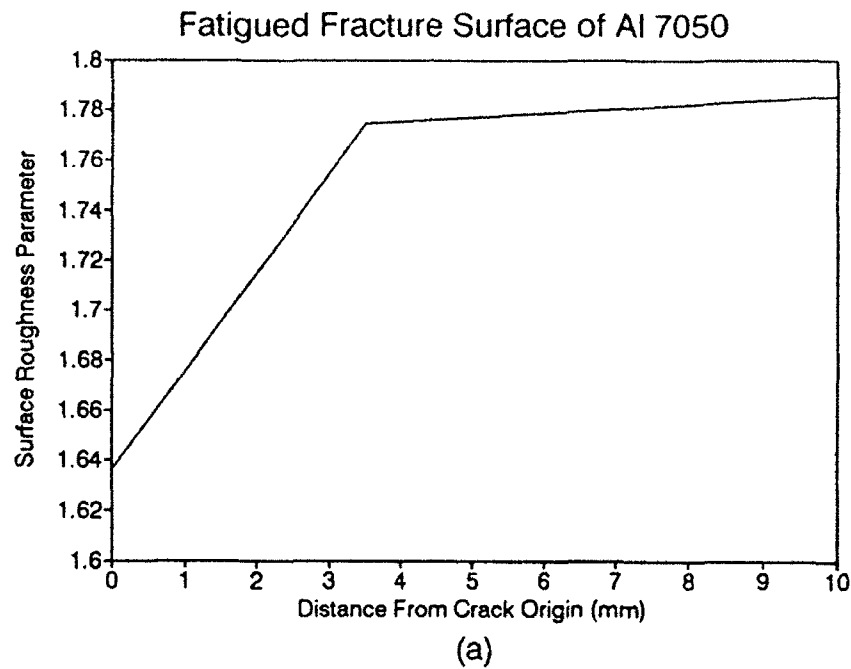
Figure 46. Change of (a) roughness parameter and (b) the fractal dimension with distance from the crack origin for the fatigue fracture surface of the new 7050 plate alloy.
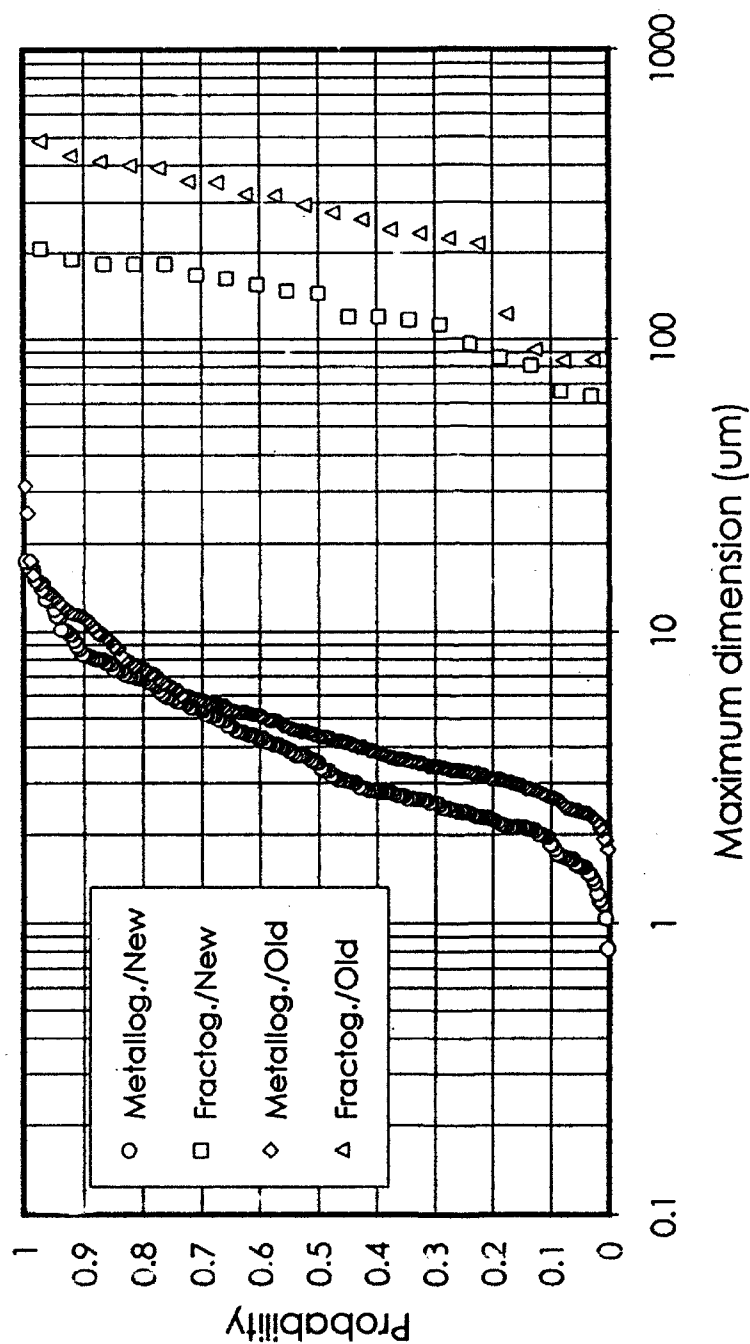
Figure 47. Comparison of the distributions of the maximum pore dimensions measured on metallographic sections with the actual fatigue crack initiating pore sizes obtained from fractographic analysis of the smooth fatigue samples.
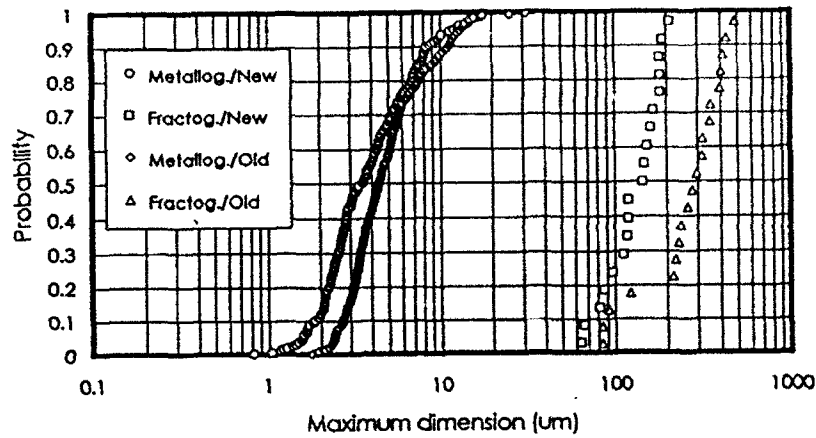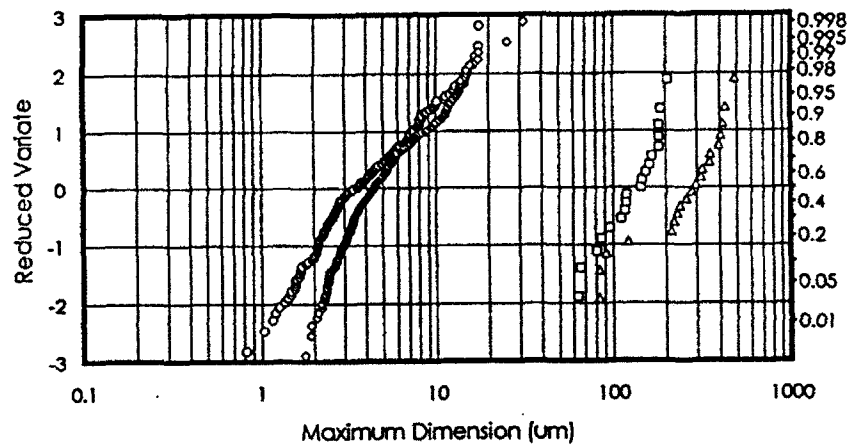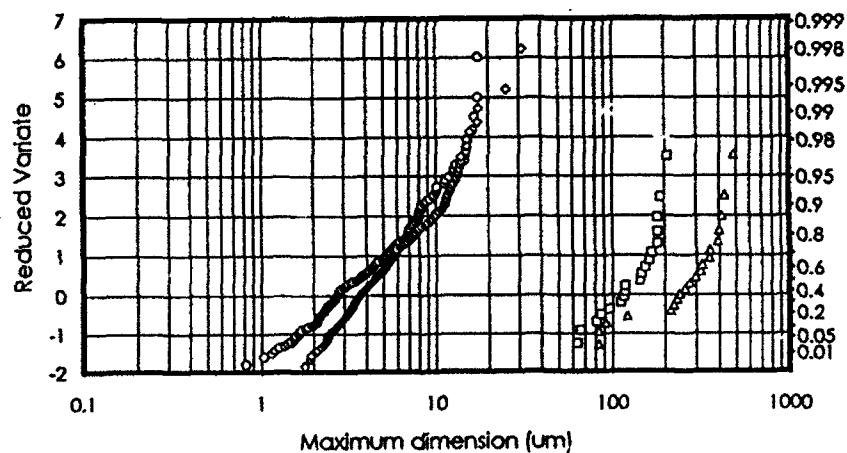
Figure 48. Comparison of the metallographic and fractographic pore size data for the old and new pedigree 7050-T7451 alloys on (a) linear, (b) lognormal and (c) Gumbel probability papers.
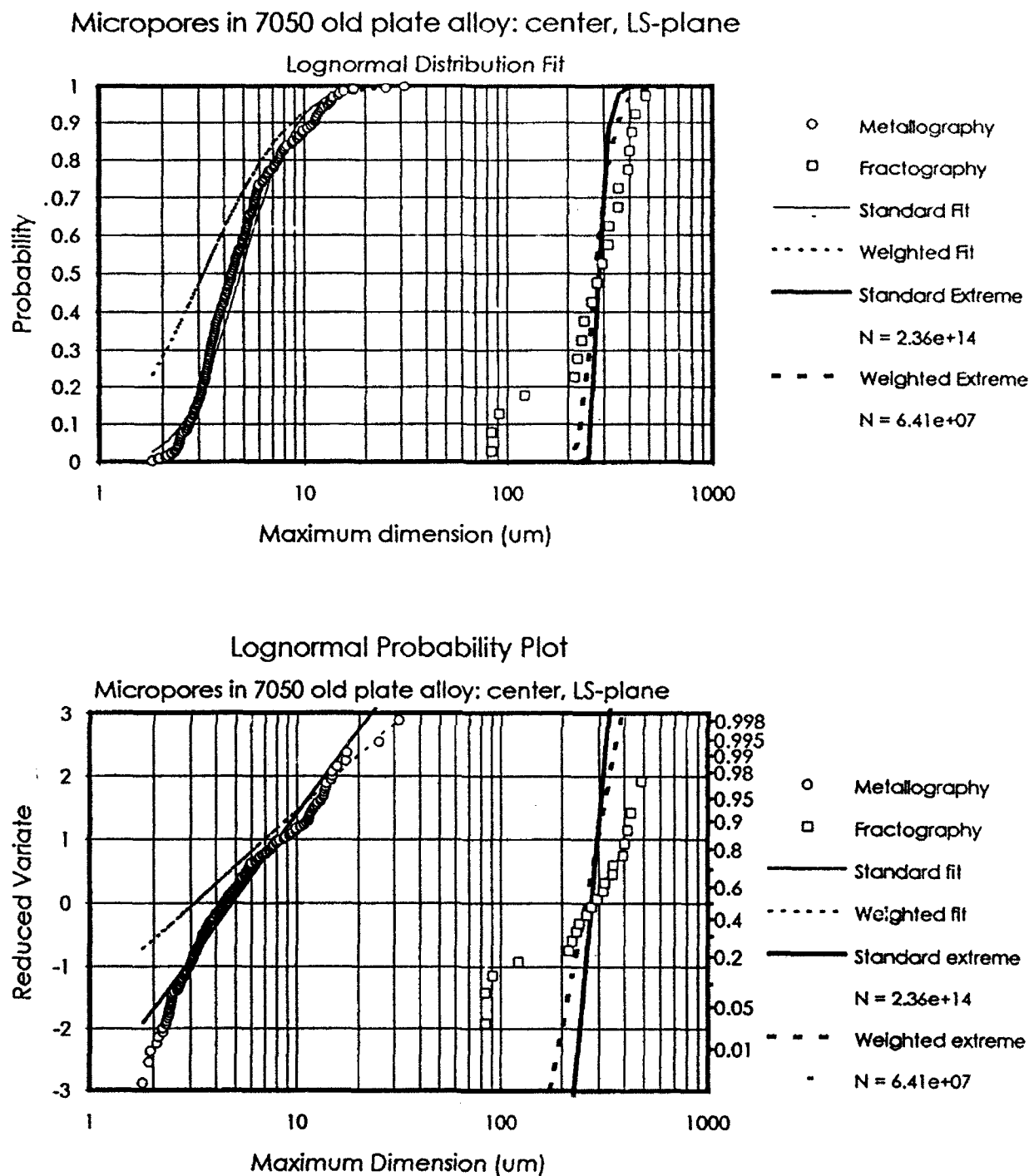
Micropores in 7050 old plate alloy: center, LS-plane

Lognormal Distribution Fit

o	Metallography
□	Fractography
—— · —	Standard Fit
· · · · · ·	Weighted Fit
——	Standard Extreme
	N = 2.36e+14
– – –	Weighted Extreme
	N = 6.41e+07

Lognormal Probability Plot

Micropores in 7050 old plate alloy: center, LS-plane

o	Metallography
□	Fractography
——	Standard fit
· · · · · ·	Weighted fit
——	Standard extreme
	N = 2.36e+14
– – –	Weighted extreme
-	N = 6.41e+07

Figure 49. Linear and lognormal probability plots for metallographic and fractographic pore size data for old pedigree 7050 alloy. Metallographic data have been fitted with lognormal parent distribution using standard and weighted fit. Resulting extreme value distributions and their optimum sample sizes, N, are shown as standard and weighted extreme distribution lines.
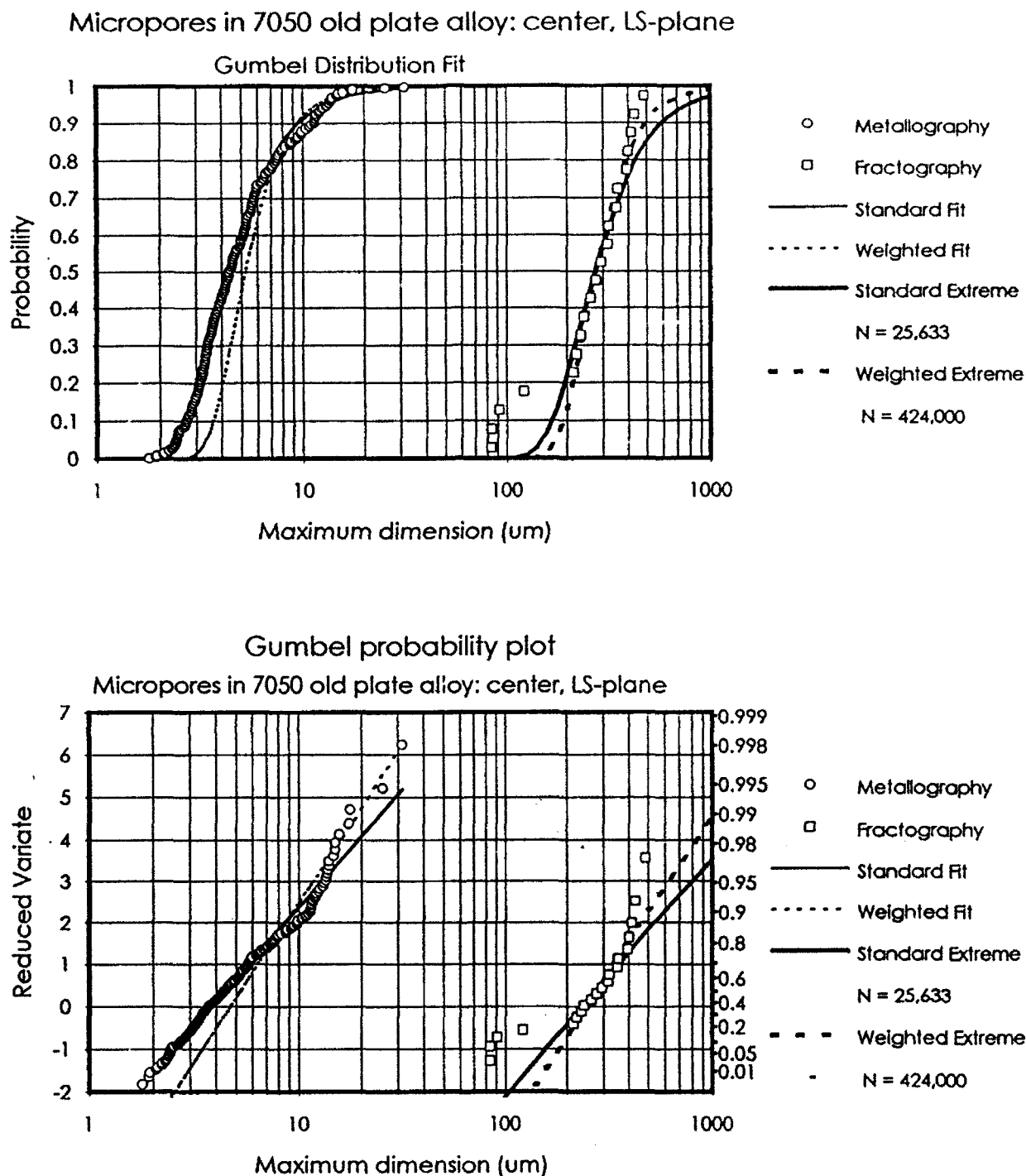
Micropores in 7050 new plate alloy: center, LS-plane

Lognormal Distribution Fit

Lognormal Probability Plot

Micropores in 7050 new plate alloy: center, LS-plane
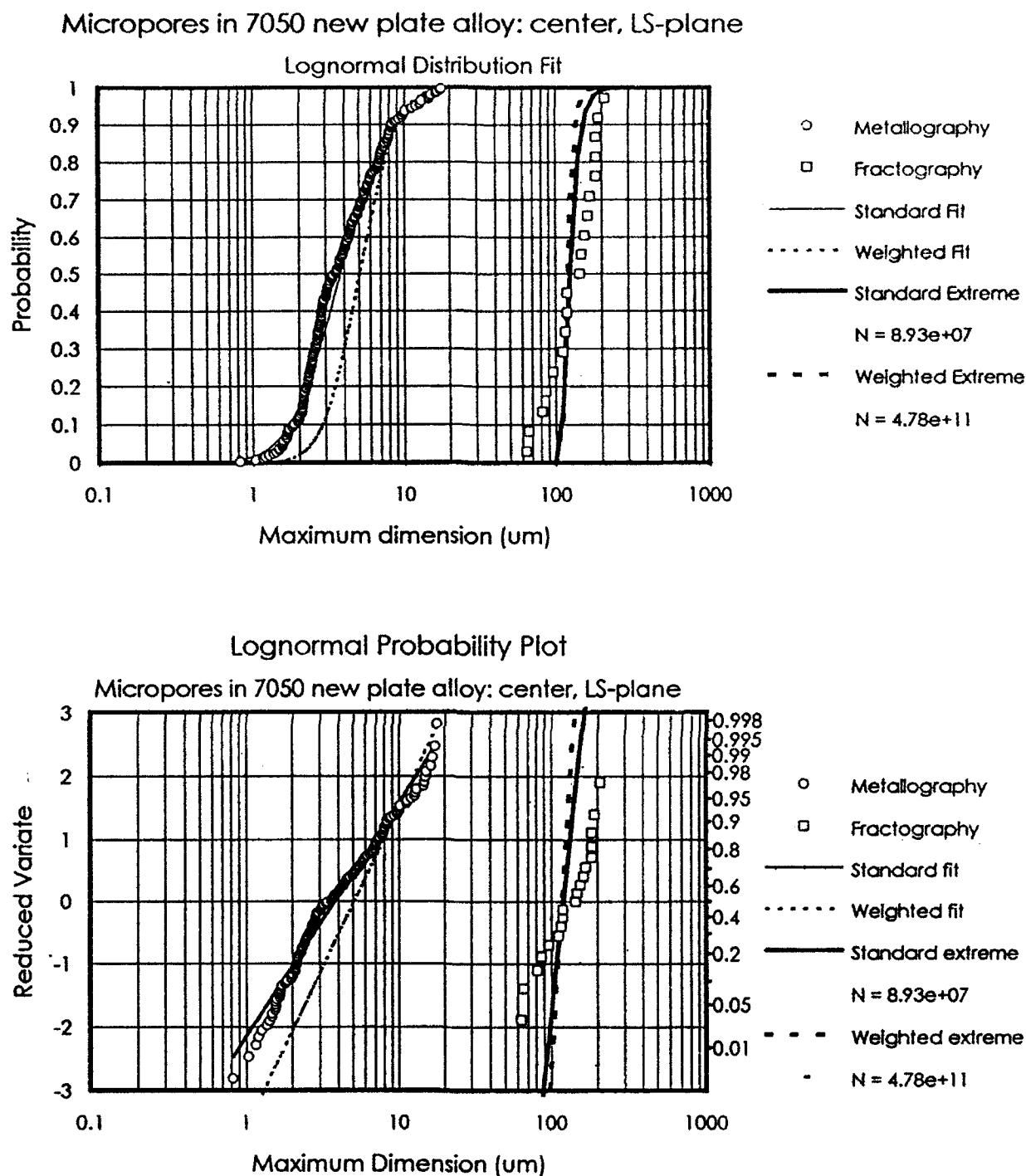
Figure 50. Linear and lognormal probability plots for metallographic and fractographic pore size data for new pedigree 7050 alloy. Metallographic data have been fitted with lognormal parent distribution using standard and weighted fit. Resulting extreme value distributions and their optimum sample sizes, N, are shown as standard and weighted extreme distribution lines.

Micropores in 7050 old plate alloy: center, LS-plane

Gumbel Distribution Fit

Gumbel probability plot

Micropores in 7050 old plate alloy: center, LS-plane

Figure 51. Linear and Gumbel probability plots for metallographic and fractographic pore size data for old pedigree 7050 alloy. Metallographic data have been fitted with Gumbel parent distribution using standard and weighted fit. Resulting extreme value distributions and their optimum sample sizes, N, are shown as standard and weighted extreme distribution lines.
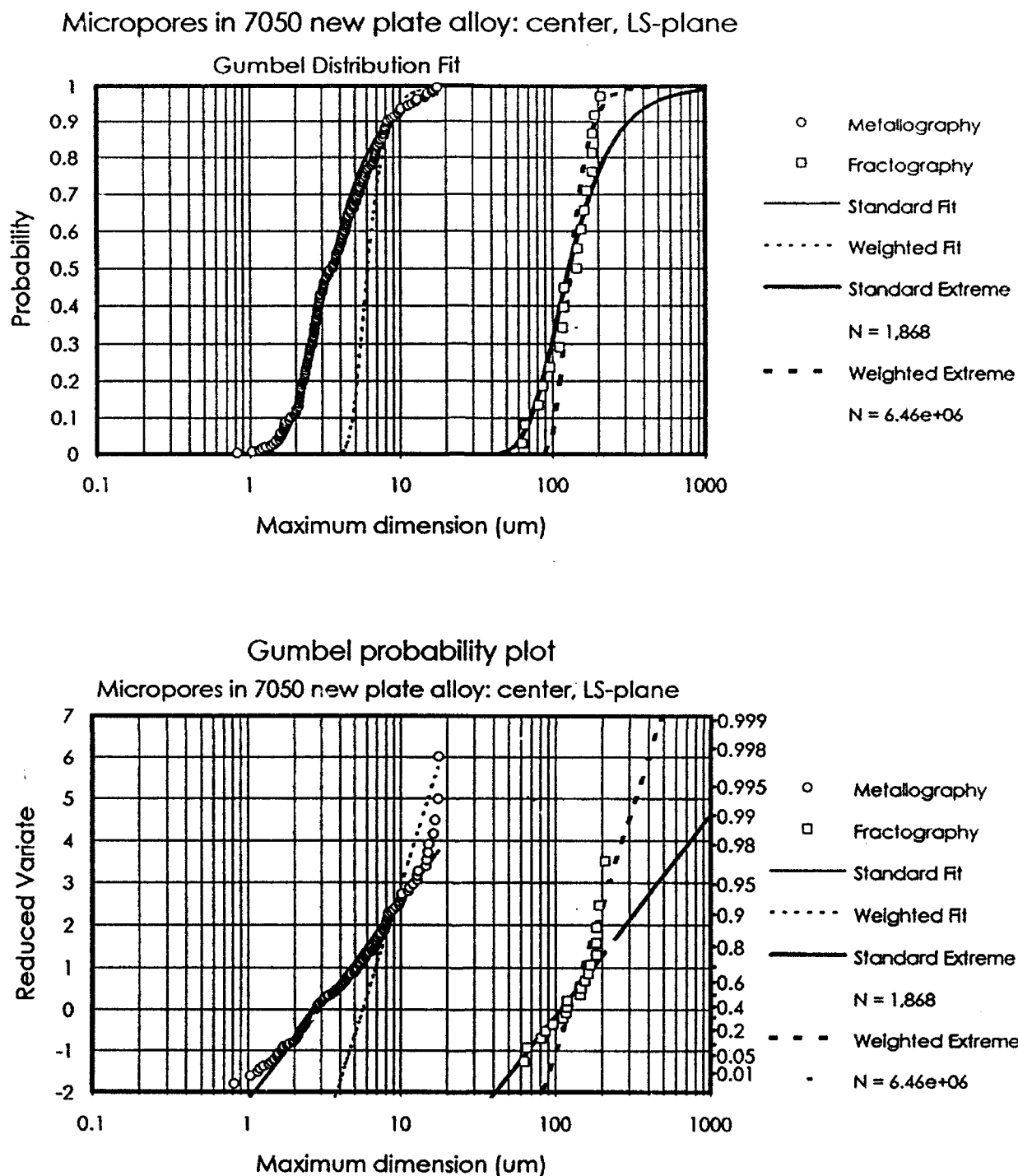
Figure 52. Linear and Gumbel probability plots for metallographic and
fractographic pore size data for new pedigree 7050 alloy.
Metallographic data have been fitted with Gumbel parent
distribution using standard and weighted fit. Resulting extreme
value distributions and their optimum sample sizes, N, are shown
as standard and weighted extreme distribution lines.

Fatigue Data for 7050-T7451 Plate Alloys
Smooth Samples, Max. Stress = 240 MPA, R = 0.1
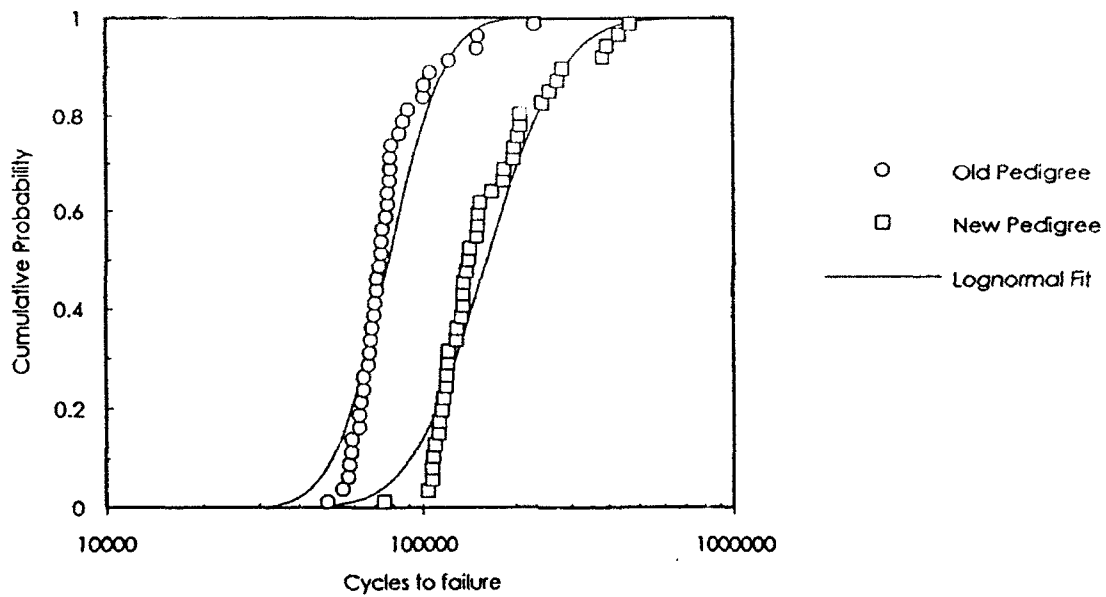
Fatigue Data for 7050-T7451 Plate Alloys
Smooth Samples, Max. Stress = 240 MPA, R = 0.1
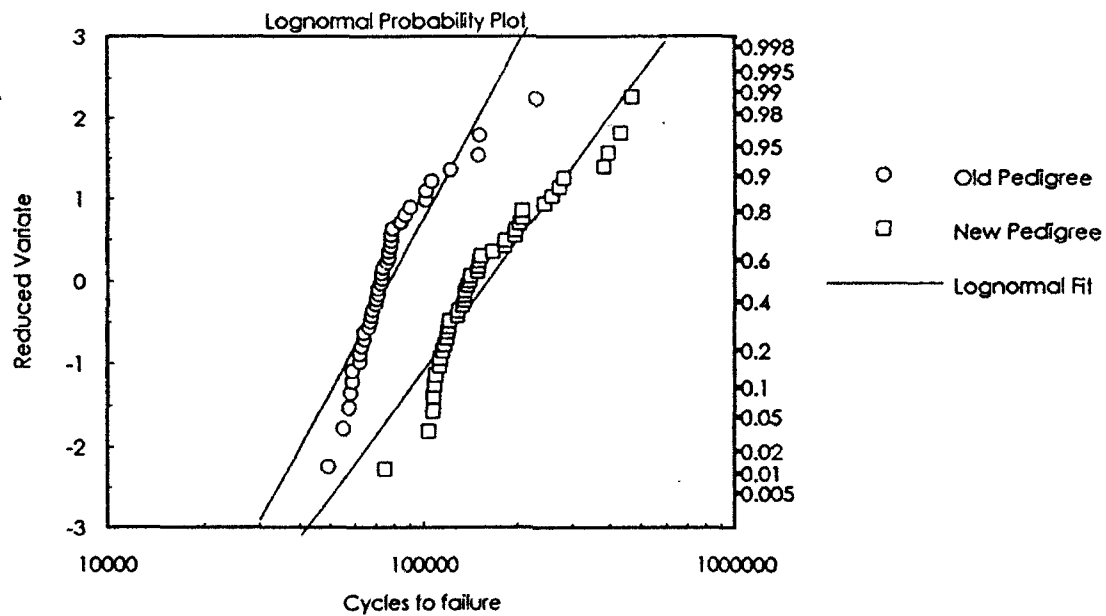
Figure 53. Linear and lognormal cumulative probability plots of cycles-to-failure data for smooth fatigue samples made from new (low porosity) and old (high porosity) 7050-T7451 alloys. Maximum tensile stress 240 MPa, R = 0.1.

Fatigue Life Predictions for 7050-T7451 Old Plate Alloy
Smooth Fatigue Samples, Max. Stress = 240 MPa, R = 0.1

(a)
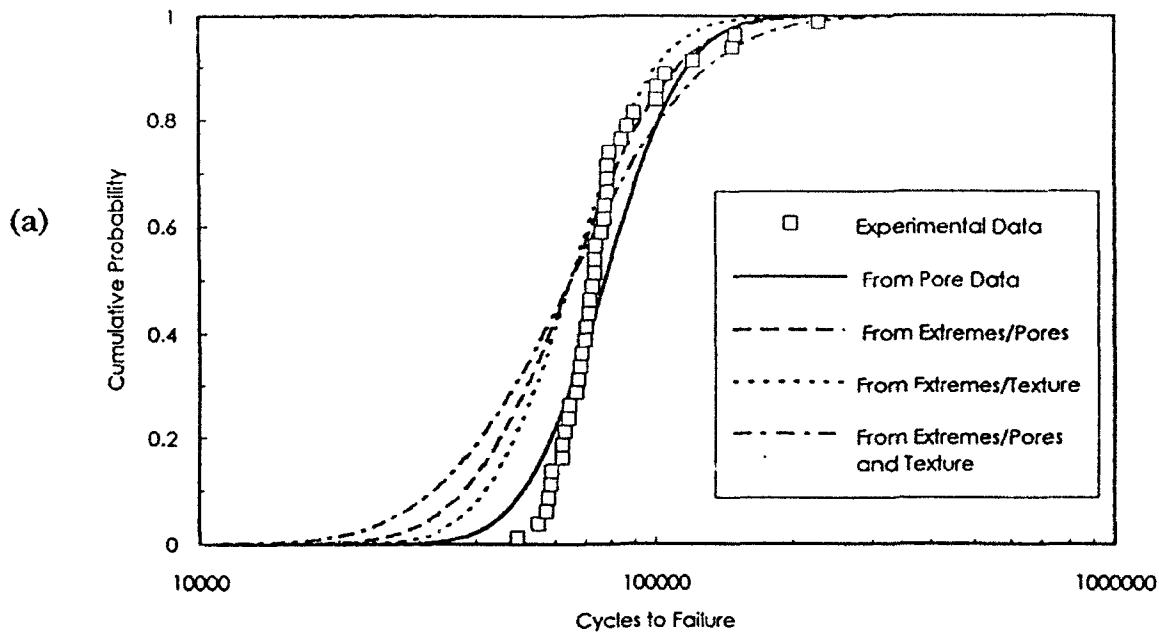
Fatigue Life Predictions for 7050-T7451 New Plate Alloy
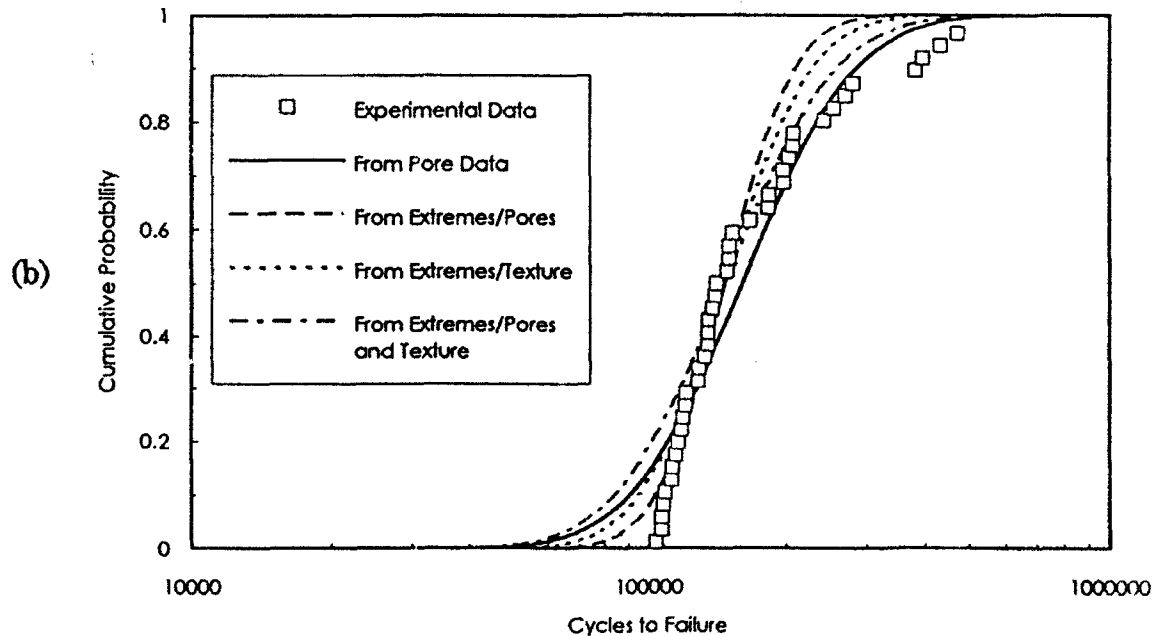Smooth Fatigue Samples, Max. Stress = 240 MPa, R = 0.1

(b)

Figure 54. Comparison of the experimental fatigue data with predictions for (a) old and (b) new pedigree 7050 alloys. Predictions obtained using, as input: (1) crack initiating pore size data (Pore Data), (2) estimated extreme pore size distributions (Extremes/Pores), (3) estimated texture fluctuations (Extremes/Texture) and (4) both texture and extreme pore size distributions (Extremes/Pores and Texture).
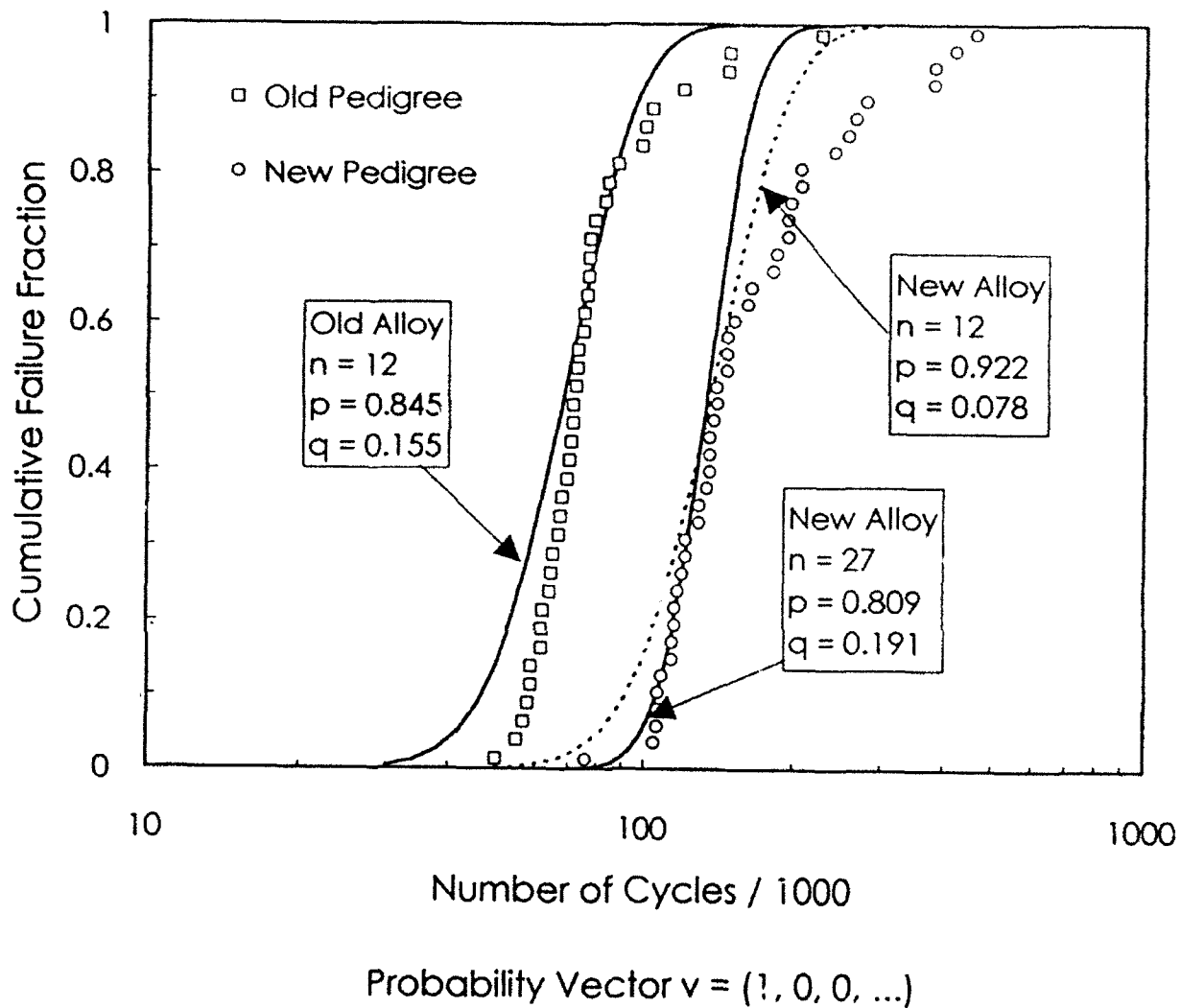
Figure 55. Comparison of the fatigue data for old and new pedigree 7050 alloys with predictions from the Markov B-model. Maximum tensile stress 240 MPa, R = 0.1, n is the size of the transition matrix, p is probability that crack does not grow during one duty cycle, q = 1 - p.

Cumulative Fatigue Failure Distribution
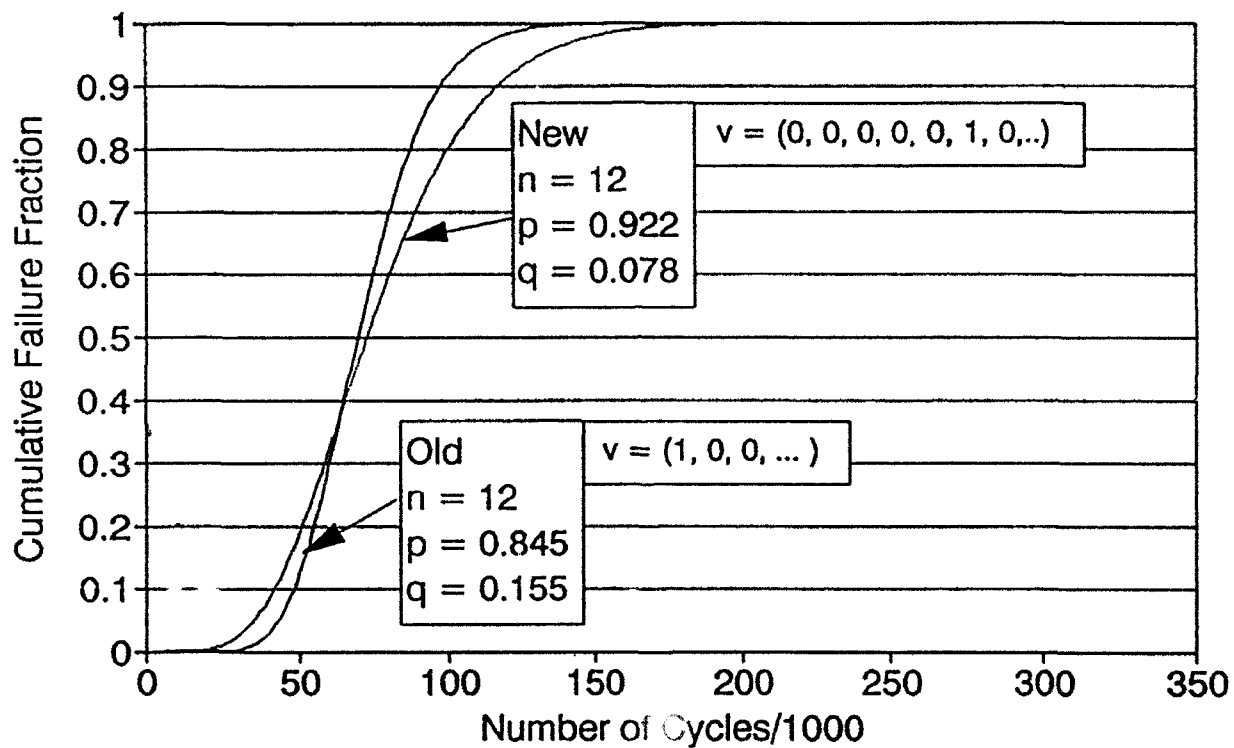## 7050 Alloy, Markov B-Model

Figure 56. Simulation of the effect of the increase of the initial crack length on the Markov chain model prediction. By increasing initial crack length in the new alloy from position number one to six in the probability vector, it was possible to obtain similar fatigue life distributions in both new and old alloys. Notation and loading the same as in figure 55.

Fatigue Failure Distribution
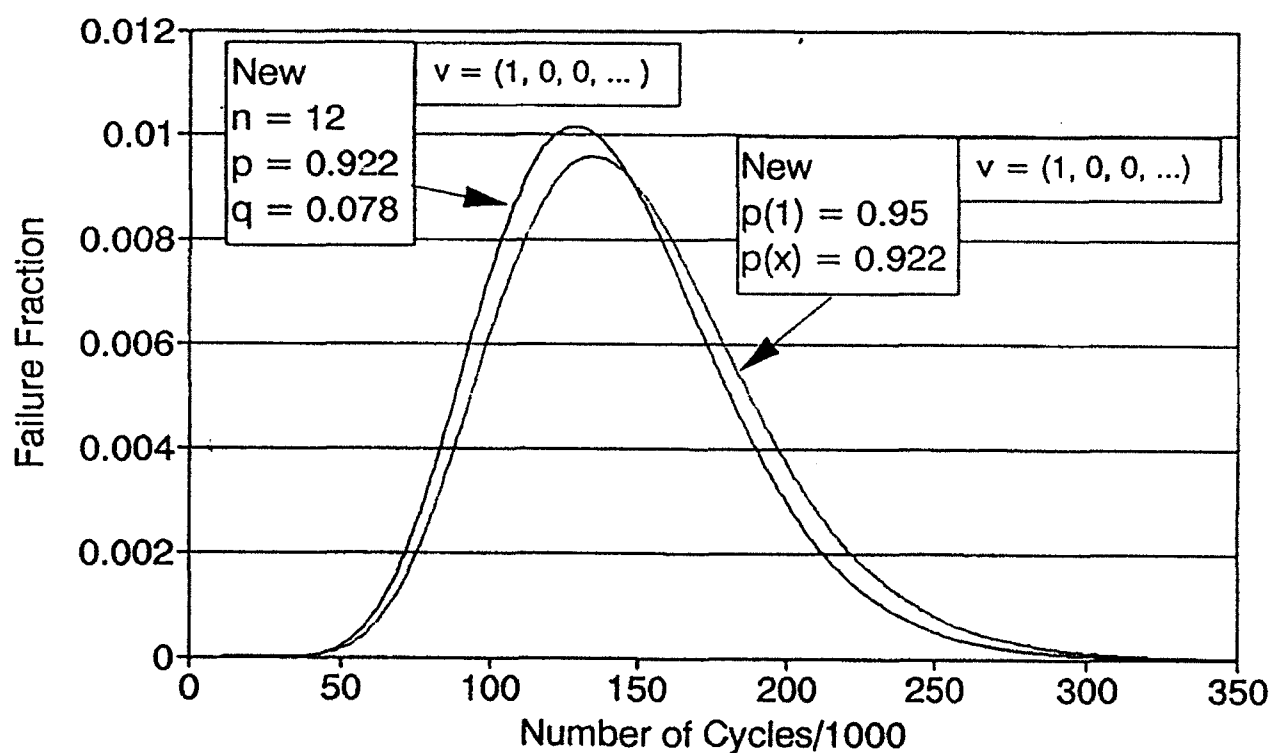## 7050 Alloy, Markov B-Model

Figure 57a. Effect of the change of the p value in the first row of the
transition matrix on the fatigue life distributions predicted by the
Markov B-model. New alloy, notation as in figure 55.

Fatigue Failure Distribution
7050 Alloy, Markov B-Model

New	$v = (1, 0, 0, ...)$
$n = 12$	
$p = 0.922$	
$q = 0.078$	

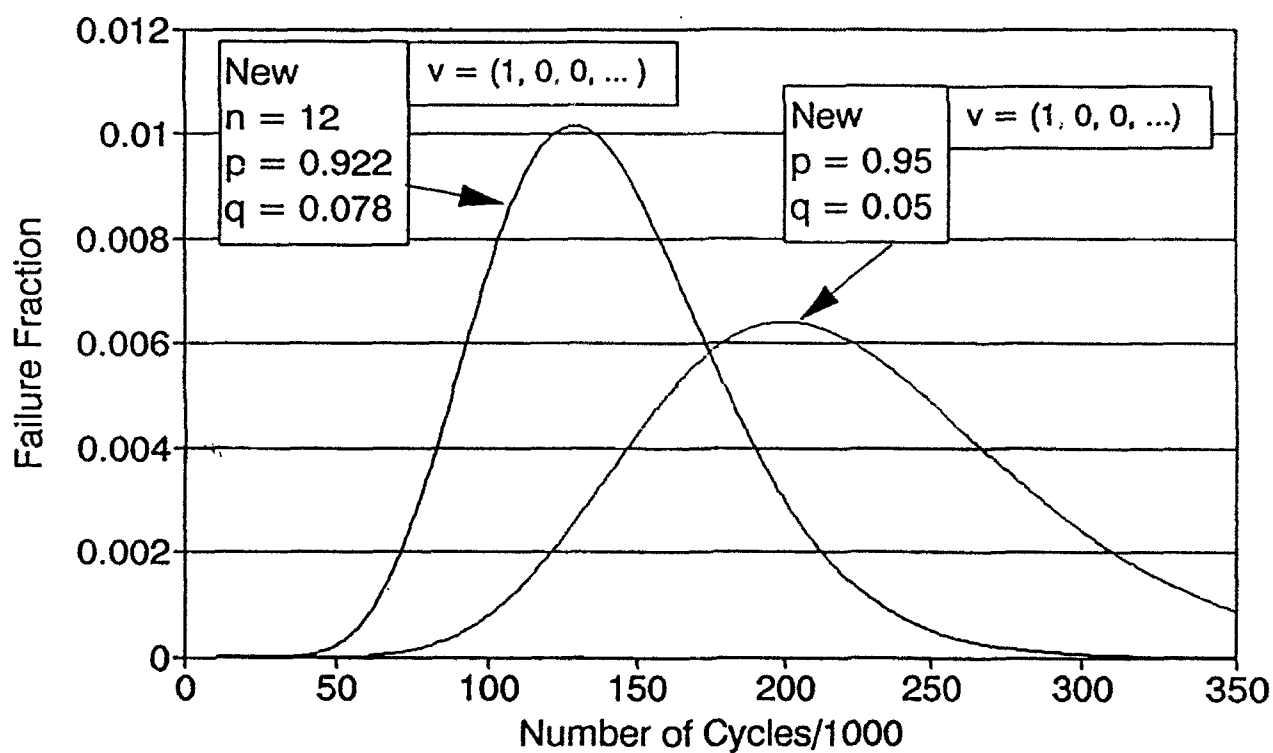| New	$v = (1, 0, 0, ...)$
$p = 0.95$	
$q = 0.05$	

Figure 57b. Effect of the change of the p value in the entire transition matrix on the fatigue life distributions predicted by the Markov B-model. New alloy, notation as in figure 55.

110